CUTTING MECHANICS AND MANUFACTURE OF OPTICS FOR IMAGING APPLICATIONS

by

John Roberson Troutman

A dissertation submitted to the faculty of
The University of North Carolina at Charlotte
in partial fulfillment of the requirements
for the degree of Doctor of Philosophy in
Optical Science and Engineering

Charlotte

2016

Approved by:

_____
Dr. Matthew A. Davies

_____
Dr. Tony L. Schmitz

_____
Dr. Thomas J. Suleski

_____
Dr. Joseph D. Owen

_____
Dr. Mehdi Miri

ABSTRACT

JOHN ROBERSON TROUTMAN. Cutting mechanics and manufacture of optics for imaging applications. (Under the direction of DR. MATTHEW A. DAVIES)

Ultraprecision diamond machining enables physical realization of freeform surfaces of nearly arbitrary complexity through turning and milling processes. Achievable form accuracies make diamond machining a viable alternative to conventional techniques particularly for infrared and longer wavelength applications. This dissertation aims to further the knowledge base for manufacturing of infrared optics. Many infrared materials including germanium and chalcogenide glass ($As_{40}Se_{60}$, trade name IRG 26) are brittle, but under appropriate conditions, they can be machined in a ductile-dominated manner, resulting in a fracture-free and often optical quality surface. The cutting mechanics, surface condition, and subsurface integrity of these materials were studied to independently isolate effects due to cutting velocity, rake angle, and tool-workpiece interaction time. Experiments were performed under steady-state conditions using orthogonal, oblique, and round-nosed turning geometries, as well as under interrupted cutting conditions using flycutting and milling configurations. To overcome the limitations of conventional computer aided manufacturing packages, an analytical strategy for toolpath generation for slow tool servo machining operations was developed and verified in conjunction with an artifact-based approach for pre-process mapping and compensation of tool- and machine-based process error sources. The research findings were then used to select appropriate machining parameters and generate toolpaths for the manufacturing of several freeform optics including a chalcogenide glass Alvarez lens pair and the primary and tertiary mirrors of a compact imaging spectrometer.

ACKNOWLEDGEMENTS

I am very grateful to Professors Matthew Davies and Tony Schmitz for their guidance, encouragement, and their support in fostering an environment which enabled me to develop and pursue my research interests. I am also grateful to my committee members, Professor Thomas Suleski and Dr. Joseph Owen, for their insight and assistance with completing this dissertation, and to Dr. Chris Evans, with whom I have had many helpful discussions along the way.

I would like to thank Joel Pritchard, Roland Hege, and Joe Dalton for sparking and encouraging my passion for machining. Special thanks also belong to my research and lab mates Daniel, Chris, Vasishta, and Preston, as well as colleagues Jason and Tres. I am thankful for financial support from the National Science Foundation and the Center for Freeform Optics, without which this dissertation would not have been possible.

TABLE OF CONTENTS

NOMENCLATURE AND ABBREVIATIONS

d_a	Axial tool engagement
d_r	Radial tool engagement (milling)
w_c	Chip width
t_c	Chip thickness
f_t	Feed per revolution (turning) or feed per cutter tooth (milling)
X	Tool side cutting edge angle
θ	Tool nose sweep angle
Φ	Cutter angular orientation
α, α_{eff}	Tool and effective rake angles
Ψ	Spindle inclination angle
R_{ct}	Cutter radius of curvature
D_t	Milling tool diameter
Ω	Spindle rotational rate
V_c	Cutting velocity
ρ, ϕ, z	Right cylindrical coordinates
X, Z, C	Machine axis coordinates
F_c, K_c	Orthogonal cutting force component, coefficient
F_t, K_t	Orthogonal thrust force component, coefficient
F_a, F_p, F_v	Generalized resultant force components
F_x, F_y, F_z	Dynamometer force coordinate system
S_{pv}, Sa	Areal surface peak-valley height, average departure from mean plane
rms	Root mean square
fpr	Feed per revolution
rpm	Revolutions per minute
STS	Slow tool servo
SCD	Single crystal diamond
CAD/CAM	Computer aided design / manufacturing

CHAPTER 1: MOTIVATION AND BACKGROUND

For centuries, glass components have been used for many optical applications including astronomical observation and microscopy. After initial casting or molding, such optics were typically finished, or figured, by hand using fine abrasive processes such as lapping and polishing. Due to the relative ease of manufacture and available and proven measurement techniques such as the Ronchi test [1] or Focault knife-edge test [2], these optics were, and have through contemporary times been most always composed of combinations of flat and/or spherical surfaces.

Enabling the manufacturability of freeform optics has revolutionized the field of optical design [3] [4]. Such components offer many advantages over traditional components. By giving optical designers more flexibility in surface specification, freeform optics can enhance system performance in ways not previously possible, such as by correcting for aberrations, or by enabling novel functions such as in the case of the Alvarez lens [5]. By combining multiple traditional surfaces into a single composite element, freeforms can be used to make system integration easier by reducing the number of elements, mass, and complexity of a given system, and often reducing total package size. By reducing the component count of a system, the number degrees of freedom and hence sources for possible errors in assemblies is also reduced. With modern ultraprecision machining centers, mounting and alignment features can be machined directly on an optic without changing the machining setup, transferring the accuracy of the machine tool directly to the component. Machining alignment features directly into a

component reducing the combined uncertainty in assemblies when compared with conventional methods in which mounting features were cut (often on a separate machine) in a different setup than used for machining the optical surface, thus transferring the uncertainty of the multiple set-ups into the optic and its alignment features. Freeform optics are finding expanded use in many areas including medical imaging, directed light management, and night vision devices.

It has been known since the 1960s [6] that under appropriate cutting conditions, optical glasses and other brittle materials can be machined in a manner similar to metals by grinding [7] [8] [9] [10] and turning [11] [12] [13] [14] [15] [16] [17] [18] [19] [20] [21] [22], often producing long, curly chips. The development of high-stiffness, high-accuracy CNC lathes enabled single point diamond turning (SPDT) of rotationally-symmetric components with increasing form accuracy, while in the early 2000s, coordinated motion of position-controlled rotary and linear [23] axes allowed "slow tool servo" (STS) machining of non-axisymmetric components with surface departures which are sufficiently mild enough to prevent tool-workpiece collisions. While contemporary diamond turning lathes can typically operate at several hundred rpm in STS mode, the maximum speed is dependent on required tool stroke (often several mm in magnitude) and system bandwidth. For non-axisymmetric components requiring small tool strokes (on order of 100 μm), cycle time can be often be reduced by an order of magnitude by mounting the turning tool atop an auxiliary piezoelectric or voice coil actuated fast tool servo (FTS) which is attached to one of the lathe's linear axes. With appropriate low-mass tooling, FTS bandwidths up to 1000 Hz can be achieved. Though initially limited by development of sufficiently-capable tooling, modern diamond machining centers offer

optional high speed auxiliary spindles in combination with 5 or more position-controlled axes which allow diamond milling [24] [25] [26] [27] [28] of components of nearly arbitrary shape. With care, these diamond machining centers are capable of producing components with form tolerances of ±100 nm and surface finishes below 5 nm Ra. Such specifications are sufficient for producing optics and molds for infrared applications which require no further processing, as well as components for visible applications which require only final figure correction. For prototyping and low-volume production, ultraprecision diamond machining is less expensive and faster than conventional molding processes. Aside from plastics, ductile non-ferrous metals, and some visible glasses [29], ultraprecision diamond machining is used widely in the production of germanium optics, and in machining other infrared materials such as zinc selenide, zinc sulfide, and cadmium telluride. As demand for infrared applications has grown, so has the importance of chalcogenide glasses, which include sulfides, selenides, and tellurides.

This dissertation focuses on the cutting mechanics and surface integrity of amorphous chalcogenide glass and single crystal germanium. A process methodology is developed for STS operations, and cutting parameters identified using simplified experimental geometries are applied to the production of both reflective and transmissive freeform optics using the STS technique.

When a force is applied to a material, it will first deform elastically, in a manner that is reversible upon removal of the load. After some critical yield stress is exceeded, the material will begin to plastically deform in an irreversible manner, and then will fracture at some critical value of strain. Brittle materials are loosely defined as those materials which support little to no plastic deformation (i.e. the onset of fracture is abrupt

and immediate after exceeding the material's yield stress.) Efforts to model the material removal process in ultraprecision grinding of brittle materials [7] were based upon the knowledge of microcracking as described in [30] [31] [32] [33]. Such cracking has two phases, crack initiation and crack propagation. While crack propagation is relatively well-understood, crack initiation behavior is largely affected by unknown material properties such as residual stress state and the existence of damage due to handling or previous machining and environment. However, analysis of the Bossinesq and Hertzian stress fields below sharp- and round-tipped indenters [34] reveals that even without knowledge about the presence of preexisting nucleation sites, it is reasonable to expect a crack to initiate preferentially close to the indenter axis at the base of the resulting plastic deformation field, at the point where tensile stress reaches a local maximum. As described in [30] and shown in [31] [34], after a load is applied, at some critical load value, a *median* crack along the indenter axis (in a plane parallel to the specimen surface) opens, and as the load increases, the crack grows in length at a steady rate related to the applied load and the ratio of the material's hardness to its elastic modulus. Upon unloading, the median crack closes, but does not heal, and "sideways" or *lateral* cracks open up, and upon complete removal of the load, continue to grow towards the surface of the specimen. This cracking process is illustrated in Figure 1.1.

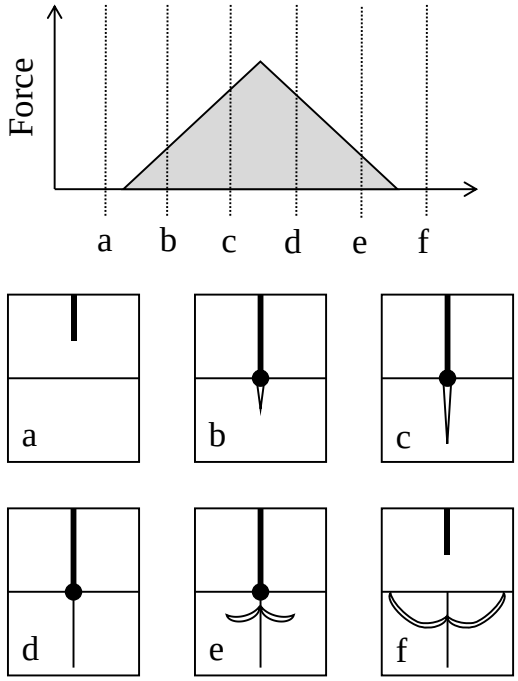

Figure 1.1: Loading profile and six stages of crack propagation: (a) unloaded condition, (b) load increasing, median crack opening, (c) load increasing, median crack growth, (d) load decreasing, median crack closure, (e) load decreasing, lateral crack opening, (f) unloaded condition, lateral crack propagation to surface. Adapted from [34].

It is shown for the case of soda-lime glass in [35] and for an AsGeSe chalcogenide in [36] that indentation behavior is significantly temperature-dependent, with both materials exhibiting a marked increase in fracture toughness at temperatures above the glass transition temperature. At all temperatures, it was shown that chalcogenide glasses have a much lower fracture toughness than soda-lime or other silica-based glasses.

In the indentation literature [19] [34], it was observed that certain brittle materials, particularly optical glasses, support small plastic deformation before fracturing, and that the initiation of fracture occurs at some critical indentation depth. As described in [19], under stress free conditions, due to the inevitable presence of flaws in the material, it can be argued that the fracture stress of a material is less than some supposed flow stress

required to initiate plastic flow in the material, which is itself less than the idealized yield strength of the material, if it had no existing flaws. As observed experimentally in [37], the presence of high hydrostatic stress is known to suppress fracture and enable plastic flow at a stress level lower than the failure stress. Thus in cutting with sufficient hydrostatic stress material removal by a ductile mechanism can be possible in nominally brittle materials. It is for this reason that large negative rake angles are used in machining brittle materials, as they increase the hydrostatic pressure near the cutting zone. Accordingly, early efforts [6] [11] to machine glass by ruling or turning using single point tools did so with cone-shaped diamond indenters, providing effective rake angles of approximately -38°.

In abrasive machining processes such as grinding, a transition from a ductile-dominated machining mode to a brittle-dominated mode was proposed in [38] which was controlled by the size of abrasive particle, while a similar transition was shown in [7] as a function of grinding wheel infeed rate. Drawing from these observations, a model was developed for diamond turning [17] [39] [18] which related machining behavior to chip thickness. During a face-turning process using a round-nosed tool, instantaneous chip thickness is determined by both depth of cut and infeed rate, and varies with location along the tool nose. This model, known from here forward as the "critical chip thickness model," postulates that at chip thicknesses greater than some critical value, fractures begin to propagate ahead of the tool and into the material. Under appropriate cutting conditions, fractures either do not occur, or due to a correspondingly short fracture propagation depth, are removed by the next pass of the tool, leaving behind a smooth, damage-free surface. However, at higher chip thicknesses, fractures propagate far

enough into the workpiece that the resulting surface has fractures that degrade surface finish and appearance. According to the critical chip thickness model, a marked, abrupt ductile-brittle transition is predicted when the critical chip thickness is exceeded. Others, as described in [13] and indicated experimentally in [40], have shown that during turning of germanium, the measured thrust force component is much larger than the cutting component at nanometer level commanded uncut chip thicknesses, suggesting rubbing between the tool nose and no material removal by chip formation, while as commanded uncut chip thickness is increased, the resultant force rotates towards the workpiece surface and material removal by ductile chip formation may occur. The onset of surface fracture can be associated with this force system direction in the "critical stress model" which postulates that above some certain chip thickness value, this rotation induces fracture through resolved tensile stresses behind the tool. While there is some disagreement over the onset and origin of the surface fractures, both models relate cutting behavior to commanded uncut chip thickness, and experimental results [40] confirm that a more negative rake tool increases the commanded uncut chip thickness for which fracture-free surfaces are attained. These purely geometric cutting models can neither support nor refute anecdotal evidence and operator experience which suggests that some materials such as spinel and germanium can be more readily diamond milled than diamond turned. In milling the process is more dynamic than in turning and very short tool-workpiece contact times (<1 ms) are typical. Geometric models also do not explain the reduction in tool wear rate at extremely low contact times during flycutting of steel, as seen in [41].

For the purposes of this dissertation, we define "ductile-dominated cutting conditions" as those under which material can be removed while leaving behind a smooth, fracture-free surface of optical finish. Such a ductile cutting regime can often be characterized by the production of long, curly chips similar to those in [11] [42] [43], and by measured cutting forces which scale approximately linearly with cross-sectional chip area. Under brittle-dominated machining conditions which are presumably due to a material removal mechanism dominated by fracture, the resulting surface is typically visibly dull or matte in appearance and can be observed to be pitted using both digital microscope and scanning white light interferometric (SWLI) measurement techniques. Resulting chip form is dominated by short, broken, powder-like chips. Resultant cutting forces are approximately invariant with chip cross-sectional area and are much lower than those measured in a ductile cutting regime. These are a compelling indicator of a brittle-dominated machining mode.

Unlike in grinding operations where the cutting geometry is undefined due to the random shape and orientation of the abrasive particles, the cutting geometries of milling and turning operations are well-defined by variables such as depth of cut, feed rate, tool nose radius, and tool rake angle, which are discussed further in Section 2.2. Using round-nosed tools, chip thickness is a function of both feed rate and depth of cut, which also varies with location along the tool nose. By performing cutting experiments with appropriately-oriented dead-sharp tools, the cutting arrangement can be reduced to orthogonal conditions as described in [44] [45]. In this geometry, the chip is rectangular with constant thickness determined only by the feed rate and a width determined only by the depth of cut. This arrangement produces plane strain conditions, under which all of

the shearing or chip-forming action is assumed to lie in a single plane. Resultant forces can be projected into a cutting force which is along the direction of cutting velocity, and a thrust force which opposes the feed motion. This two-dimensional arrangement contrasts the more complex, three-dimensional representation of oblique machining. As described in [46], there have been many attempts to analytically relate machining behavior to basic material properties such as elastic modulus and yield strength through shear-plane models, slip-line field models, and shear zone models. However, in general, agreement with experimental results for these models is less than desired, as such models often neglect less well-understood effects due to temperature, strain hardening, etc. The most accurate models combine finite-element approaches with experimental force data, yet modeling of metal-cutting processes is still largely empirical. Interpolation between experimentally measured conditions is possible, but extrapolation or prediction of conditions far from those measured typically meets with less success. For brittle materials, predictive models are even more difficult.

Although it is well-known that brittle materials can be machined in a ductile-dominated mode to leave behind an optically smooth surface, such a surface does not guarantee the absence of subsurface damage and cracking. Subsurface quality is of supreme importance for components used in high-power laser applications or for applications in harsh environments such as those encountered in military or space-based systems. In these cases, the presence of subsurface damage or defects will be propagated by cycling in the environment and can cause accelerated component failure. Prevention and removal of such damage is presently a limiting factor in the production of silicon wafers for optoelectronics [9]. While as-grown single-crystal boules can be assumed to

be nearly defect-free, the slicing of wafers, often using a wire saw, creates mechanical damage. After slicing, wafers are typically flat-lapped, chemically etched, and then subjected to multiple polishing processes to remove remaining damage [8]. Several models for subsurface damage accumulation in silicon are discussed in [10]. While the bulk silicon is monocrystalline, the damaged layer consists of polycrystalline segments with a packing density less than that of the monocrystalline lattice, leading to residual compressive surface stresses which can be observed using many spectroscopic techniques, as well as a distorted lattice structure which complicates and often precludes fabrication by lithographic or other deposition-based techniques. Ductile-regime grinding [7] is proposed as an alternative to traditional wafer processing techniques, replacing multi-step polishing processes with a single finish grind. In [8], cracks resulting from silicon grinding processes were examined using optical microscopy after cleaving and sectioning of the ground wafer. Atomic force microscopy (AFM) examination of as-ground surfaces before sectioning confirmed that subsurface damage often exists below surfaces that appear otherwise smooth and fracture-free. While subsurface crack depth was shown to be generally independent of crystalline orientation, crack depth was shown to increase with both grinding wheel feed per revolution and grinding wheel grit size.

Once appropriate cutting parameters are selected to produce the desired mechanical properties of the surface on a component, generation of numerical-control (NC) toolpath for ultraprecision machining is required. This process is difficult due to the typical sub-micrometer tolerances required. Macroscale components are often well-represented in CAD/CAM packages by primitive solids. While optical designers

typically describe a surface using a mathematical equation, such packages often represent complex surfaces as a collection of triangular patches and approximate non-circular curves as a series of discrete splines. While these approximations are acceptable for general manufacturing where tolerances are on the order of several micrometers or more, they induce errors which are inappropriate for ultraprecision machining. CAD/CAM packages also often lack required functionality to define tools of arbitrary shape or having errors of arbitrary shape on a scale that affects the overall part form on an optical scale. Although CAM software packages designed specifically for diamond turning and milling are available and can compensate for tool shape errors often called tool waviness, such packages often utilize specialized, application-specific methods for defining surface form, restricting functionality and reducing ease of use. However, similar to the method used in [47] for ultraprecision milling, using a coding environment such as MATLAB®, toolpath points can be calculated directly from an optical equation and tool description. Using such a method, deterministic errors due to causes such as tool and machine axis waviness can be compensated directly in NC code.

The literature base has generally shown that germanium can diamond turned in a ductile manner at chip thicknesses on the order of 100 nm, while optical glasses of varying composition can be machined at chip thicknesses on the order of 1 μm. Although simplified tests can be used to quickly identify suitable cutting parameters, the knowledge base is very narrow for other infrared materials, particularly chalcogenide glasses.

The remainder of this dissertation is organized as follows: Chapter 2 defines cutting force models for milling and turning and introduces the notation which is used in

the remainder of this work. Chapter 3 describes the equipment and experimental arrangements used to complete this research. Chapter 4 presents a comprehensive study of the cutting mechanics of an arsenic selenide (trade name IRG 26) chalcogenide glass during steady-state and interrupted cutting conditions, with both square and round tools. Chapter 5 summarizes previously-reported results for orthogonal turning of germanium, and presents a brief study of cutting mechanics and surface integrity for specimens machined using round-nosed tools. In Chapter 6, a methodology for mapping common tool and machine error sources and generating NC toolpaths for STS machining is presented. Chapter 7 utilizes the results of Chapter 4 and demonstrates validity of the STS approach through the manufacture of a transmissive freeform chalcogenide glass lens pair, while Chapter 8 describes STS manufacturing and initial metrology of reflective freeform mirrors for a miniature imaging spectrometer. The findings of this dissertation, a brief discussion, and remarks on suggested future work are summarized in Chapter 9.

The original contributions of this research are: (1) a comprehensive study of the cutting mechanics of IRG 26 ($As_{40}Se_{60}$) chalcogenide glass as a function of chip thickness, cutting speed, rake angle, and tool-workpiece interaction time, (2) validation of a mechanistic cutting force model used to predict forces for machining of both IRG 26 and single crystal germanium, (3) a initial correlation of cutting mechanics, surface condition, and subsurface integrity of turned and flycut germanium specimens, and (4) an analytical toolpath generation strategy and pre-process approach for mapping and compensation for tool waviness, tool offset error, and machine axis waviness for slow tool servo ultraprecision machining operations.

CHAPTER 2: CUTTING FORCE MODEL FOR MACHINING

2.1 Introduction

This chapter develops the cutting force models for milling and turning operations which are used throughout the remainder of this dissertation. These models are not new and are fundamentally based upon the analyses described in [48] [49] as well as many other works. However, application of these force models to brittle materials such as those used in ultraprecision machining of optics is an emerging research topic.

2.2 Cutting Force Model for Turning

Turning operations, in which a stationary tool is fed into a rotating workpiece, are commonly used for production of rotationally-symmetric components. Although more complex machines may incorporate more degrees of freedom, the most common lathes combine two perpendicular linear axes with a rotating spindle. In these operations, process forces may be measured by mounting the cutting tool atop a force transducer (often a small dynamometer), so it is convenient to define a force reference frame which is fixed at the tool tip, and to characterize these processes by the forces exerted by the workpiece upon the tool. While orthogonal turning is the simplest turning geometry, a unified mechanistic cutting force model enables force prediction and meaningful comparison between various processes.

2.2.1 Orthogonal Turning

In the simplest turning configuration, the cutting tool is oriented such that the cutting velocity direction at the tool edge, the tool cutting edge, and the feed direction are mutually orthogonal. This arrangement is shown in Figure 2.1 for an outer diameter (OD) turning operation. This cutting geometry results in a rectangular chip of width, w_c, equal to the depth of cut, d_a, and a thickness, t_c, equal to the commanded feed per revolution, f_t. In this configuration, the resultant force upon the tool lies in a single plane, and can be decomposed into a cutting component, F_c, along the cutting velocity direction, and a thrust component, F_t, opposing the feed motion. These forces can be expressed as shown in Eq. 2.1 as a function of cutting and thrust coefficients K_c and K_t, and process geometry. For metals, these process coefficients which depend upon both material properties and tool condition are often approximately constant and are tabulated in references such as [48] [49], but for materials which exhibit a transition from a ductile-dominated to a brittle-dominated cutting mechanism, these coefficients may themselves be a strong function of t_c, for example as described in [47] [50].

$$\begin{Bmatrix} F_c \\ F_t \end{Bmatrix} = w_c t_c \begin{Bmatrix} K_c(t_c) \\ K_t(t_c) \end{Bmatrix} \qquad \text{Eq. 2.1}$$

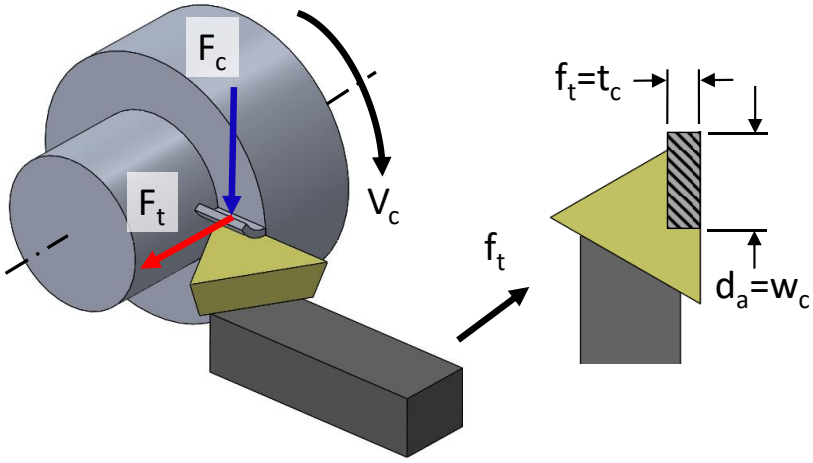

Figure 2.1: Orthogonal OD turning geometry and force model.

2.2.2 Oblique Turning

In oblique turning, the rotation of the cutting edge by the side cutting edge angle, χ, produces a resultant force upon the tool which can no longer be decomposed into the cutting and thrust force components present during orthogonal turning. For this configuration, as shown in Figure 2.2, it is convenient to define force components (F_a, F_p, F_v) with respect to a reference frame which is fixed at the tool tip. In this reference frame, F_v is along the direction of cutting velocity, F_p opposes feed motion, and F_a is perpendicular to both F_p and F_v. For identical values of d_a and f_t, the uncut chip is thinner and wider than for the corresponding case of orthogonal turning, as indicated by Eq. 2.2. Although the resultant force no longer lies in a single plane, its components may be expressed in terms of cutting coefficients K_c, K_t, as described by Eq. 2.3.

$$\begin{Bmatrix} t_c \\ w_c \end{Bmatrix} = \begin{Bmatrix} f_t \sin\theta \\ d_a / \sin\theta \end{Bmatrix} \qquad \text{Eq. 2.2}$$

$$\begin{Bmatrix} F_a \\ F_p \\ F_v \end{Bmatrix} = f_t d_a \begin{Bmatrix} K_t (f_t \sin\theta) \cdot \cos\theta \\ K_t (f_t \sin\theta) \cdot \sin\theta \\ K_c (f_t \sin\theta) \end{Bmatrix} \qquad \text{Eq. 2.3}$$

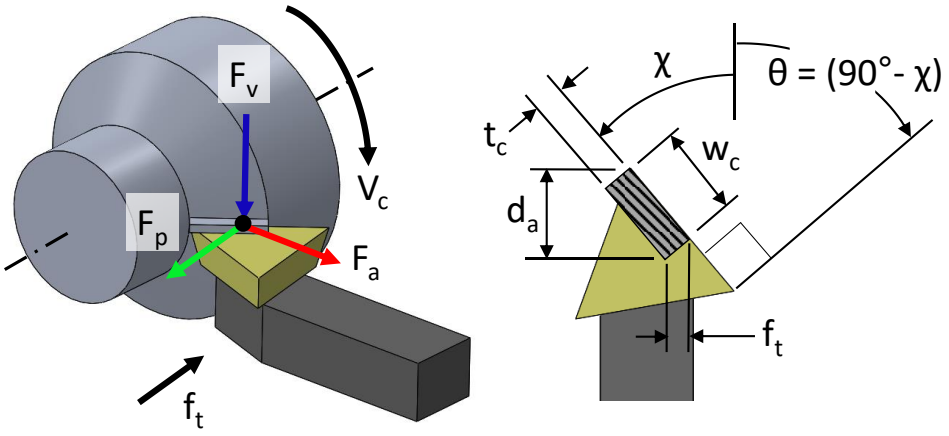

Figure 2.2: Oblique OD turning geometry and force model.

2.2.3 Round-nosed Turning

While simplified cutting geometries such as orthogonal and oblique turning using sharp-nosed tools are useful for study of the cutting behavior of materials, these arrangements are not representative of actual optics manufacture. Tools with a large nose radius, R_{ct}, are preferred to enable production of finer surface finishes for a given feed per revolution, or to allow higher feed rates while maintaining a given finish, as suggested by the approximate relation for surface finish given in Eq. 2.4. Further, tools with negative rake angles, α, are often utilized to induce hydrostatic pressure near the cutting zone and suppress crack formation and propagation in brittle materials, as noted in [37].

$$S_{pv} \approx \frac{f_t^2}{8R_{ct}} \qquad Sa \approx \frac{S_{pv}}{3} \qquad \text{Eq. 2.4}$$

The cutting geometry and force model for a round-nosed face turning configuration are illustrated in Figure 2.3. While many methods [51] have been applied to modeling the chip thickness along the tool nose, the simplest approximation is given in Eq. 2.5. This approximation is compared to reference values numerical simulations in

Figure 2.5 for typical f_t/R_{ct} ratios encountered in diamond turning, and is shown to be an acceptable approximation. This chip thinning effect also enhances ductile-regime machinability by reducing local chip thickness.

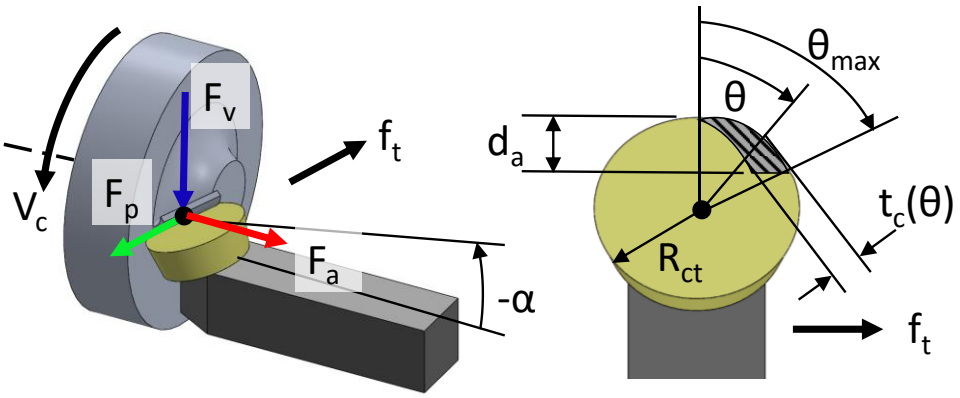

Figure 2.3: Round-nosed face turning geometry and force model.

Building upon Section 2.2.2, as shown in Figure 2.2, such a round-nosed turning operation can be modeled as a collection of discrete oblique turning operations, each with different side cutting edge angles, at each value of tool sweep angle, θ. Building upon the approximation of Eq. 2.5, the resulting forces can once again be predicted from orthogonal turning data by integrating along the tool nose, as described by Eq. 2.6 and Eq. 2.7.

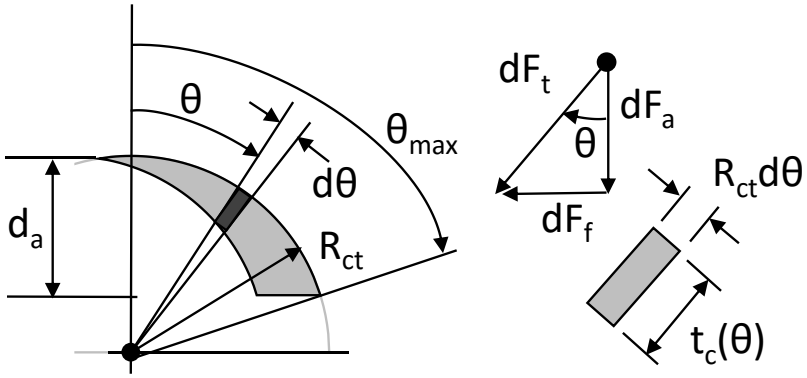

Figure 2.4: Detail of integral geometry for prediction of round-nosed turning forces.

$$\begin{Bmatrix} t_c \\ w_c \end{Bmatrix} = \begin{Bmatrix} f_t \sin\theta \\ R_{ct} d\theta \end{Bmatrix} \quad \text{Eq. 2.5}$$

$$\theta_{max} = \cos^{-1}\left(\frac{R_{ct} - d_a}{R_{ct}}\right) \quad \text{Eq. 2.6}$$

$$t_{c,max} = f_t \sin\theta_{max}$$

$$\begin{Bmatrix} F_a \\ F_p \\ F_v \end{Bmatrix} = f_t R_{ct} \begin{Bmatrix} \int_0^{\theta_{max}} K_t (f_t \sin\theta) \cdot \cos\theta \sin\theta \, d\theta \\ \int_0^{\theta_{max}} K_t (f_t \sin\theta) \cdot \sin^2\theta \, d\theta \\ \int_0^{\theta_{max}} K_c (f_t \sin\theta) \cdot \sin\theta \, d\theta \end{Bmatrix} \quad \text{Eq. 2.7}$$

While the previously developed model for oblique and round-nosed turning enables prediction of forces from orthogonal machining data, it should be noted that due to the fundamental effect of rake angle and local pressure on cutting behavior, especially in nominally brittle materials, such predictions are only valid for process geometry sets with identical rake angle.

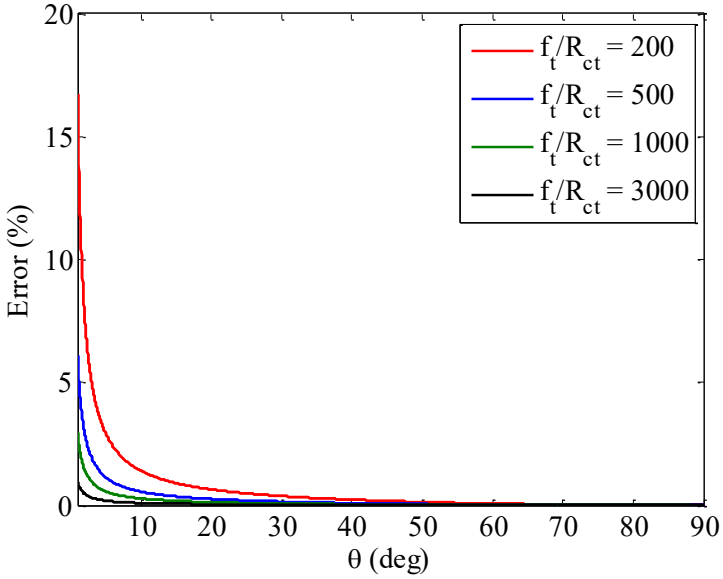

Figure 2.5: Error of chip thickness approximation from Eq. 2.5.

2.3 Cutting Force Model for Milling

While turning operations are only suitable for manufacturing a small subset of possible component geometries, if sufficient tooling and number of position-controlled axes are available, milling operations are capable of producing nearly arbitrary surfaces. In the most common configuration of 3-axis milling, a rotating tool is fed into the workpiece using the motion of three mutually orthogonal linear axes. The cutting force model presented for orthogonal turning can be extended to the case of milling with square tools.

2.3.1 Orthogonal Milling

Unlike in turning, process force measurement during milling operations typically requires mounting the workpiece, not the tool, to the dynamometer or transducer. Therefore, it is more suitable to characterize milling processes by the forces imparted on the workpiece by the tool, and it becomes prudent to express forces in a fixed reference frame which is attached to the workpiece. The simplest case of orthogonal milling using

a square tool is illustrated in Figure 2.6. In this configuration, the chip width is equal to the axial depth of cut, and the chip thickness varies with the cutter angular orientation, ϕ. Although many approaches, as presented in [51] have been proposed for modeling the chip thickness during milling, the simplest approximation is given in Eq. 2.8. This approximation is compared to values obtained from numerical simulation in Figure 2.7 and found to be acceptable for ratios of feed per revolution to cutter diameter, D_t, common in diamond milling.

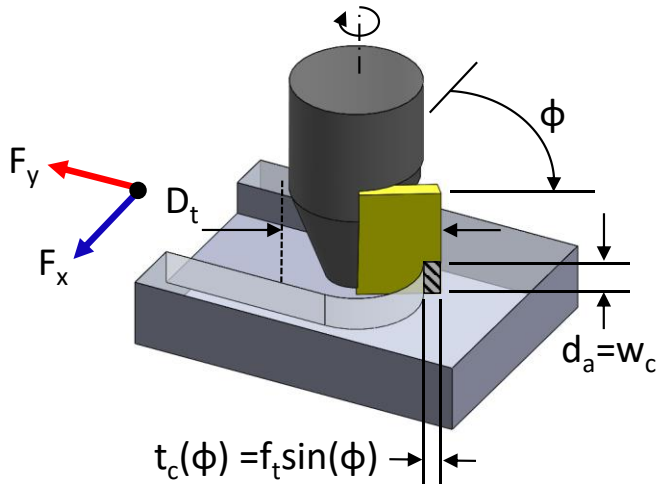

Figure 2.6: Process geometry and cutting force reference frame for orthogonal milling.

$$\begin{Bmatrix} t_c \\ w_c \end{Bmatrix} = \begin{Bmatrix} f_t \sin\phi \\ d_a \end{Bmatrix} \quad \text{Eq. 2.8}$$

$$\begin{Bmatrix} F_c(\phi) \\ F_t(\phi) \end{Bmatrix} = d_a f_t \sin\phi \begin{Bmatrix} K_c(f_t \sin\phi) \\ K_t(f_t \sin\phi) \end{Bmatrix} g(\phi) \quad \text{Eq. 2.9}$$

$$\begin{Bmatrix} F_x(\phi) \\ F_y(\phi) \end{Bmatrix} = \begin{bmatrix} \sin\phi & -\cos\phi \\ -\cos\phi & -\sin\phi \end{bmatrix} \begin{Bmatrix} F_c(\phi) \\ F_t(\phi) \end{Bmatrix} \quad \text{Eq. 2.10}$$

While the resultant force vector changes in both magnitude and direction ϕ, it can still be decomposed into cutting and thrust components at any given instant in time, as given by Eq. 2.9 for the case of a single-tooth cutter. In this relationship, g(ϕ) is a

switching function which is equal to one when the cutter tooth is engaged in the workpiece, and equal to zero otherwise. Again, these forces are expressed in terms of cutting coefficients, which may themselves vary with local uncut chip thickness, and process geometry. For the full-slotting cut illustrated in Figure 2.6, this switching function is equal to one when ϕ is greater than 0° and less than 180°. For the case shown where the tool is fed along the –Y direction of the dynamometer, the rotating cutting and thrust forces can be transformed into the stationary workpiece-based reference frame using Eq. 2.10.

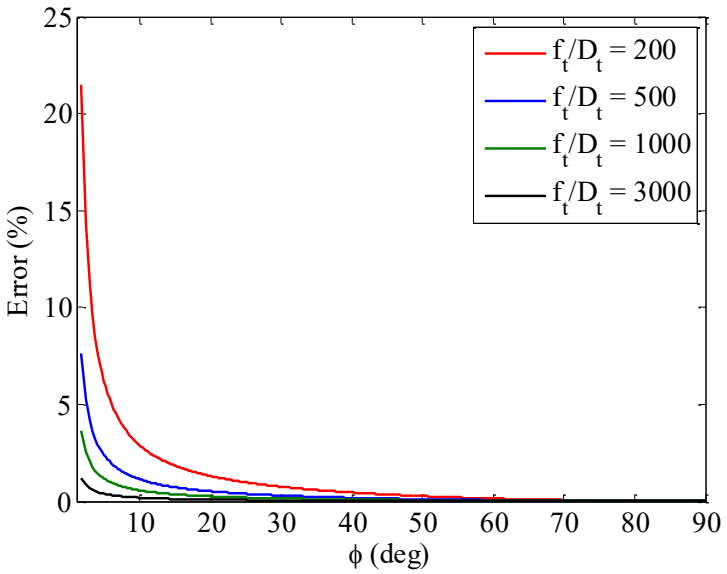

Figure 2.7: Error of chip thickness approximation from Eq. 2.9.

The cutting force models and configurations given in this section will be used throughout the remainder of this dissertation and thus form a common theme for later discussions.

CHAPTER 3: EXPERIMENTAL ARRANGMENTS AND TECHNIQUES

3.1 Introduction

Specialized equipment and experimental apparatus was necessary to complete this dissertation. In this chapter, the equipment used in the research and relevant experimental arrangments are discussed.

3.2 Diamond Machining Center

Cutting experiments and optical fabrication were performed on a Moore Nanotechnology 350FG diamond machining center. This machine is located in a laboratory with temperature control to 20 ± 0.1°C and maximum 50% relative humidity. This 5-axis ultraprecision machining center is equipped with three linear (X, Y, Z) axes and two rotary (B, C) axes with 0.01 nm linear and 0.1μ° rotational programming resolution, respectively. The three linear axes and the rotary B axis are fully constrained oil hydrostatic units, while the C axis incorporates a groove-compensated air bearing. The B axis is a removable unit which mounts to the machine Z-axis table. For the experiments described, the B axis was not necessary and therefore was not installed. The C axis can function as a conventional turning spindle with a maximum speed of 10,000 rpm, or as a rotary positioning axis for coordinated axis (C-X-Z, C-X-Y-Z, etc.) machining. In coordinated axis mode, the controller can process up to 1000 blocks per second. The machine is also equipped with an auxiliary 60,000 RPM air bearing spindle for micro milling and grinding applications and an optical tool setting microscope.

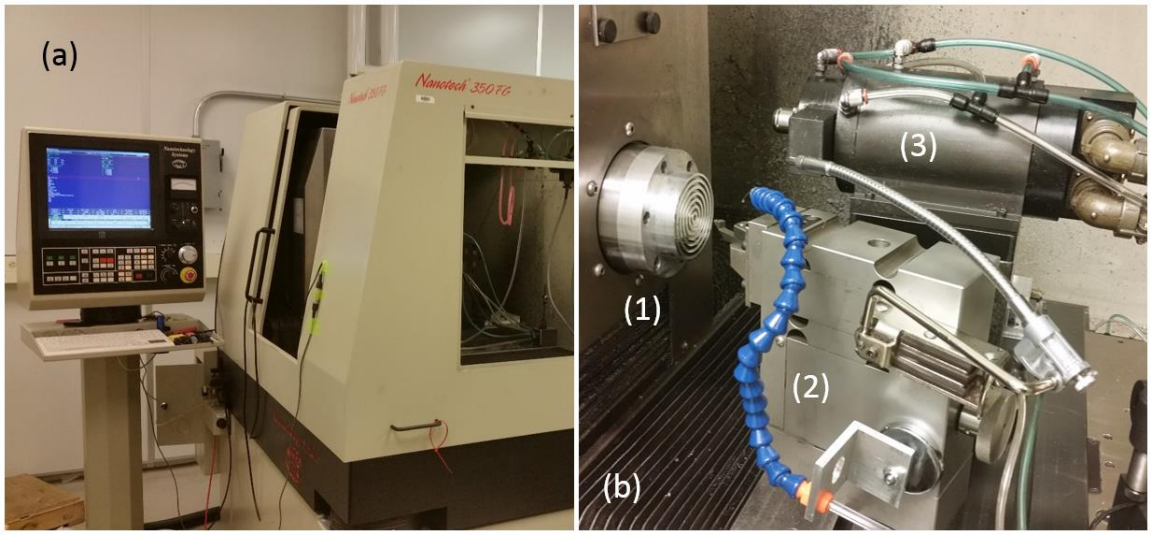

Figure 3.1: (a) Moore Nanotechnology 350 Freeform Generator (b) view of work volume showing (1) main spindle/C axis, (2) toolpost and turning tool, (3) auxiliary micro-milling/grinding spindle.

3.3 Surface Metrology Equipment

The surface finish of components and samples was measured using a Zygo ZeGage Plus scanning white light interferometer (SWLI). Form error of flats and spherical components were measured using a Zygo VeriFire ATZ Fizeau interferometer. Both instruments are shown in Figure 3.2. A Mitutoyo Finescope optical microscope was also utilized for assessment of surface condition and general microscopic examination of tooling and components. Form measurements of freeform optics were performed using an OptiPro UltraSurf 5X at OptiPro in Rochester, NY. Although uncertainties are difficult to estimate, this multi-axis noncontact measurement system is capable of measuring aspherical and freeform components to sub-micrometer accuracy [52], and thus can provide form verification, although typically not sufficient in itself for optical applications without additional verification.

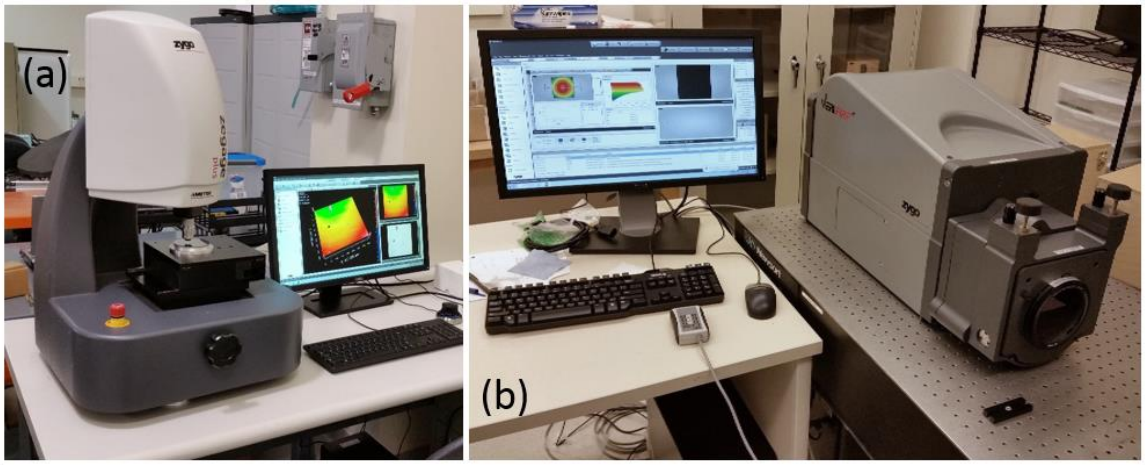

Figure 3.2: (a) Zygo ZeGage Plus (b) Zygo VeriFire ATZ.

3.4 Confocal Raman Microscopy

For subsurface damage measurements, collaboration with Oklahoma State University was leveraged. Confocal Raman microscopy was used to characterize subsurface damage of machined specimens, using a Witec alpha300 RS. This instrument combines a traditional confocal microscope with a high-throughput spectroscopy system which acquires a Raman spectrum corresponding to each image pixel. This instrument can also be configured as an atomic force microscope (AFM) and is equipped to perform scanning near optical microscopy (SNOM). Raman spectroscopy is often used to observe low-frequency vibrational modes of a specimen which are related to molecular and lattice vibrations. The driving mechanisms responsible for Raman scattering are rather complex, and are described in texts such as [53]. An abbreviated description is is given here. When a stabilized laser of very narrow linewidth is incident on the specimen under test, a small number of the incident photons will be scattered via an inelastic process in which interaction with the lattice or molecular modes of the specimen results in a scattered photon with a different, typically lower, wavelength than that of the incident photons. When analyzing the reflected spectra indicates, the Raman shift for

crystalline materials is indicative of the lattice spacing. Changes in lattice spacing due to residual stresses can thus often be correlated to changes in this shift. Similarly, changes in the shape of the peak, particularly quantitative measures of the full width at half maximum (FWHM) of the Raman peak provides a measure of lattice disorder due to subsurface damage.

3.5 Cutting Force Measurement

Cutting forces were measured using transducers and data acquisition equipment as described in this section.

3.5.1 Miniature Cutting Force Dynamometer

During cutting experiments, process forces were measured using Kistler 9256C1 and 9256C2 miniature cutting force dynamometers. These sealed, fluid-proof piezoelectric dynamometers have a measurement range of ±250N, a minimum threshold of 0.002 N, and an unloaded natural frequency of nearly 5 kHz. When loaded with a tool or vacuum chuck assembly, the natural frequency was reduced to approximately 3 kHz, requiring inverse filtering to extend the usable range beyond this frequency limit. Both dynamometers are identical except for the size of the top mounting plate. Charge output was converted to voltage using a Kistler type 5010 dual mode charge amplifier.

3.5.2 Data Acquisition and Analysis

During all experiments, transducers were continuously monitored using a NI USB-2009 data acquisition (DAQ) unit. This DAQ supports simultaneous sampling of up to six channels with an aggregate sampling rate of 50 kHz, and was monitored using a custom virtual instrument (.vi) in LabVIEW 2011. Data was acquired using a NI USB-6251 BNC DAQ, supporting simultaneous sampling of up to eight channels with an

aggregate sampling rate of 1.0 MHz. Data acquisition and post processing was performed using MATLAB® r2013b.

3.6 System Dynamics Identification

A MLI MetalMAX LA package was utilized for identification of structural dynamics of experimental setups. This machine tool characterization package includes small, medium, and large instrumented hammers for stimulus application and accelerometers for response measurement, as well as a data acquisition unit which allows sampling of up to 4 channels at a maximum per-channel rate of 70 kHz. Proprietary software allows application of windowing and averaging during tap testing for system dynamics identification, as well as subsequent prediction of stability lobe diagrams for conventional machining operations. More information about this package can be obtained from [54].

3.7 Diamond Tooling

Cutting mechanics experiments and prototype optical component manufacturing were performed using single crystal diamond (SCD) cutting tools. Many tools were used in conducting the work described in this dissertation, which are described as in the appropriate sections. Because most standard diamond tooling is round-nosed, two specially-designed cutting tools were ordered for orthogonal cutting experiments, and are pictured in Figure 3.3. Orthogonal turning and flycutting tests used a 60° included angle dead-sharp (no radius) single crystal diamond with 10° clearance and 0° rake, brazed to a 55° DCMT-style carbide insert, which was fastened to a steel insert holder. Milling experiments used a 3 mm diameter square SCD endmill with 0° rake, 10° clearance, which was brazed to a 6.35 mm diameter carbide shank.

Figure 3.3: (left) Insert-style turning tool, (right) square SCD endmill.

3.8 Experimental Setups

Cutting mechanics experiments were conducted using three configurations: turning, flycutting, and milling. Specialized fixturing and apparatus were constructed to permit these cutting arrangements.

3.8.1 Turning

Turning experiments were performed in an arrangement, shown in Figure 3.4, where the tool was mounted to an aluminum tooling plate on top of the cutting force dynamometer, which permitted arbitrary orientation of the cutting tool, enabling both outer diameter (OD) and face turning experiments. A specially-designed vacuum chuck was constructed such that both the OD and face of a 30 mm diameter cylindrical workpiece would be fully accessible using the available tooling. To bring the height of the tool's rake face near the centerline of the spindle while maximizing rigidity, the dynamometer was mounted to the top of a 150 mm tall precision-machined cast iron riser block which was attached to the machine table.

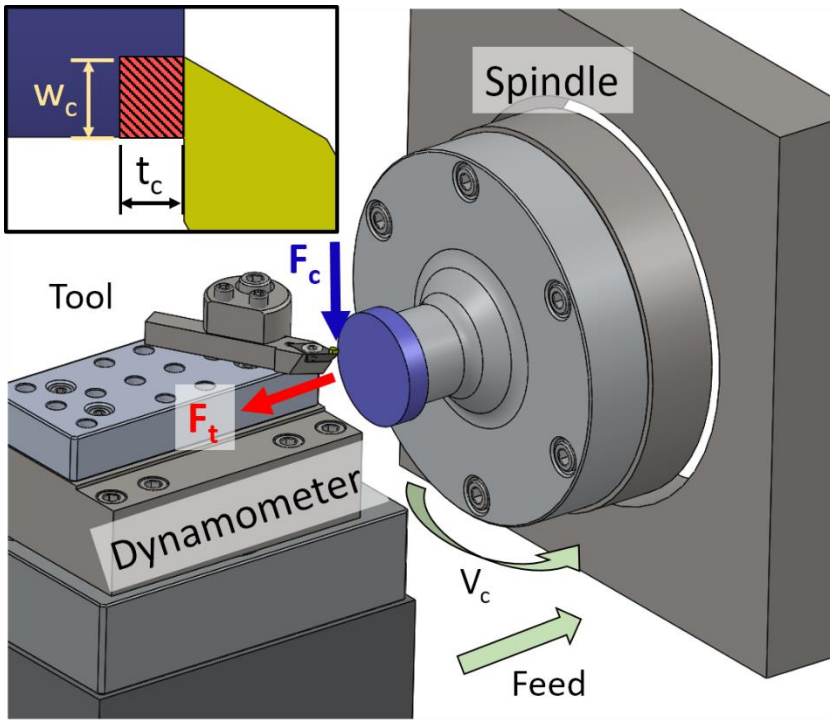

Figure 3.4: Experimental apparatus, force orientation, and (inset) chip geometry detail for orthogonal turning.

3.8.2 Flycutting

To reproduce orthogonal turning geometry in an interrupted cutting configuration, a flycutting setup was designed and constructed, as illustrated in Figure 3.5. In this arrangement, to bring the workpiece near the spindle centerline, the cutting force dynamometer was mounted to a tooling plate which was attached to a vertical cast iron tombstone on top of the machine ways. The workpiece was held by a custom-designed vacuum chuck which was attached to the dynamometer and was intended to be machined flat in place before each use.

A 6061 aluminum flycutter was mounted to the main spindle of the Moore 350FG. Slots in the flycutter held steel tooling blocks which were designed to present the 60° insert-style turning tool on center at 0° rake and 0° side cutting edge angle, with the tool tip nominally 50 mm from the spindle centerline. This geometry allowed relatively

high surface speeds to be achieved at low spindle rotational rates, reducing vibrational effects due to the unbalanced flycutter. Interchange of the tooling blocks allowed the mounting of a variety of other turning tools in the flycutter for in-situ specimen preparation.

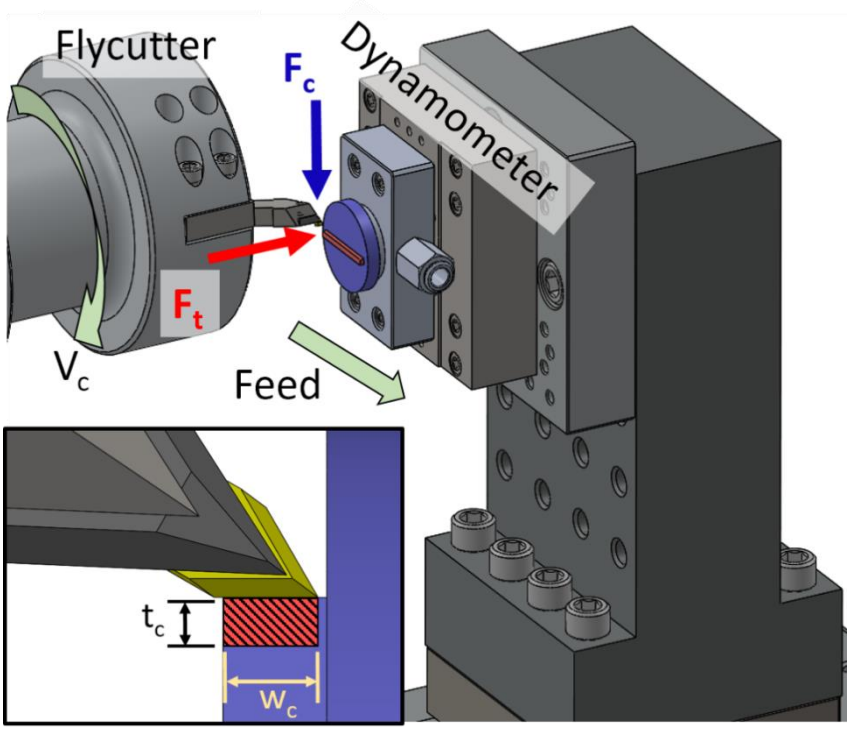

Figure 3.5: Experimental apparatus, force orientation, and (inset) chip geometry detail for orthogonal flycutting.

Though not visible in the figure, improved balancing was obtained with a dummy tool shank mounted opposite the actual tool.. Further, Set screws around the periphery of the flycutter (also not shown) allow balancing adjustment, and a center-mounted ER-16 collet holder permitted low-speed milling operations if desired; for example the flycutter could be used to face cut the vacuum chuck. Due to balance considerations, this flycutter was intended to operate at spindle speeds below 2000 rpm, and was designed to

rotate clockwise so that chips would naturally be ejected downward from the cutting zone, improving the ease of collection.

3.8.3 Milling

To facilitate milling experiments, in which the high-speed milling/grinding spindle was used, a mount was constructed, shown in Figure 3.6, to attach the dynamometer to the main spindle of the diamond turning machine, which was locked in place in C-axis mode during milling operations. A smaller vacuum chuck was designed to hold the specimen while minimizing mass upon the dynamometer and thus maintaining a higher force measurement bandwidth. If desired and necessary, the dynamometer could be electrically isolated from the spindle using a polycarbonate spacer with minimal loss in rigidity.

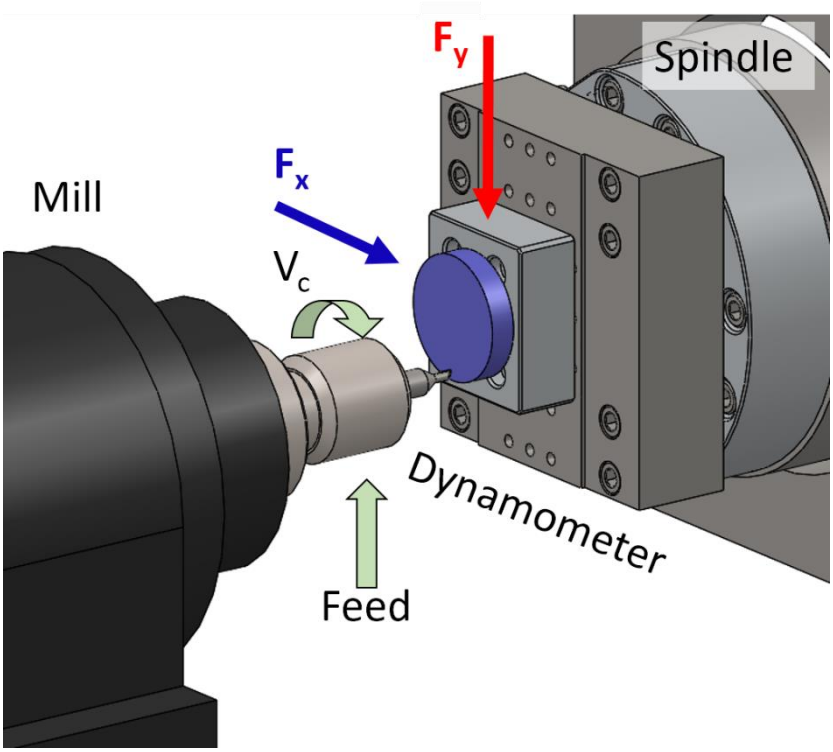

Figure 3.6: Experimental apparatus and force orientation for milling.

CHAPTER 4: DIAMOND MACHINING OF IRG 26

4.1 Introduction

In this chapter, cutting mechanics experiments are discussed for an arsenic-selenium ($As_{40}Se_{60}$) chalcogenide glass, trade name IRG 26, from the Schott IRG series of AsGeSe glasses. With a relatively high refractive index of 2.801 at 3.0 μm wavelength and greater than 50% transmission from 1 μm to 12.5 μm, this glass is an appropriate choice for many infrared (SWIR to LWIR) applications. Relevant material properties for this glass are presented in Table 4.1. The absence of germanium from the composition facilitates a wider transmission spectrum than other glasses in the product range.

Table 4.1: IRG 26 material properties, from [55]

Density	4.93 g/cm^3
Thermal expansion coefficient	2.08 x 10^{-6}/K
Transition temperature	185 °C
Hardness	1.04 GPa (Knoop)
Young's modulus	18.3 GPa

Although this glass is a brittle material, it can be processed under appropriate cutting conditions by diamond turning and milling in addition to conventional grinding and polishing. The relatively low glass transition temperature makes production by molding another viable processing option. Typical spindle speeds for turning operations are from approximately 1000 rpm to approximately 5000 rpm. Cutting velocities vary with part diameter but are often between 1 m/s and 5 m/s. Surface velocities up to 10 m/s

are encountered in milling operations, depending on tool diameter, but at much higher spindle speeds, typically between 20,000 and 50,000 rpm. Operator experience suggests that some materials can be machined in a fracture-free manner by diamond milling, but not as successfully by diamond turning. During the short tool-workpiece interaction times (often on order of 100 μs) encountered in milling operations, this anecdotal evidence suggests that cutting mechanics in highly dynamic milling operations may differ from those seen during turning operations which are nearly steady-state.

To understand the behavior of this IRG 26 under different cutting conditions, process forces were measured during turning, flycutting, and milling experiments. These process forces were compared to mechanistic predictions using cutting force coefficients obtained from orthogonal cutting data. Further, surface finish, texture and integrity were examined and related to cutting parameters using SWLI and digital microscopy. The results of these experiments indicated that when chip thickness exceeds approximately 600 nm during orthogonal cutting processes, the material exhibits a transition from a ductile-dominated cutting mode, where material removal is dominated by plastic deformation, to a brittle-dominated mode driven by fracture propagation. This critical chip thickness was shown to vary slightly in response to cutting velocity, but to be invariant with tool-workpiece interaction time. During round-nosed cutting, the transition was observed to occur at higher feed rates than expected, which could be attributed to cutting behavior in regions of slowly-varying chip thickness or to tool edge condition. Using tooling with high negative rake angles enabled higher feed rates and increased material removal rates while still maintaining a ductile-dominated cutting. The

findings of this chapter were used to select cutting conditions for the manufacture of a freeform lens pair which is detailed later in this dissertation.

4.2 Orthogonal Turning

Orthogonal turning experiments were performed on a cylindrical sample of IRG 26 with an outer diameter of 30 mm using the experimental setup described in Section 3.8.1. The test configuration is shown in Figure 4.1. Although brittle materials are typically turned using negative-rake tools or by appropriately tilting a zero-rake tool [56], fracture-free surfaces are also produced in IRG 26 with 0° rake angle, as used in these experiments. These experiments were conducted using the insert-style 60° tool described in Section 3.7.

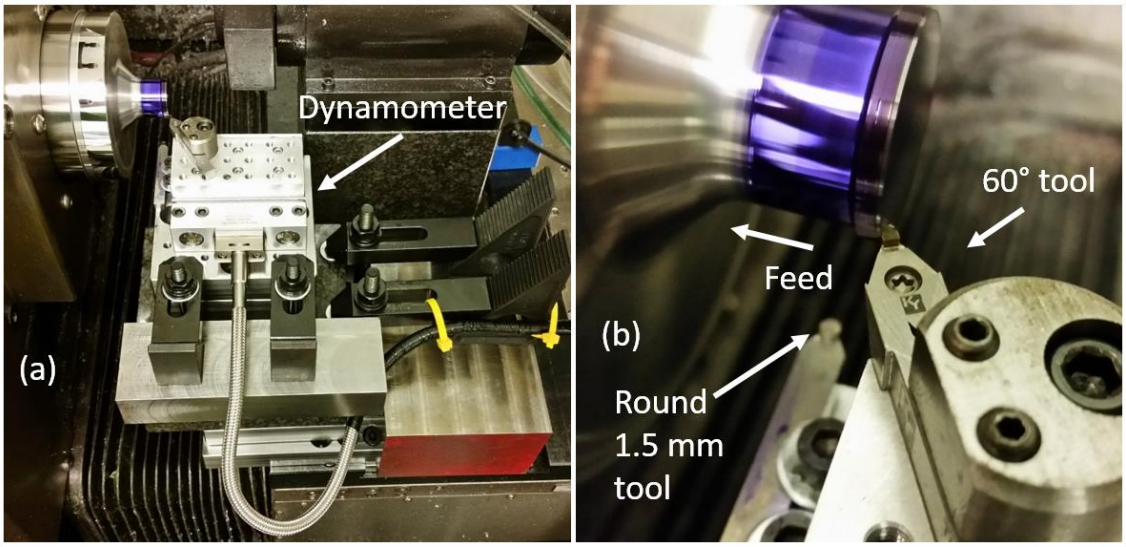

Figure 4.1: (a) Test configuration for orthogonal turning and (b) enlarged view of tool, specimen, and cutting zone.

4.2.1 Influence of Chip Thickness on Cutting Mechanics

The effect of chip thickness on cutting behavior was investigated at a constant cutting velocity of 2 m/s, corresponding to 1300 rpm, at the outer diameter of the workpiece. Chip width, w_c, was held constant at 100 μm for all experiments, while chip

thickness, t_c, was varied between 200 nm and 2.0 μm. Before any experiments were performed, the vacuum chuck was centered on the spindle as well as possible, the specimen was centered on the chuck, then the outer diameter and face of both were diamond machined in-situ to improve balance. Before cutting tests, and as necessary between tests, 200 μm of material was removed from the outer diameter of the specimen using a 1.5 mm radius round-nosed turning tool to remove any accumulated damage from previous machining operations.

In [47], a discontinuity or 'hysteresis' effect was seen in during orthogonal turning of this glass. The location of the ductile-brittle transition varied based on whether experiments were performed in order of ascending or descending chip thicknesses. It was believed that the forward propagation of cracks into the workpiece subsurface was responsible for this phenomenon. For the tests described in this section, 500 revolutions of cutting at t_c = 100 nm were performed between each experiment to minimize the effects of accumulated damage on subsequent tests. After removal of previous damage, for each set of cutting conditions, 80 revolutions of cutting force data were sampled at 500 kHz. Two sets of experiments were performed in order of ascending chip thickness, and two sets were performed in descending order, for a total of four experiments at each chip thickness. A 3rd order low-pass Butterworth filter was applied in MATLAB® with a cutoff frequency of 250 Hz to remove dynamic effects from the tool and dynamometer.

Figure 4.2 shows measured cutting and thrust forces at chip thicknesses of 200 nm and 1.2 μm. At t_c = 400 nm, forces increased linearly over one revolution as the tool enters the material (lead-in), then remained constant throughout the cut, indicating a ductile-dominated cutting mechanism. Forces then dropped rapidly as the tool dwelled at

the end of the cut (lead-out) and retracted. At t_c = 1.2 μm, when the tool entered the material, forces jumped to approximately 3x those at t_c = 400 nm, then began to drop off rapidly, remaining at a much lower level for the remainder of the cut. This force behavior indicates successful removal of accumulated subsurface fracture before the experiment, and a cut which began in a ductile-dominated mode, then after several revolutions of cutting, experienced a transition to brittle-dominated cutting mode due to forward propagation of subsurface cracks.

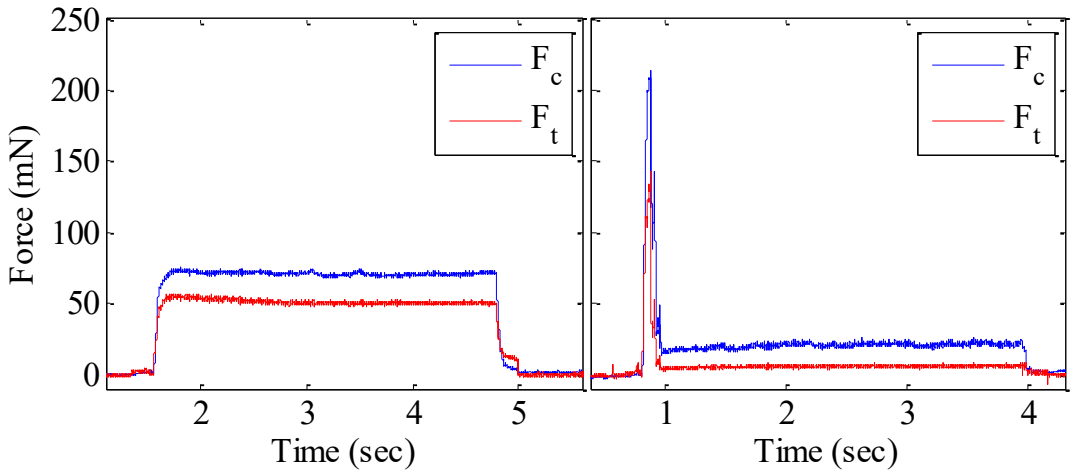

Figure 4.2: IRG 26 turning forces at v_c = 2 m/s. (right) t_c = 400 nm, (left) t_c = 1.2 μm.

The filtered data from each cutting experiment was trimmed to isolate only the portion after steady-state behavior had been reached (i.e. in the case of t_c = 1.2 μm as shown in Figure 4.2, only the portion between 1.2 sec and 3.8 sec would be retained.) After isolating the relevant data segments, mean cutting and thrust forces were computed for each experiment. Results are shown in Figure 4.3. Cutting experiments performed in order of ascending chip thicknesses are indicated by triangles, while those performed in descending order are indicated by circles. Agreement was seen between experiments at each chip thickness, regardless of test ordering.

At values of t_c below 600 nm, as indicated by the black lines, cutting and thrust forces increased approximately linearly with chip thickness, indicating a ductile-dominated cutting regime, while forces were much lower and nearly constant above this critical chip thickness, suggesting a brittle-dominated cutting mechanism due to cracking. Within the brittle-dominated regime, the force dropoff shown in Figure 4.2 occurred more rapidly as chip thickness increased, consistent with the notion of fracture due to forward-propagated damage. At higher chip thicknesses, the crack propagation depth was deeper, so fewer revolutions of cutting were necessary for cracks to grow longer than the commanded chip thickness and initiate irreversible brittle fracture.

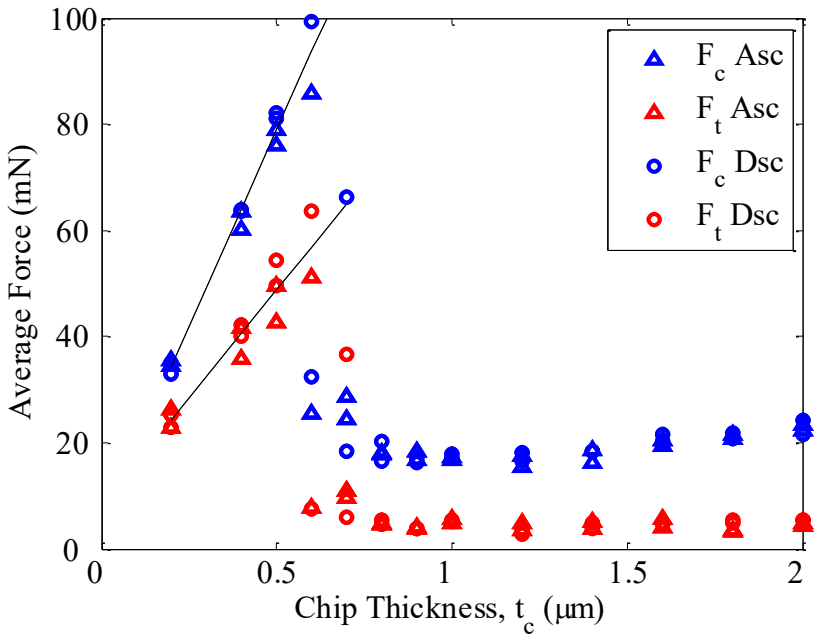

Figure 4.3: IRG 26 at v_c = 2 m/s, average cutting forces vs. chip thickness.

For t_c values of 600-700 nm, the force dropoff rate was low enough that 80 revolutions of cutting was sometimes insufficient to reach steady state cutting behavior. Thus, some data points indicating ductile-dominated cutting at these chip thicknesses are seen in Figure 4.3. Further study of the behavior in this transition zone is warranted; it

would be helpful to more completely understand the mechanisms that cause the transition and if the transition to fracture-dominated cutting could be controlled or prolonged to a higher (and more productive) uncut chip thickness.

To determine cutting force coefficients, linear regressions were performed over the ductile-dominated cutting regimes, indicated by black lines in Figure 4.3. Average cutting and thrust force coefficients of K_c = 1489±62 N/mm^2 and K_t = 816 ±71 N/mm^2 were found. Cutting coefficients are plotted as a function of t_c in Figure 4.4, again illustrating a sharp decrease in force level above a chip thickness of approximately 600 nm. The direction of the cutting force vector was also calculated for each set of cutting conditions. As chip thickness increased, the direction of the resultant force vector rotated towards the direction of cutting velocity, indicating a less shearing-dominated cutting condition.

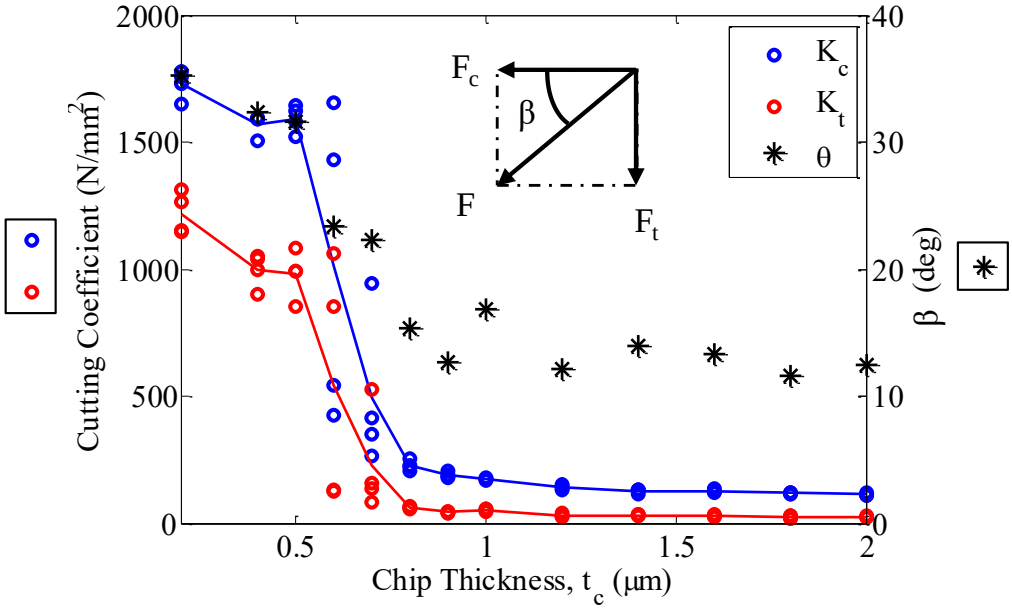

Figure 4.4: IRG 26 orthogonal turning cutting coefficients at v_c = 2 m/s.

A SEM study of chip morphology is presented in Figure 4.5. At t_c = 200 nm and 400 nm, collected chips were long and curly, similar in form to those encountered when cutting ductile metals. At higher chip thicknesses of 1.0 μm and 1.4 μm, chips were short, broken, and powder-like, confirming a fracture-based material removal mechanism.

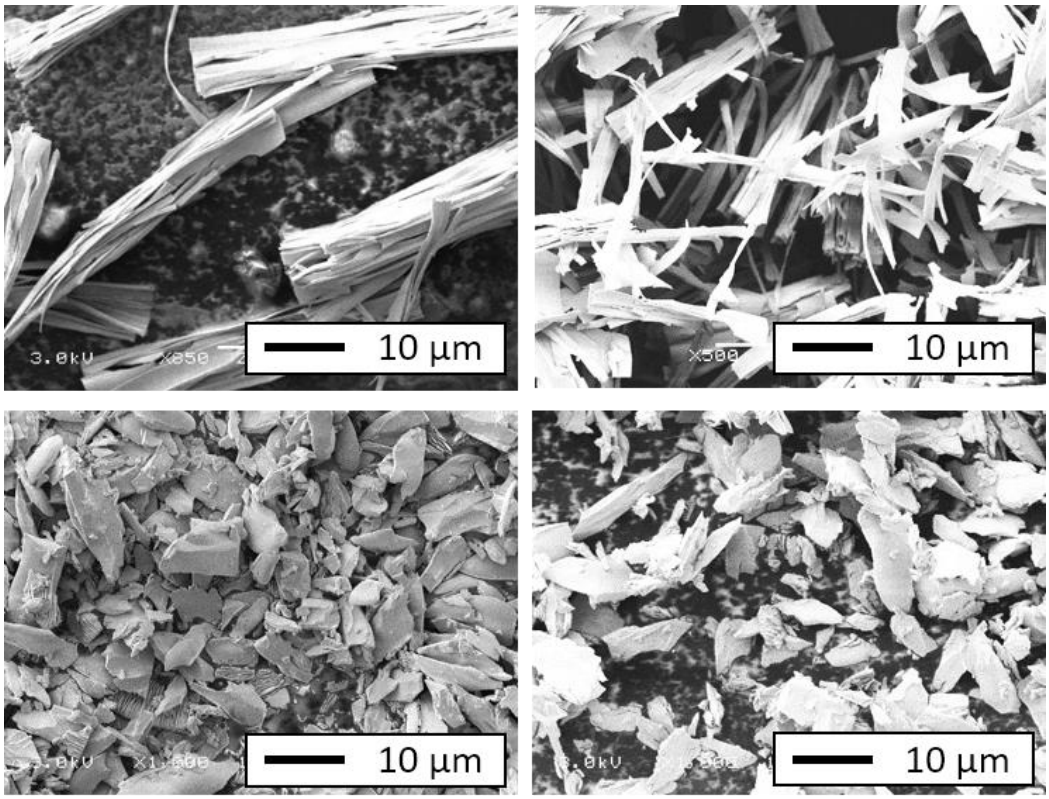

Figure 4.5: SEM micrographs at 3000x magnification of chips from orthogonal turning experiments. Clockwise from top right: t_c = 200 nm, 400 nm, 1.0 µm, 1.4 µm.

Although cutting coefficient values were in agreement with previous work, the critical chip thickness value of t_c = 600 nm reported was lower than the value of approximately 1 µm reported in [47] [50]. Possible causes are material inhomogeneity and/or tool edge condition (edge radius). The specimen used in these orthogonal turning experiments originated from a different batch/melt of glass than that of the specimens used in the previous work. Although all experiments presented in Figure 4.3 were performed on a single specimen, further turning experiments performed on several pieces of glass from the same melt confirmed a critical chip thickness of t_c = 600 nm. These experiments were performed using a brand new tool, while the edge condition of the tool used in the cited work is unknown. Any cutting edge deterioration (flank wear, edge rounding, or build-up-edge) would present an effective negative tool rake to the

workpiece, which could act to suppress brittle fracture, increasing the critical chip thickness [39] [57] [40]. SEM examination in Figure 4.6 of tool edges before and after orthogonal turning experiments did not show evidence of significant cutting edge deterioration.

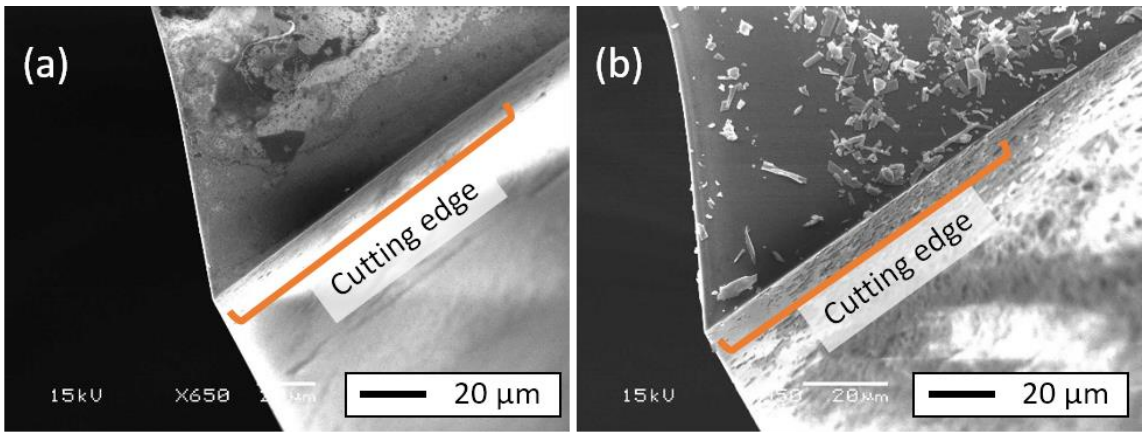

Figure 4.6: SEM micrographs at 650x of (a) new tool cutting edge, (b) cutting edge after orthogonal turning experiments.

4.2.2 Influence of Cutting Velocity on Cutting Mechanics

The orthogonal turning experiments described in Section 4.2.1 were repeated using the same tool and workpiece at cutting velocities from v_c = 0.5 to 8.0 m/s. Three experiments were performed at each chip thickness. Experimental sets were performed in order of descending cutting velocity, such that higher cutting speeds were tested at larger diameters, to reduce the required spindle speed, and thus minimize the effect of rotational imbalance on the cutting process. Cutting coefficients were calculated at t_c = 400 nm and are shown as a function of v_c in Figure 4.7. Error bars on the figure extend one standard deviation above and below the mean values. Broken black lines indicate the average coefficient values of K_c = 1489 N/mm^2 and K_t = 816 N/mm^2 calculated from Figure 4.3. Cutting coefficients were in general higher than those for aluminum alloy

6061, as tabulated in references such as [48] [49]. At this constant chip thickness, no trend could be identified between cutting velocity and cutting coefficients.

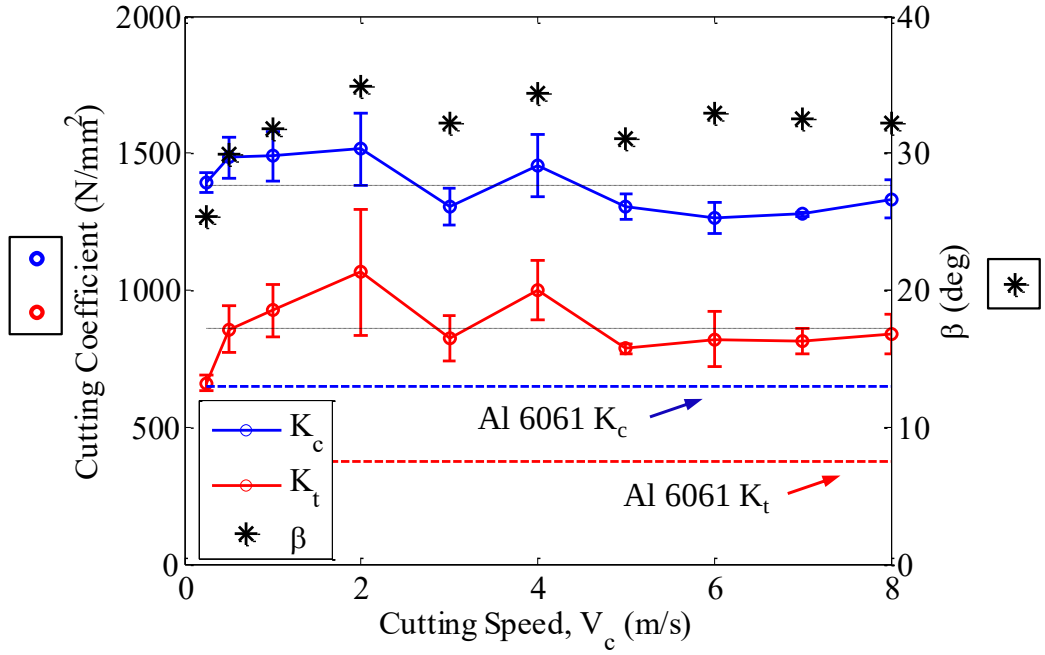

Figure 4.7: IRG 26 orthogonal turning cutting coefficients at t_c = 400 nm.

Cutting and thrust forces are shown as a function of chip thickness in Figure 4.8 for several cutting velocities. Over the ductile-dominated cutting regime, visual inspection of Figure 4.8 confirms that there is little variance of cutting coefficients with cutting velocity. Below t_c = 500 nm, a standard deviation of 8 mN was observed, while a higher standard deviation of approximately 30 mN was apparent through the transition region of t_c = 500-800 nm, similar to the behavior observed in Figure 4.3. At higher cutting velocities, the critical chip thickness decreases slightly to an approximate value of 550 nm. While this slight decrease could be due to material properties, it could also be a result of process dynamics. Tool vibration will always be present, causing the instantaneous chip thickness to fluctuate about the nominal, commanded value. Further, the spindle-vacuum chuck-workpiece system will always exhibit some amount of

rotational imbalance. Depending upon system dynamics, increased rotational rates could lead to increased tool vibration, which if large enough could also result in an earlier onset of fracture and an apparent reduction in critical chip thickness.

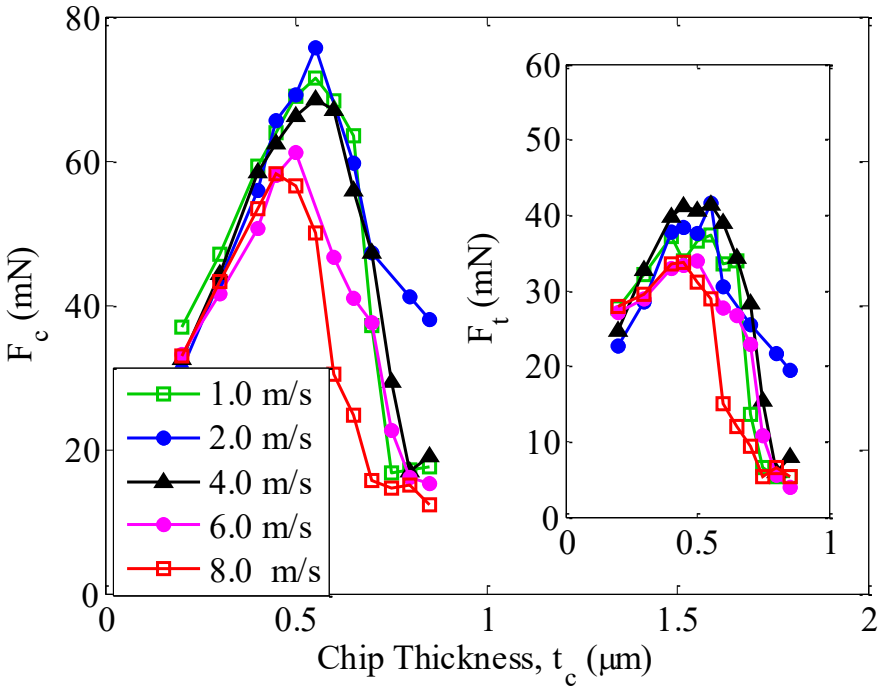

Figure 4.8: IRG 26 cutting and thrust forces as a function of cutting velocity.

4.3 Oblique Turning

Next, the tool was rotated by an angle χ to generate an oblique turning configuration. Experiments were performed on an alternate IRG 26 workpiece from the same material batch. The tool was the same as that used in the orthogonal turning experiments. Cutting velocity was held at 2 m/s, corresponding to 1320 rpm, while depth of cut, d_a, was held at 100 μm. Feed per revolution, f_t, was varied from 200 nm to 2.0 μm. Side cutting edge angles of 15° and 30° were tested. Additional experiments at 0°, identical to orthogonal turning geometry, were performed as a baseline. Four experiments were performed at each feed rate, and 80 revolutions of cutting data, sampled at 100 kHz, was post-processed using a 3rd order Butterworth 250 Hz low-pass

filter. For all experiments, F_a was directed along the least-sensitive direction of the dynamometer, and was inherently noisier. Selected force signals and frequency spectra are presented in Figure 4.9 for the case of 15° side cutting edge angle.

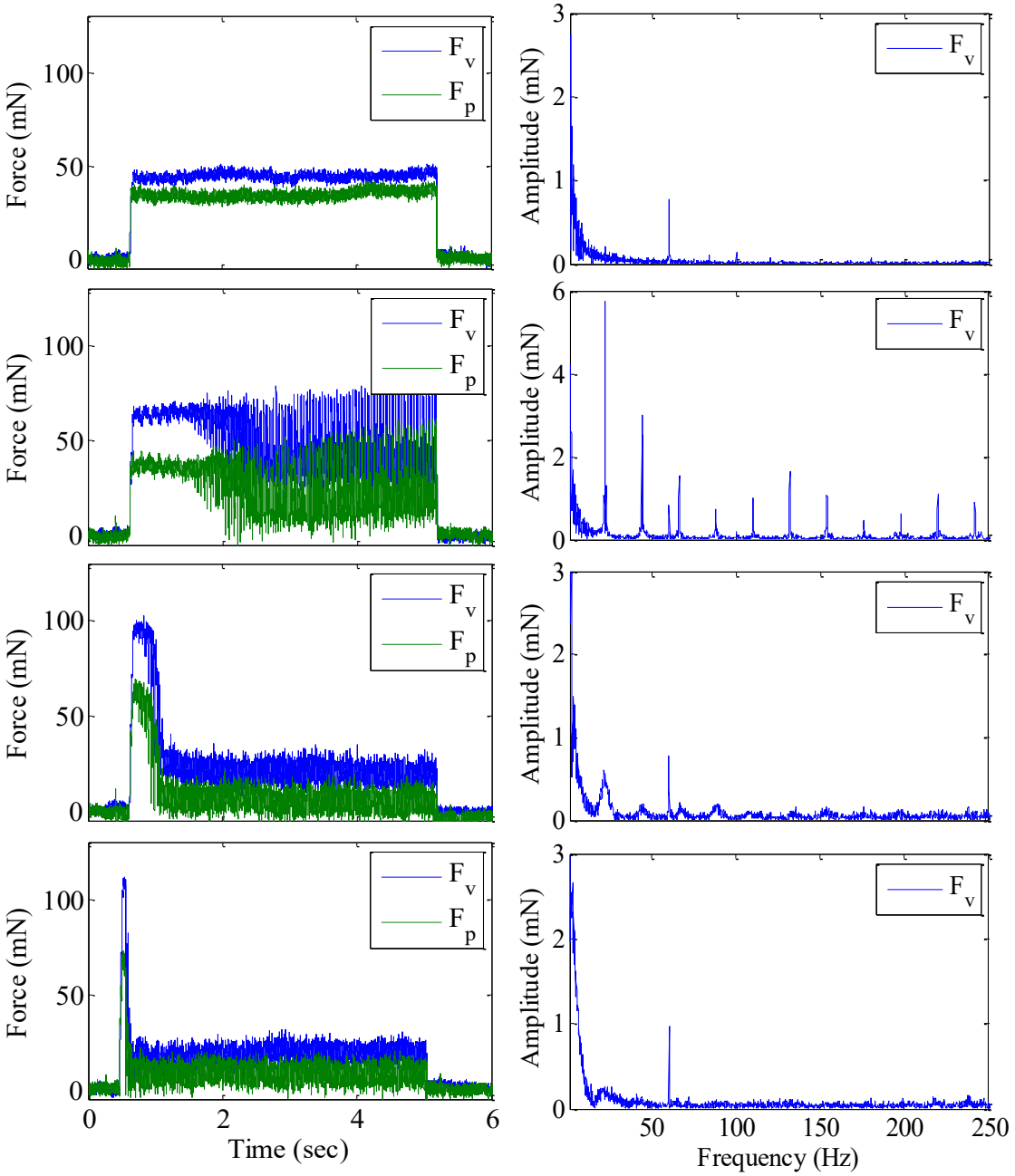

Figure 4.9: Force signals and frequency spectra for IRG 26 15° oblique turning. From top to bottom, 300, 500, 700, 900 nm/rev feedrates.

The force signal at a feed rate, f_t, of 300 nm per revolution was very similar in behavior to that shown in Figure 4.2, with spectral content dominated by low-frequency components and 60 Hz electrical noise. However, at f_t = 500 nm, harmonics of the 22 Hz spindle rotational frequency were apparent, suggesting a circumferential material

inhomogeneity in which one region of the workpiece was still cutting in a ductile-dominated mode, while the remainder exhibited a fracture-dominated material removal mechanism. This phenomenon was not noticeable during the experiments performed in Section 4.2, suggesting material variation even within a single batch. Only the first 22 Hz harmonic was prominent in the signal at f_t = 700 nm, and at f_t = 900 nm, the entire workpiece exhibited a consistent behavior, again dominated by low-frequency sources and electrical noise.

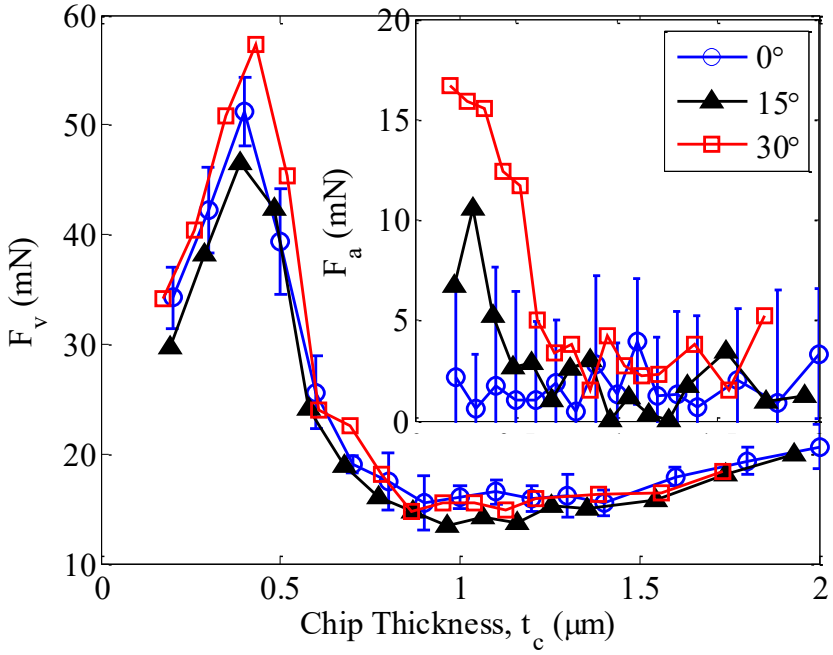

Figure 4.10: IRG 26 average forces as a function of chip thickness for oblique turning.

Average cutting forces are shown as a function of chip thickness in Figure 4.10. Error bars indicate one standard deviation above and below the mean values for the 0° case. Over the text domain, critical chip thicknesses were not observed to change in response to side cutting edge angle. F_v was generally invariant to side cutting edge angle, as cross-sectional chip area remains constant for a fixed depth of cut and feed per revolution, regardless of the value of χ. However, Fa clearly exhibits the effect of the

oblique rotation which induces a rotation of the force components in the plane perpendicular to the cutting velocity.

4.4 Round-nosed Turning

Round-nosed face turning experiments were conducted using single crystal diamond turning tools of various rake angles on several workpieces from the same batch/melt of IRG 26 as used in previous sections.

4.4.1 Zero Rake Tooling

Zero-rake round-nosed face turning experiments were performed in a configuration identical to that shown in Figure 2.3. A 1.0 mm radius turning tool was mounted atop the Kistler 9256C1 cutting force dynamometer. Cutting speed and depth of cut were held constant at 2 m/s and 10 μm, respectively, while feed per revolution was varied from 2 to 16 μm. A light mist of mineral oil lubrication was applied to improve chip evacuation and resulting surface finish. Three sets of experiments were performed at each feed rate, and are presented in Figure 4.11. For each experiment, 100 revolutions of cutting data were sampled at 100 kHz and mean force levels were determined after applying a 3rd order Butterworth low-pass filter with a cutoff of 250 Hz. Force levels for the zero-rake case were predicted using the orthogonal turning data from Figure 4.4 and Eq. 2.7. Predictions carried out using mean values of cutting coefficients are shown with broken lines, while the shaded bands represent a ±1 standard deviation variation in cutting coefficients. For all experiments performed, F_p was oriented along the least-sensitive direction of the cutting force dynamometer, and was dominated by electrical noise.

The experimental and predicted values show acceptable agreement below feed rates of approximately 5 μm pre revolution. At higher feed rates, the local uncut chip thickness exceeded the critical value of approximately 600 nm, and the orthogonal turning data predicts the onset of irreversible brittle fracture, which would be accompanied by a decrease in force level. However, the experimental data exhibited the corresponding decrease in force level at a much higher feed rate than predicted.

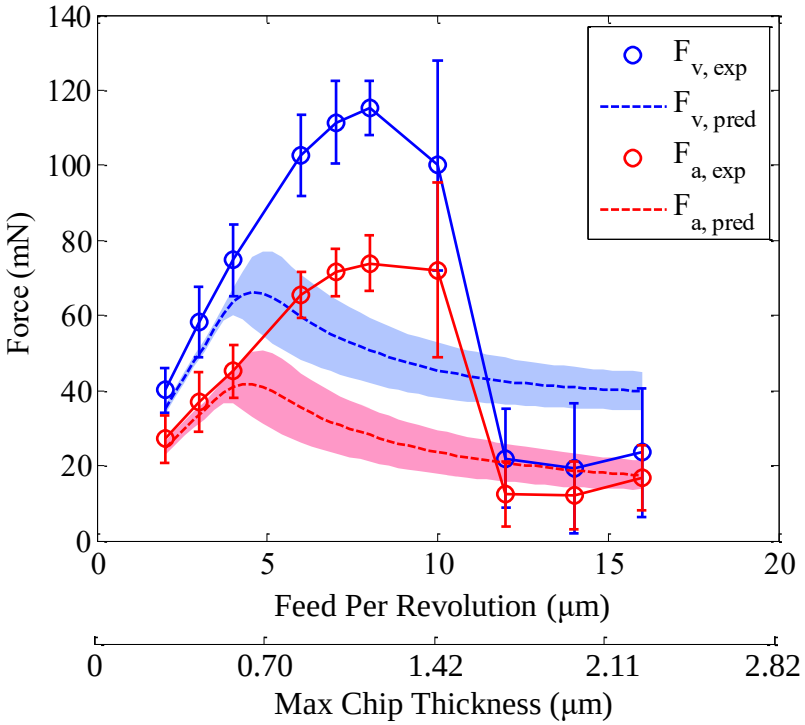

Figure 4.11: IRG 26 round-nosed face turning forces and predicted values.

This disagreement between prediction and experimental result could be caused by several effects. First, the edge condition of the tool used was not precisely known. While examination of the tool using optical microscopy did not indicate appreciable chipping or other damage, such examination was incapable of measuring the tool edge radius, which if large enough (typically on order of 100 nm or less for diamond tools) could induce an effective negative rake angle near the cutting zone, which would be

expected to result in an increased critical chip thickness. Second, the shallow depth of cut and large tool radius impose effective side cutting edge angles on order of 80° in this configuration. While the oblique turning experiments presented in Section 4.3 did not suggest a change in cutting behavior with side cutting edge angle over the range tested, such change may be evident at much higher angles. Third, a sharp, abrupt transition from ductile-dominated to brittle-dominated cutting behavior was observed during orthogonal and oblique turning, in which the chip thickness was constant throughout the entire chip. However, during round-nosed machining operations where the chip thickness varies across the tool nose, a single critical chip thickness corresponding to the transition may be impossible to clearly define. In regions where the local chip thickness was slowly-varying, a wider and more continuous transition zone may exist.

4.4.2 Negative Rake Tooling

The experiments described in the previous section were repeated using a -25° rake turning tool which was mounted directly to the dynamometer or was mounted using a specially-designed rake adapter plate, shown in Figure 4.12, to produce a -50° rake. Surface speed and depth of cut were once again maintained at 2 m/s and 10 μm, while feed per revolution was varied over a large enough range to detect the transition from ductile-dominated to brittle-dominated machining behavior for each rake angle. Again, three experiments were performed at each feed rate and were post-processed using a low-pass Butterworth filter with 250 Hz cutoff. Values of F_p were below the dynamometer noise threshold for all experiments.

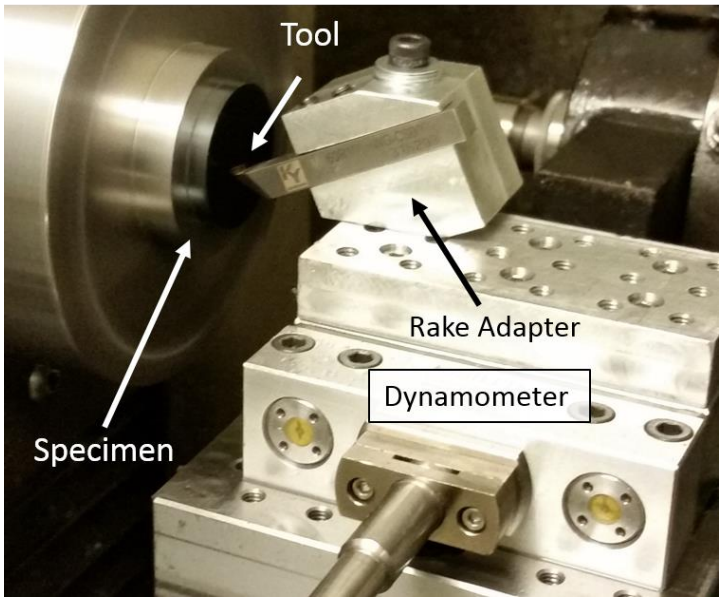

Figure 4.12: IRG 26 round-nosed turning setup, -50° rake.

Average forces are plotted in Figure 4.13 for all rake angles. It can be observed that higher negative rake angles result in an increased critical chip thickness. This is consistent with the notion that negative rake angles produce localized regions of high hydrostatic pressure near the cutting zone and suppress crack growth and propagation, as described in [37]. At zero rake, the magnitude of F_v was larger than that of F_a regardless of feed per revolution, yet at -25° rake and -50° rake, F_a was larger than F_v. This crossover of force components was consistent with that observed in [58], and can be observed more easily in Figure 4.14 which shows the angle of the cutting force vector β. The increase in β is is consistent with increased compressive stress applied to the workpiece material at higher negative rake angles.

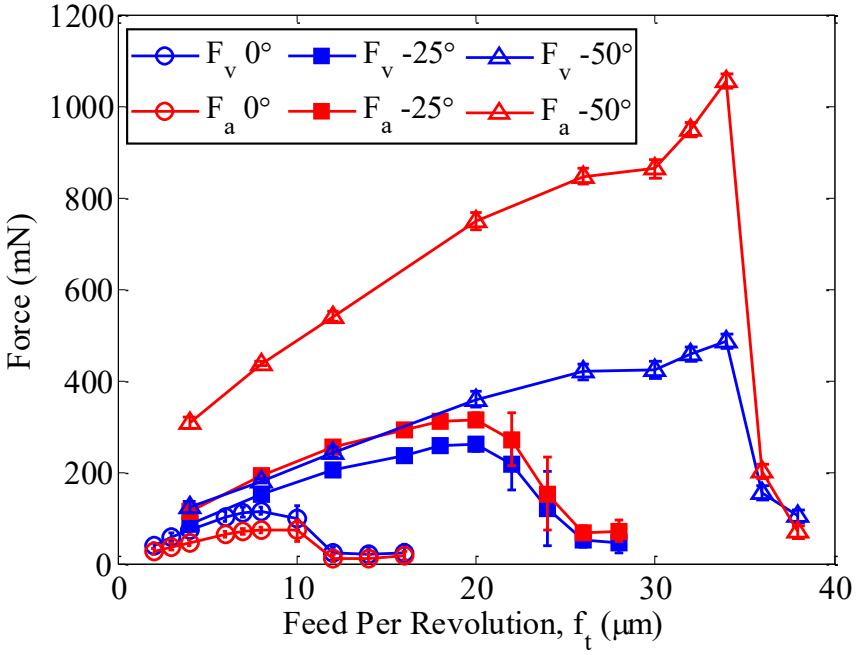

Figure 4.13: IRG 26 round-nosed turning forces.

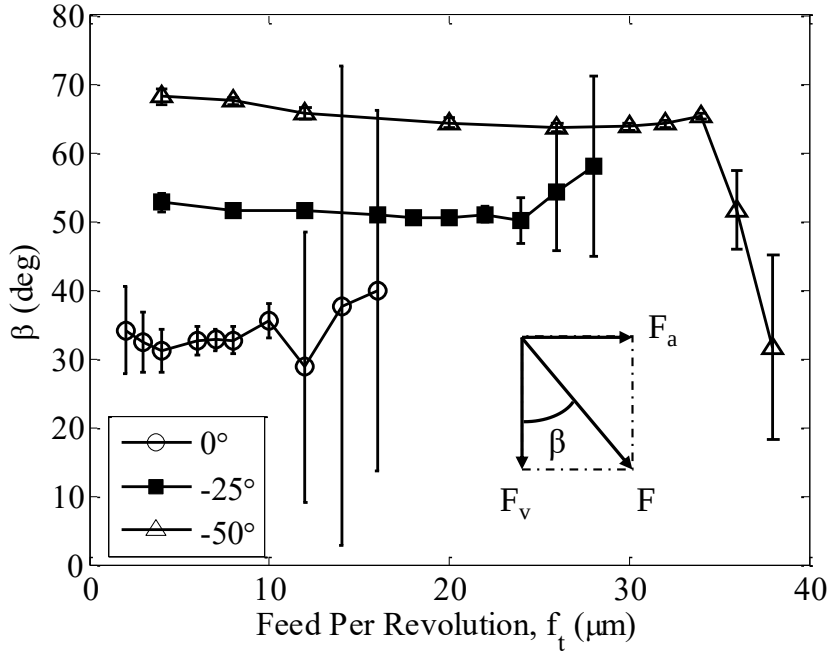

Figure 4.14: IRG 26 round-nosed turning resultant force angle.

After cutting force measurements were performed using a given tool, a series of 0.7 mm wide bands was machined on the face of each specimen at 10 µm depth of cut

and feed per revolution identical to the values used in cutting mechanics experiments. The tool was then plunged slightly into the workpiece at appropriate locations to demarcate the band boundaries. Digital microscope images of the banded specimens are shown in Figure 4.15. At zero rake, the onset of surface fracture was apparent at a feed rate of 7 μm/rev, and the fraction of the surface showing fracture increases sharply with feed rate. The onset of significant surface fracture occurred at a higher feed rate for -25° rake, and a generally less-fractured surface was apparent. At -50° rake, surface fracture was not discernible at this low magnification, although a clearly-defined cusp-like structure from the tool nose radius was evident at the highest feed rates.

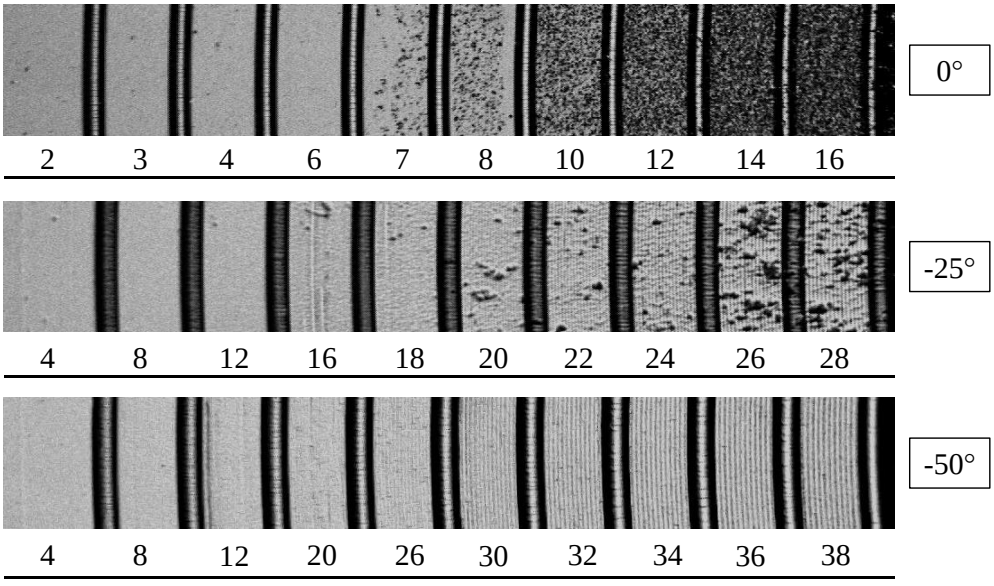

Figure 4.15: Digital microscope images at 5X of IRG 26 banded specimens turned using 0°, -25°, and -50° rake tooling. Bands are 0.7 mm wide.

SWLI examination of the banded specimens was also performed using a 20X Mirau-type interferometric objective. Figure 4.16 presents areal roughness, Sa, as it varies with feed rate for the three specimens. Selected micrographs from the zero-rake specimen are also presented for comparison. At low feed rates, the surface texture was

dominated by a cusp-like structure due to the feed motion of the tool (some debris is also visible). As feed rate increased, the surface topography began to be affected by the presence of pits and cracks in the material, resulting in a much higher surface peak to valley height. As feed increased to cause brittle fracture, the surface was dominated by pits and voids.

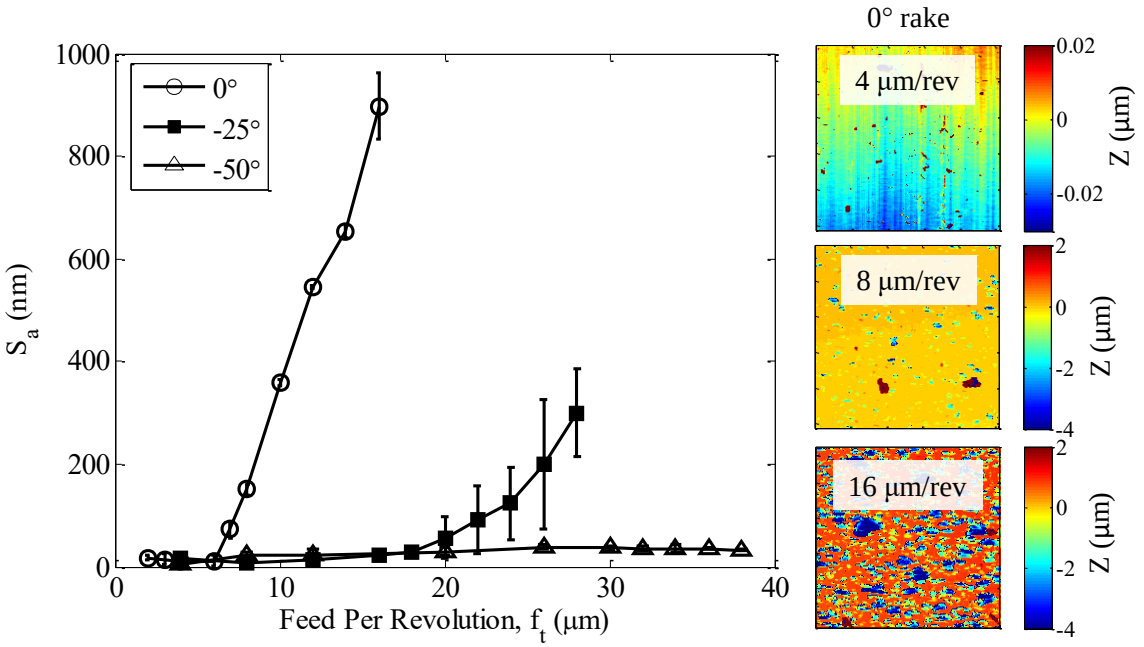

Figure 4.16: (left) IRG 26 round-nosed turning Sa, (right) SWLI micrographs of zero-rake specimen at 4, 8, and 16 µm/rev feed. 408 µm square FOV. Error bars are present, yet are not discernible at certain data points.

Although the SWLI is typically used only for assessing surface topography by observing modulation of interference fringes, the instrument's detector array is also capable of measuring the intensity of light reflected from a specular surface and constructing an intensity map of that surface. Based on this capability, a new metric of surface integrity, RI_{80}, is proposed. This is defined as the area fraction of the surface for which the reflectivity is greater than 80% of the bulk reflectivity for a diamond turned surface free of fracture (i.e. the fraction of the surface where the intensity incident upon

the SWLI detector was greater than 80% of that experienced when observing a fracture-free region of the specimen.) Characterization of surfaces by RI_{80} stipulates that all measurements are performed using the same illumination intensity. RI_{80} is presented in Figure 4.17 for the banded specimens, and selected intensity maps are shown for the zero-rake specimen. For these measurements, RI_{80} was computed with respect to the band turned with the 0° rake tool at 2 μm/rev. Again, at lower feed rates, very few cracks or pits were present, resulting in a bright, highly-reflective surface. As feed increased, the area percentage of the map covered by pits and voids increased, resulting in a less reflective surface and a darker intensity map. The results of Figure 4.17 agree with those in Figure 4.16, but RI_{80} was found during the measurement process to be a more robust metric for quantifying surface integrity, as the presence of dust or contamination can easily distort areal roughness values for very smooth surfaces. Agreement between the trends in Figure 4.15 and Figure 4.17 is evident.

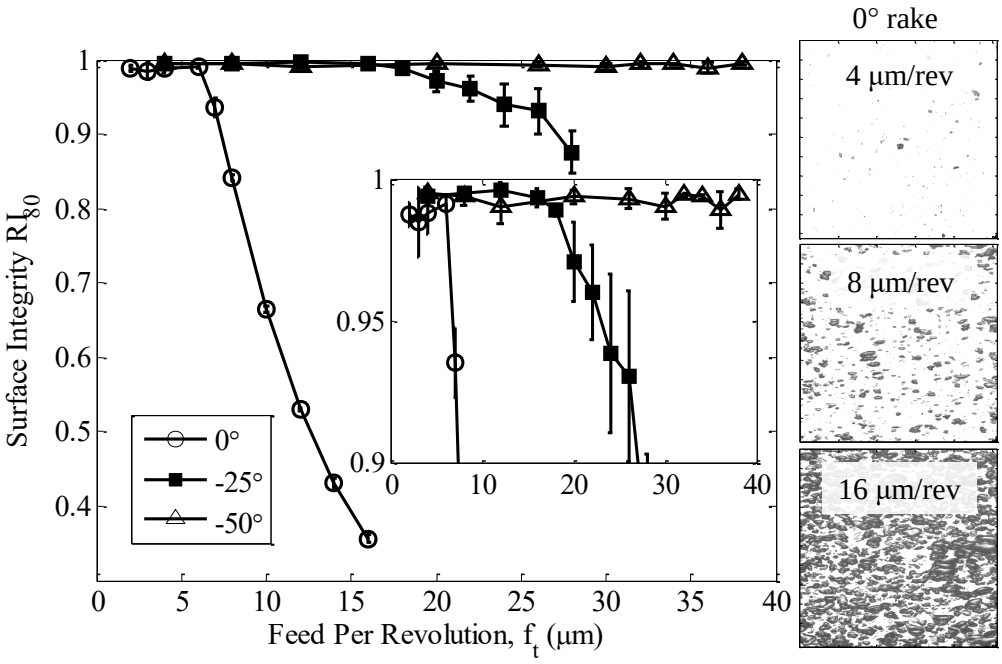

Figure 4.17: (left) IRG 26 round-nosed turning surface integrity as indicated by RI_{80}, (right) SWLI intensity maps of zero-rake specimen at 4, 8, and 16 μm/rev feed. 408 μm square FOV. Error bars are present, yet are not discernible at certain data points

4.4.3 Sine Wave Plate

Although negative rake angles can inhibit fracture in machining of brittle materials, the variation in surface geometry of a given component will cause an unavoidable variation in local effective rake about the nominal tool value when performing STS or FTS operations [59]; that is, the tool will be moving over a curved surface and the variations in the local surface normal will cause a variation in the instantaneous rake angle. Thus, depending upon geometry, for a zero rake tool, it is the effective rake angle will assume slightly positive values in certain regions of a freeform optic. However, due to potential tool interference and other process geometry limitations described further in Section 6.2, such positive effective rake angles would be no larger than the tool clearance angle, typically on order of 5-7°.

To investigate the effect of small positive rake angles on cutting behavior, an annular region of an IRG 26 workpiece was machined by STS to the sinusoidally varying form described by Eq. 4.1 between part radii of 10 and 15 mm; this part was termed a sine wave plate. During machining of this component using zero-rake tooling, the effective rake angle cycled between +3° and -3° three times per revolution. Finish passes were performed with a 5 μm depth of cut and a 10 μm stepover per revolution.

$$z(\rho, \phi) = 0.2358 \cos(3\phi) \qquad \text{Eq. 4.1}$$

The completed sine wave plate and results of subsequent SWLI analysis are presented in Figure 4.18. SWLI images at 50X magnification indicate clear cusp-like structure due to feed marks from the tool. The annular machined region was shiny and highly reflective, while the inner shoulder of the annulus was dull and gray in color, suggesting that critical chip thickness was exceeded locally. No discernible change in surface condition could be observed between regions of positive, zero, and negative effective rake, when compared to the brittle-fractured shoulder region, suggesting that under appropriate cutting conditions, IRG 26 was tolerant of the small positive effective rake angles which can be an unavoidable result of STS/FTS process geometry.

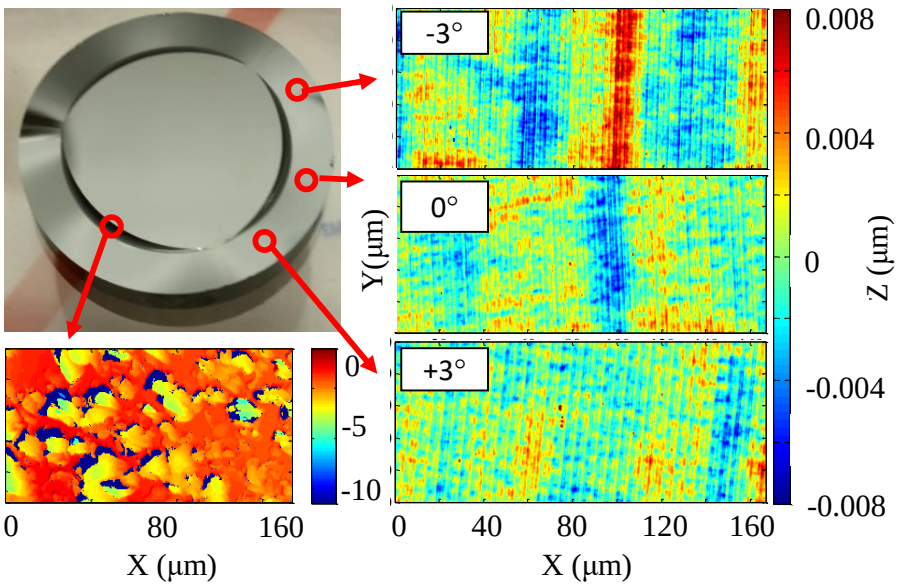

Figure 4.18: Clockwise from top-left: IRG 26 sine wave plate, 50X SWLI images at -3°, 0°, +3° rake, and brittle-fractured region of shoulder.

4.5 Orthogonal Flycutting

To investigate the cutting behavior of IRG 26 under interrupted cutting conditions, orthogonal flycutting experiments were performed using an implementation of the setup described in Section 3.8.2, which is shown in Figure 4.19(a). Initial experiments and results were summarized in [43] [60]. This setup duplicates the cutting geometry of orthogonal turning but in an interrupted cutting process. For consistency, and to enable a comparison between steady-state and interrupted cutting conditions, flycutting tests were performed using the same tool and specimen that were used for orthogonal turning experiments. After mounting on the machine spindle and initial balancing, the outer diameter of the flycutter was diamond turned to improve balance and provide a reference face for later reattachment. The vacuum chuck-dynamometer-tombstone system was assembled and aligned to the machine axes using a digital test indicator, resulting in a misalignment of less than 5 µm over 100 mm of travel. The face

of the vacuum chuck was machined in place and after mounting to the vacuum chuck, the specimen was machined in-situ using a 50 μm radius turning tool mounted in the flycutter, leaving only a thin rib of material standing above the bulk workpiece, as illustrated in Figure 4.19(b).

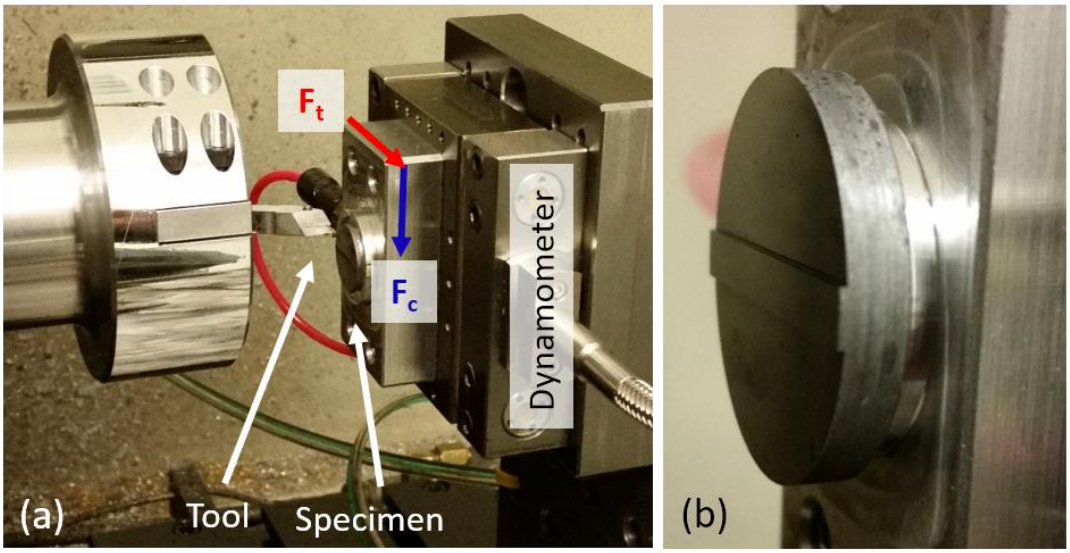

Figure 4.19: (a) Experimental arrangement for orthogonal flycutting (b) enlarged view of prepared specimen.

As described in [43], initial flycutting tests were performed using rib widths of 1, 2, and 4 mm, corresponding to tool-workpiece contact times of 0.5, 1.0, and 2.0 ms at a cutting speed of v_c = 2 m/s. Over the ϕ ranges bounding these cuts, as shown in Table 4.2, chip thickness variation due to chip thinning (see Eq. 2.8) was minimal and the rotation of the force coordinate frame with the cutter could be neglected, therefore cutting and thrust forces could be considered to be acting along a constant direction. In the configuration shown, cutting force was directed along the x-direction of the dynamometer and thrust force was directed along the y-direction. To enable a higher sampling rate (bounded by the DAQ's maximum aggregate rate), forces were not measured along the dynamometer's z-direction.

Table 4.2: Orthogonal flycutting specimen geometry

Rib Width (mm)	Contact Time (ms)	Start Angle, Φ_s	Exit Angle, Φ_e	Chip Thickness Variation
1.0	0.5	89.42	90.57	0.005 %
2.0	1.0	88.85	91.14	0.019 %
4.0	2.0	87.71	92.29	0.079 %

After machining of a given rib width on the specimen, the round-nosed tool was exchanged for the dead-sharp turning tool, which was oriented using the diamond turning machine's tool setting camera to present 0° side cutting edge angle to the workpiece. Cutting experiments were performed at v_c = 2 m/s (350 rpm), with w_c = 100 μm, and t_c varied from 200 nm to 2.0 μm. Three sets of experiments were performed in order of ascending chip thicknesses, and three in reverse order, for a total of six cutting experiments at each chip thickness value. Between each experiment, 250 revolutions of machining at t_c = 100 nm were performed to remove any accumulated cracking from the previous test. A total of 50 revolutions of cutting data were sampled at 500 kHz and subsequently post-processed in MATLAB®. Like the turning experiments, no cutting fluid was applied.

Unlike the turning process, which can be modeled as a time-invariant process [48], each pass of the flycutter through the workpiece was impact-like in nature, exciting many dynamic modes of the dynamometer and the tool. However, by applying an inverse filter [61], the original signal content could be recovered. For these initial flycutting experiments, in which only two channels of data were sampled, inverse filtering was performed in the frequency domain using the simplified approach described in Eq. 4.2. In this approach, which assumes negligible cross-coupling between the dynamometer axes, the corrected forces, $F_{x,corr}$ and $F_{y,corr}$ can be calculated from the

measured forces, F_x and F_y, and the direct frequency response functions (FRFs) of the dynamometer, which can be determined from impulse/tap testing of the dynamometer using an instrumented hammer as a stimulus. In the presented notation, H_{ik} represents the frequency-domain ratio of output along the k-direction to input along the i-direction, where j is the imaginary unit and ω is frequency in radians/sec. These direct FRFs were measured using TXF software and a PCB 086E80 small instrumented hammer. After inverse filtering, a 3rd order Butterworth lowpass filter was applied to eliminate frequency content outside the 10 kHz bandwidth of the tap-tests.

$$\begin{Bmatrix} F_{x,corr}(j\omega) \\ F_{y,corr}(j\omega) \end{Bmatrix} = \begin{bmatrix} H_{xx}(j\omega) & 0 \\ 0 & H_{yy}(j\omega) \end{bmatrix}^{-1} \begin{Bmatrix} F_x(j\omega) \\ F_y(j\omega) \end{Bmatrix} \quad \text{Eq. 4.2}$$

After inverse filtering, drift and offset were removed from the filtered signals, which are shown in Figure 4.20 for a 2 mm wide rib at chip thicknesses of 400 and 1600 nm. While the inverse filtering technique removes high-frequency noise and more completely isolates the true cutting forces, the forces are still partially corrupted by approximately 5 kHz noise. This corruption could be due to vibration of the cutting tool or by cross-coupling in the dynamometer axes which was not considered in Eq. 4.2, and therefore not adequately suppressed. Similar to the results obtained during orthogonal turning, at low chip thicknesses, the cutting and thrust forces were constant for all cutting revolutions. At higher chip thicknesses, the cuts began with force levels consistent with ductile-mode machining, indicating successful removal of previously-accumulated damage, then after a certain number of cutting revolutions, forces dropped sharply, indicative of the initiation of irreversible brittle-mode machining due to forward-propagated cracking.

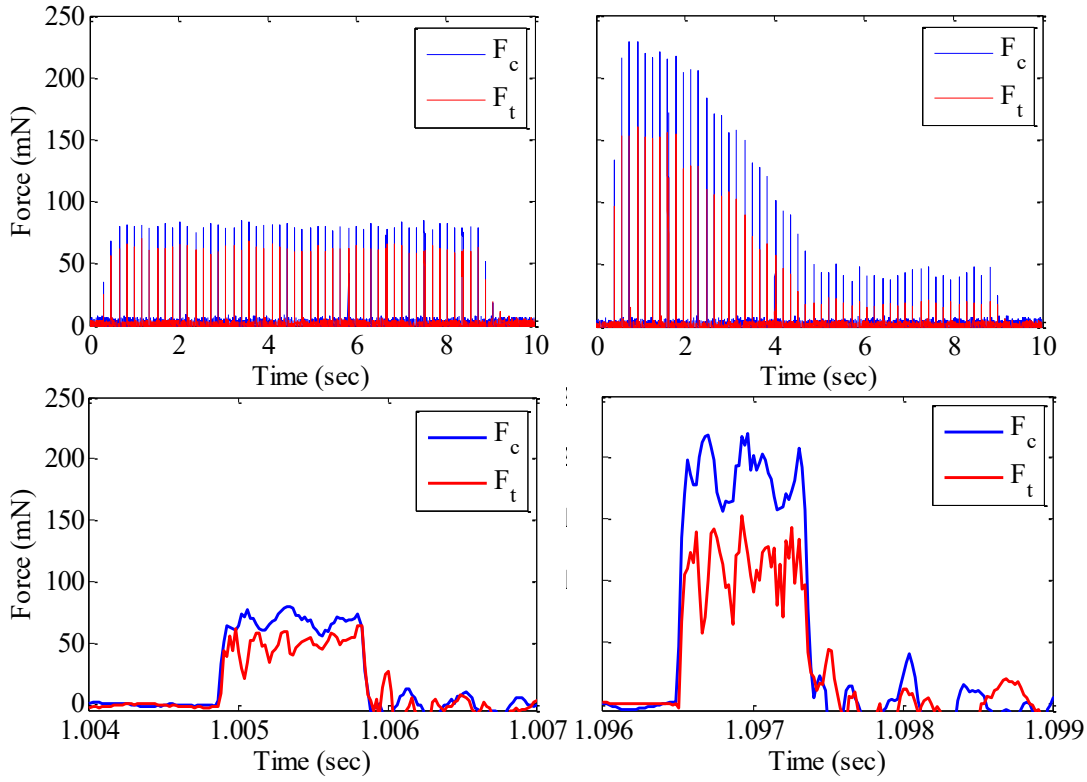

Figure 4.20: (top) Measured force signals and (bottom) selected regions of filtered data for IRG 26 orthogonal flycutting of 2 mm rib at t_c = (left) 400 nm and (right) 1600 nm.

For cuts which transitioned from ductile to brittle mode, the force dropoff rate increased with chip thickness, similar to turning (i.e. at higher values of chip thickness, fewer revolutions of cutting were required to propagate damage far enough ahead to initiate brittle mode machining.) For certain values of chip thickness near the transition zone, this dropoff rate was slow enough that only a few revolutions of steady state cutting occurred during the sampled duration.

After removing drift and offset, the force data was trimmed to include only the portion of each cut after a steady-state ductile or brittle machining mode had begun. Then, each pass of the tool through the workpiece was located using a MATLAB algorithm which detected sharp rising edges in the force signal, and a set number of samples (dependent upon the tool-workpiece interaction time) was retained after each

identified rising edge, thereby isolating only the portions of the data during which the tool was engaged in the workpiece. From this isolated data, average cutting and thrust forces were calculated, as shown in Figure 4.21 for the 2 mm rib.

A hysteresis-type effect similar to that reported in [47] was not observed. Agreement was evident between experiments performed in order of increasing chip thickness, indicated by triangles, and those done in decreasing order, indicated by circles, confirming that the followed protocol adequately removed any forward-propagated damage between experiments. Similar results were seen for rib widths of 1 mm and 4 mm, as presented in Figure 4.22. While each marker on Figure 4.21 represents a single experiment, each marker on Figure 4.22 represents an average of results from all cutting experiments at that particular chip thickness and rib width.

While no apparent change in cutting behavior could be observed with respect to rib width or contact time, an apparent transition from ductile-dominated to brittle-dominated cutting behavior occurred for all ribs between chip thicknesses of 800 and 1000 nm, slightly higher than exhibited during orthogonal turning experiments. However, closer examination of Figure 4.22 reveals that both cutting and thrust forces begin to deviate from linearity above a chip thickness of 600 nm, suggesting that this increased critical chip thickness may be an artifact of the experimental design, and that as a consequence of the force decay rate, that is an insufficient number of revolutions may have been sampled to truly observe steady-state cutting behavior at certain chip thicknesses.

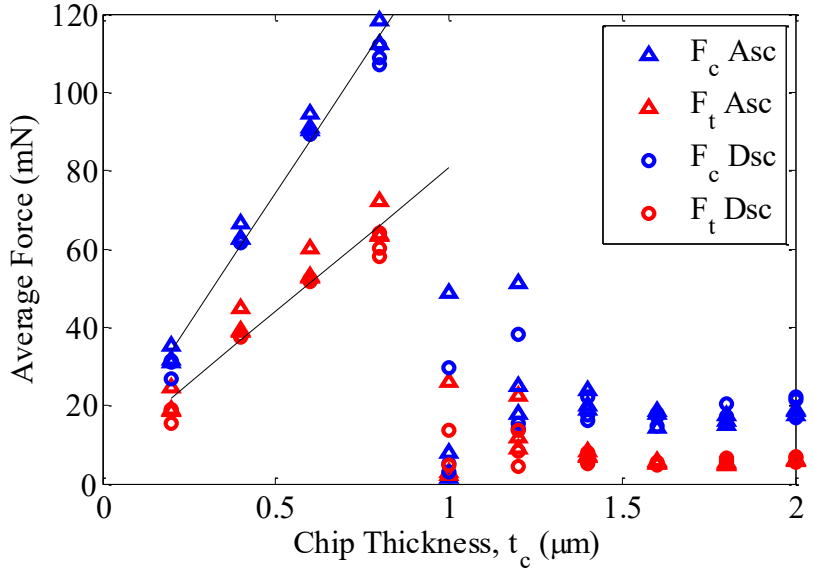

Figure 4.21: IRG 26 flycutting forces for 2 mm rib, 50 cutting revolutions sampled.

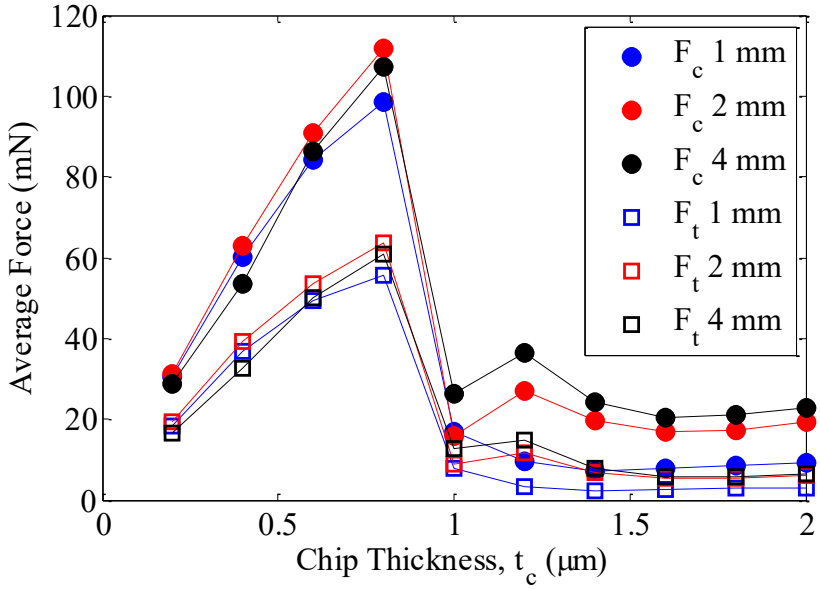

Figure 4.22: IRG 26 flycutting forces for multiple rib widths, 50 cutting revolutions sampled.

While the absence of any hysteresis effect suggests an appropriately-designed experimental procedure, the contact times produced during these initial flycutting experiments were relatively long compared to those (on order of 100 μs) encountered during typical diamond milling operations. To further investigate the cutting mechanics

during interrupted cutting, both rotational speed and rib width were varied in additional cutting experiments to produce much shorter contact times. Ribs having widths of 4 mm and 0.7 mm were cut at surface speeds varying from 1 to 8 m/s at a constant 100 μm depth of cut, with chip thickness again varied between 200 nm and 2 μm. A nominal 100 revolutions of cutting data were sampled at 500 kHz, but at chip thicknesses where low force decay rate to steady state occurred, up to 250 revolutions were sampled to adequately capture a sufficient portion of steady-state cutting behavior. Three sets of experiments were performed in order of ascending chip thickness for each rib width and cutting speed. To more completely eliminate signal corruption due to dynamometer effects, the more complete inverse filtering technique described in [62] and by Eq. 4.3 was utilized, which includes dynamometer axis cross-coupling effects.

$$\begin{Bmatrix} F_{x,corr}(j\omega) \\ F_{y,corr}(j\omega) \\ F_{z,corr}(j\omega) \end{Bmatrix} = \begin{bmatrix} H_{xx}(j\omega) & H_{xy}(j\omega) & H_{xz}(j\omega) \\ H_{yx}(j\omega) & H_{yy}(j\omega) & H_{yz}(j\omega) \\ H_{zx}(j\omega) & H_{zy}(j\omega) & H_{zz}(j\omega) \end{bmatrix}^{-1} \begin{Bmatrix} F_x(j\omega) \\ F_y(j\omega) \\ F_z(j\omega) \end{Bmatrix} \quad \text{Eq. 4.3}$$

The 9 direct- and cross-FRFs were determined again using impact testing with a higher bandwidth of 20 kHz, and are presented in Figure 4.23. As predicted earlier and shown in the figure, the cross-FRFs (plotted using blue lines) were much smaller in magnitude than the direct FRFs (plotted in black), but were not small enough to be neglected. After inverse filtering, a 3rd order Butterworth low pass filter with a cutoff frequency of 15 kHz was applied to suppress frequency content outside the bandwidth of the impact tests. Selected portions of raw and filtered data are presented in Figure 4.25 for 2 ms, 350 μs, and 175 μs contact times. As shown for the 2 ms case, the inverse filtering technique sufficiently removes signal corruption due to dynamometer effects.

When compared to the data presented in Figure 4.21, which was obtained under nearly identical cutting conditions but only processed using a simplified filtering scheme, it is clear that the residual signal distortions seen during the initial tests were due to axis cross-coupling effects in the dynamometer. It can further be concluded from this comparison that tool vibration was not a significant source of signal corruption.

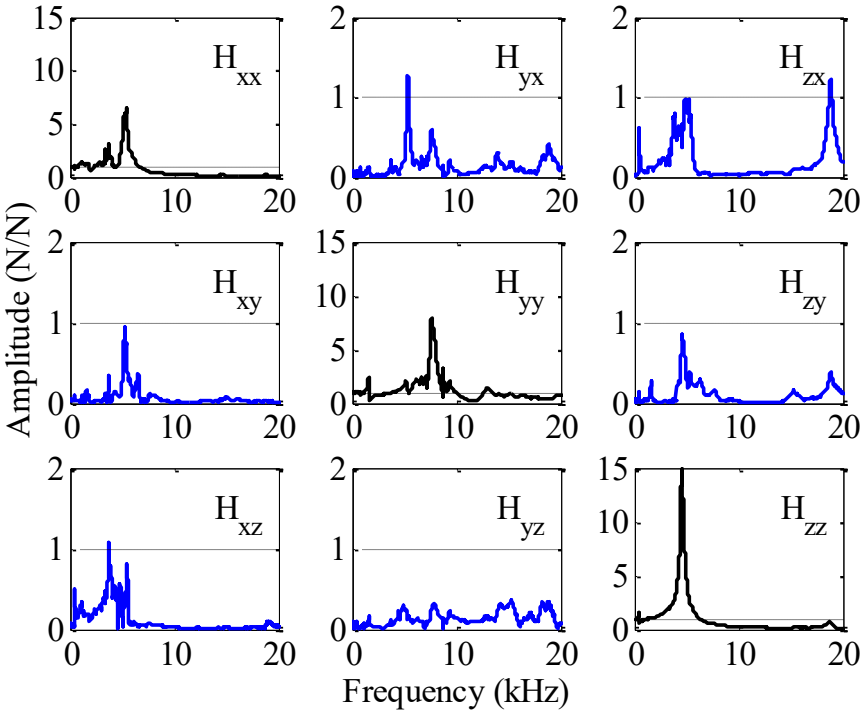

Figure 4.23: 3x3 FRF system FRF matrix for IRG 26 flycutting.

This improved filtering scheme more adequately recovers original signal content for millisecond-order timescales where the contact timescale was much longer than the characteristic times of the dynamometer natural frequencies. However, at shorter contact times on the microsecond order where the impact-like nature of the cut was on a timescale similar to the characteristic times of the dynamometer natural frequencies, it was impossible to fully remove the dynamometer effects without also removing some of

the true frequency content of the cut, as evidenced by the 350 μs and 175 μs contact time cases presented in Figure 4.24.

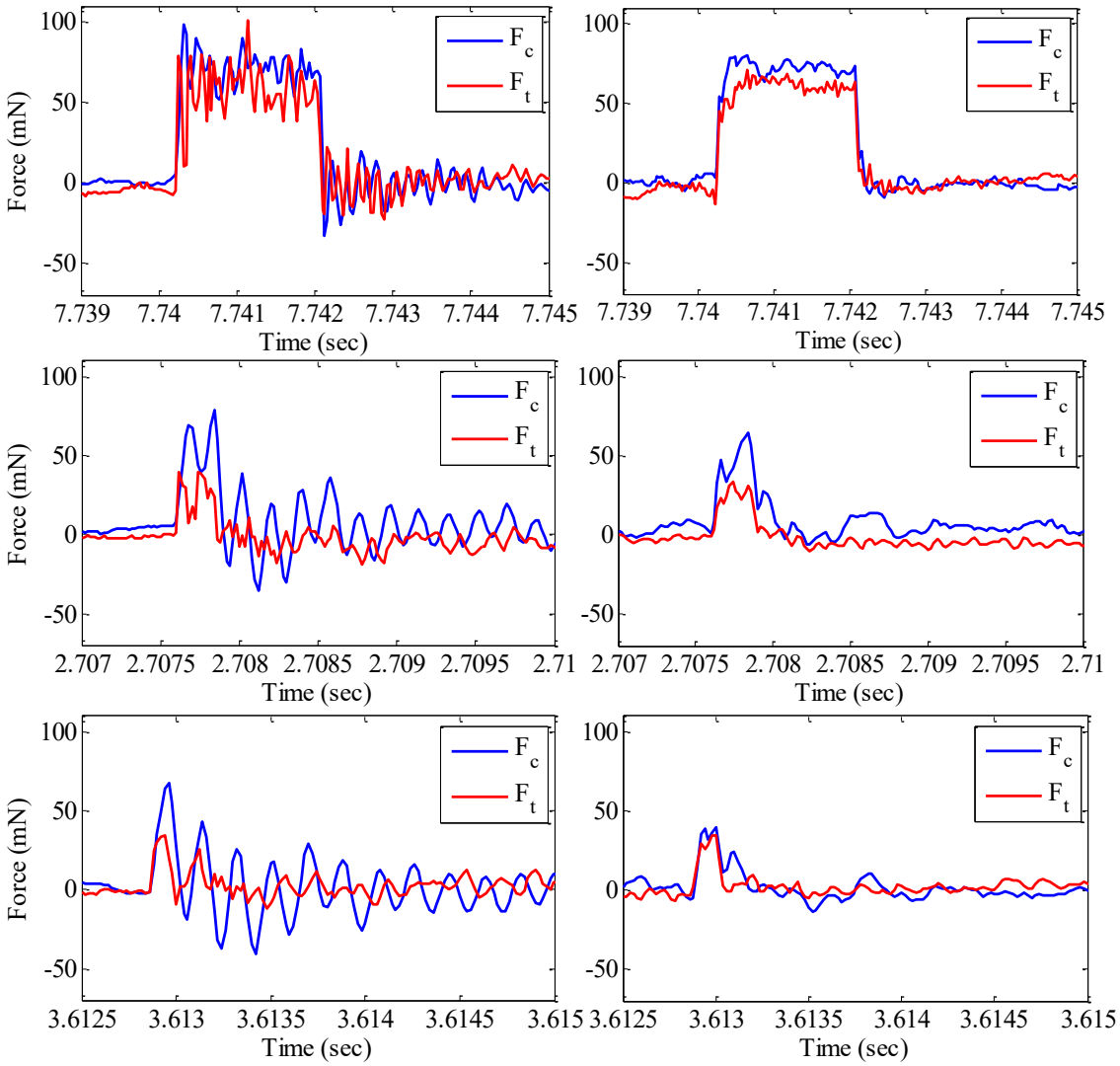

Figure 4.24: Raw (left) and filtered (right) forces during IRG 26 flycutting at 400 nm chip thickness along (top) 4 mm rib at 2 m/s (2 ms contact time), (center) 0.7 mm rib at 2 m/s (350 μs), (bottom) 0.7 mm rib at 4 m/s (175 μs). Only a single pass of the tool through the rib is shown for each.

Although the true frequency content was partially truncated for low-contact time cuts, resulting in reduced force levels, the impulse-like nature of the cutting process can still be observed in the filtered data, enabling a semi-quantitative analysis to continue even at these short contact times. As before, after the raw force signals were inverse

filtered, the data was trimmed to include only portions after which a steady-state cutting behavior began to occur. All of the selected cutting revolutions were aligned, and average cutting and thrust forces were calculated for the time during which the cutting tool was engaged with the workpiece rib. Average cutting and thrust forces are shown in Figure 4.25 for the 4 mm wide rib. Experiments were performed at 2 m/s and 4 m/s, corresponding to contact times of 2 ms and 1 ms. Additional tests were performed by flycutting the entire face of the 30 mm diameter specimen to produce relatively long contact times on the order of 20 ms.

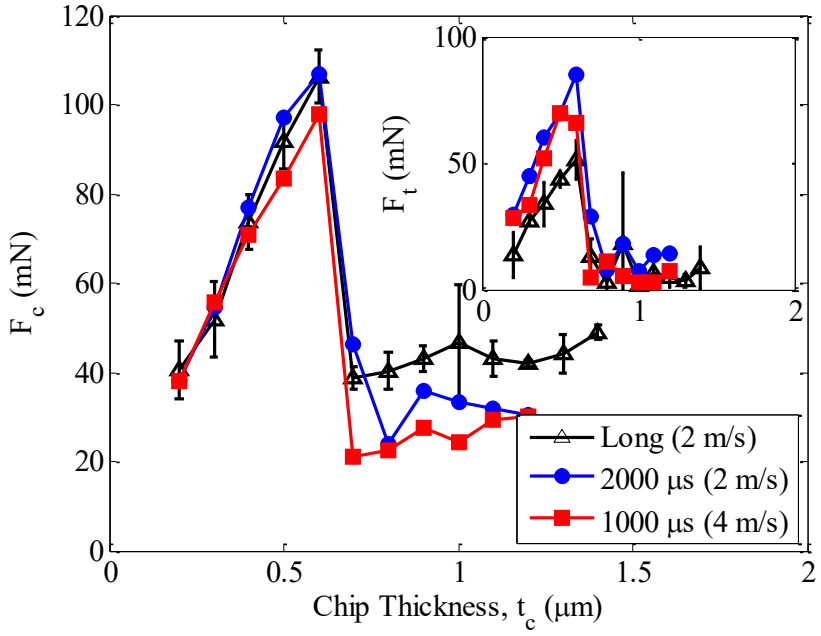

Figure 4.25: IRG 26 flycutting forces for 4 mm rib, 100 cutting revolutions sampled.

At these timescales, full removal of dynamometer effects does not result in appreciable signal corruption, enabling a direct comparison to previous experiments. Again, no change in critical chip thickness or force magnitude could be observed with respect to change in contact time. The critical chip thickness was once again observed to be approximately 600 nm, agreeing with the orthogonal turning data and confirming the

hypothesis that the supposed increase in critical chip thickness during initial flycutting tests was due to sampling an insufficient number of cutting revolutions, during which steady-state behavior was not fully obtained.

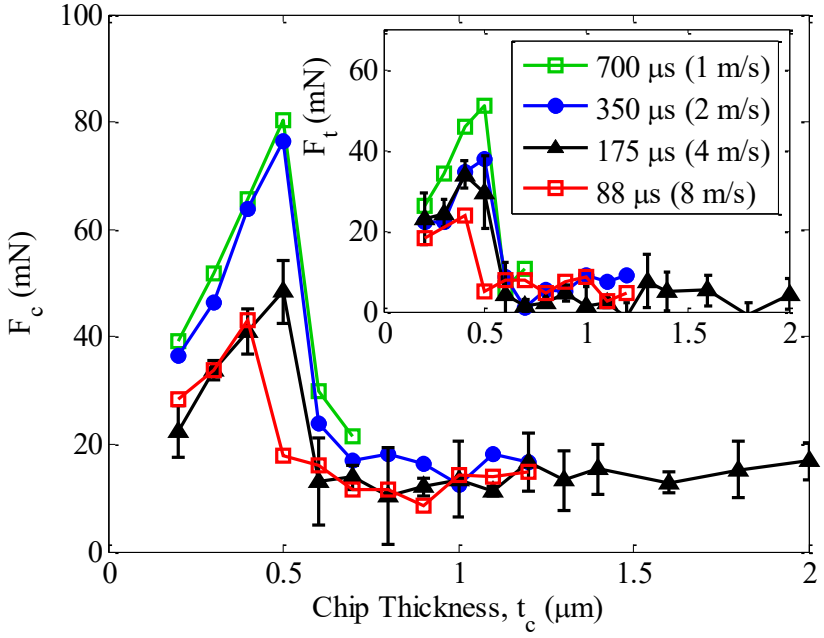

Figure 4.26: IRG 26 flycutting forces for 0.7 mm rib, 100 cutting revolutions sampled.

Average forces are shown in Figure 4.26 for the 0.7 mm wide rib. Experiments were conducted on this rib at cutting velocities of 1, 2, 4, and 8 m/s, corresponding to much shorter contact times of 700, 350, 175, and 88 μs, on the order of those encountered during typical diamond milling operations. Although the force levels are partially corrupted and reduced due to removal of dynamometer dynamic effects, ductile-dominated and brittle-dominated cutting regimes remain clearly observable. Unlike the force magnitudes, which cannot be related to those from longer-duration processes due to dynamic effects, the critical chip thicknesses can be directly compared. At contact times of 700, 350, and 175 μs, a critical chip thickness between 500 and 600 nm can be observed, consistent with previous results. At a contact time of 88 μs, a slightly lower

critical chip thickness between 400 and 500 nm was apparent. However, it is known from the results of Section 4.2.2 presented in Figure 4.8 that the critical chip thickness decreases slightly at surface speeds exceeding 4 m/s. Further, due to inherent imbalance of the flycutter, rotation at the cutting speed of 8 m/s, corresponding to a spindle speed of 1400 rpm, produces a rather large rotational imbalance and tool vibration. This causes the instantaneous chip thickness to vary and could cause an earlier onset of fracture-dominated cutting. Therefore, it can be concluded from these experiments that for IRG 26, cutting mechanics do not change significantly in response to tool-workpiece interaction time, even on timescales less than 100 μs.

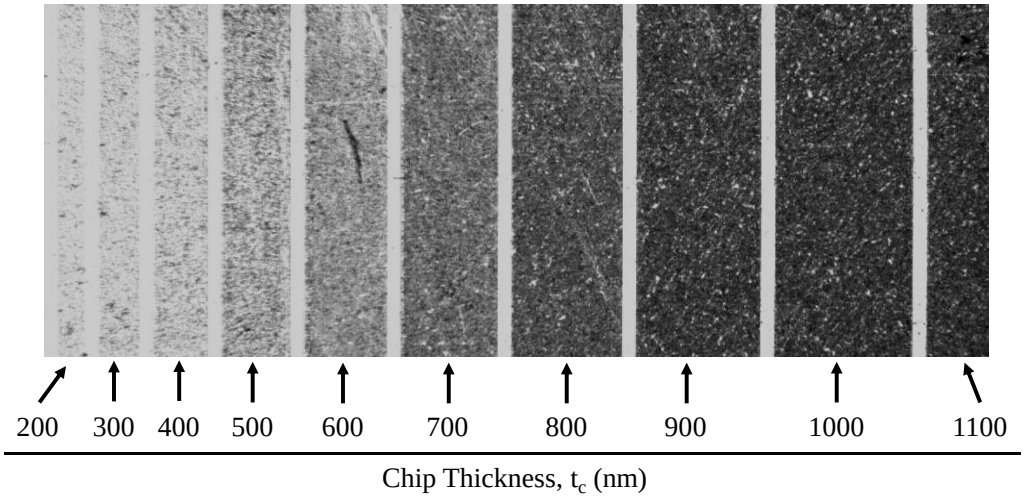

Figure 4.27: Digital microscope image of floor of flycut rib specimen, image is approximately 0.25 mm tall.

A digital microscope image of a portion of the floor of a cut rib specimen, showing ten cutting experiments, is shown in Figure 4.27. The highly reflective vertical bands between the images are the result of cleanup machining at 100 nm/rev performed between experiments. Because each cutting experiment had a fixed number of revolutions, the resulting bands are wider as chip thickness increases. Although surface finish obtained with a sharp tool as used in orthogonal turning and flycutting experiments

was much rougher than could be produced by flycutting with a round-nosed tool, a clear increase in apparent cracking and surface damage can be observed with increasing chip thickness. This is similar to the trends evidenced in Section 4.4.

4.6 Slot Milling

Low-speed slot-milling experiments were conducted on the same workpiece used for orthogonal turning and flycutting experiments using the experimental setup described in Section 3.8.3 and pictured in Figure 4.28. Tests were performed using both square and round-nosed milling tools. For both cases, spindle speed was maintained at 1000 rpm and a light air blast with no lubrication was applied near the cutting zone to assist with chip evacuation. For each experiment, 50 revolutions of cutting were sampled at 100 kHz and post-processed using inverse filtering.

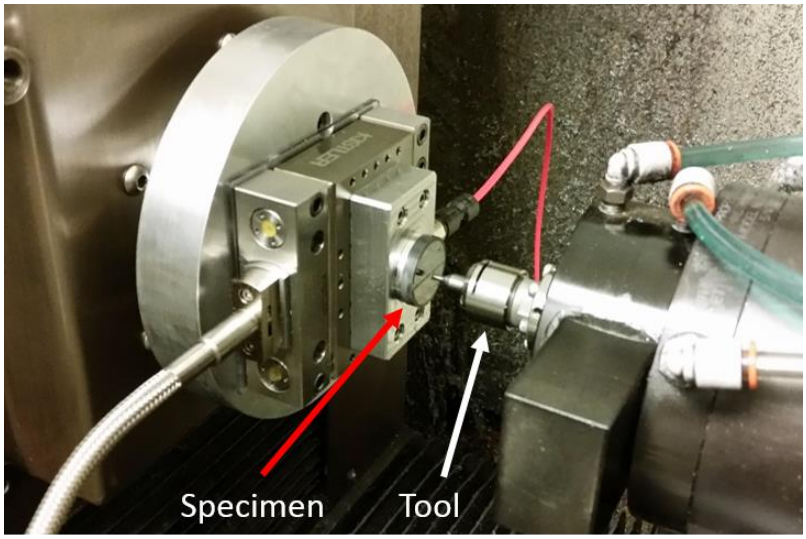

Figure 4.28: IRG 26 slot milling experimental setup.

In this experimental setup, the dynamometer was mounted to the main spindle of the diamond turning machine, which was locked in position in C-axis mode. The dynamometer was isolated electrically by use of a thin polycarbonate shim beneath the C-axis mount. The system FRF matrix for this configuration is shown in Figure 4.29.

Again, the cross-FRFs are of much lower magnitude than the direct FRFs, but are not sufficiently low to be neglected, requiring use of the full 3x3 inverse filtering approach from Eq. 4.3. As in the flycutting experiments, a 15 kHz low pass 3rd order Butterworth filter was applied to the filtered data to truncate frequency content outside the bandwidth of the tap tests used for system dynamics identification.

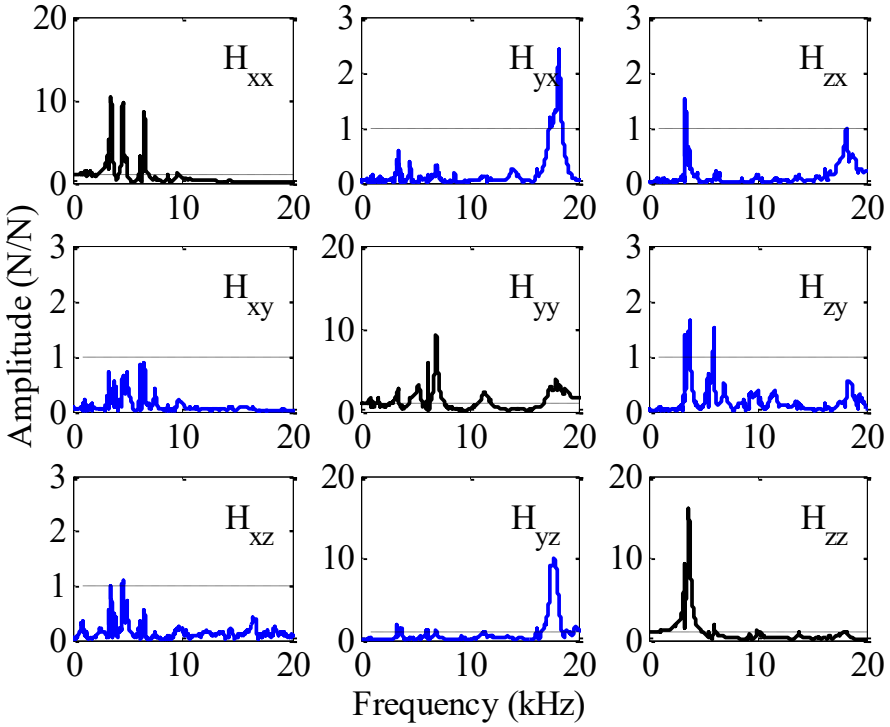

Figure 4.29: 3x3 FRF system matrix for IRG 26 milling experiments.

Slot-milling experiments were performed at a constant axial depth of cut, d_a, of 0.2 mm, and feed per revolution, f_t, of 400, 800, and 1300 nm, using the specially-ordered square SCD endmill described in Section 3.7. At each feed rate, 25 revolutions of cutting data were isolated and aligned, from which a mean force profile for a single revolution of cutting was generated. These mean force profiles were then compared to force predictions made using orthogonal turning data following the approach of Section 2.3.1, as presented in Figure 4.30.

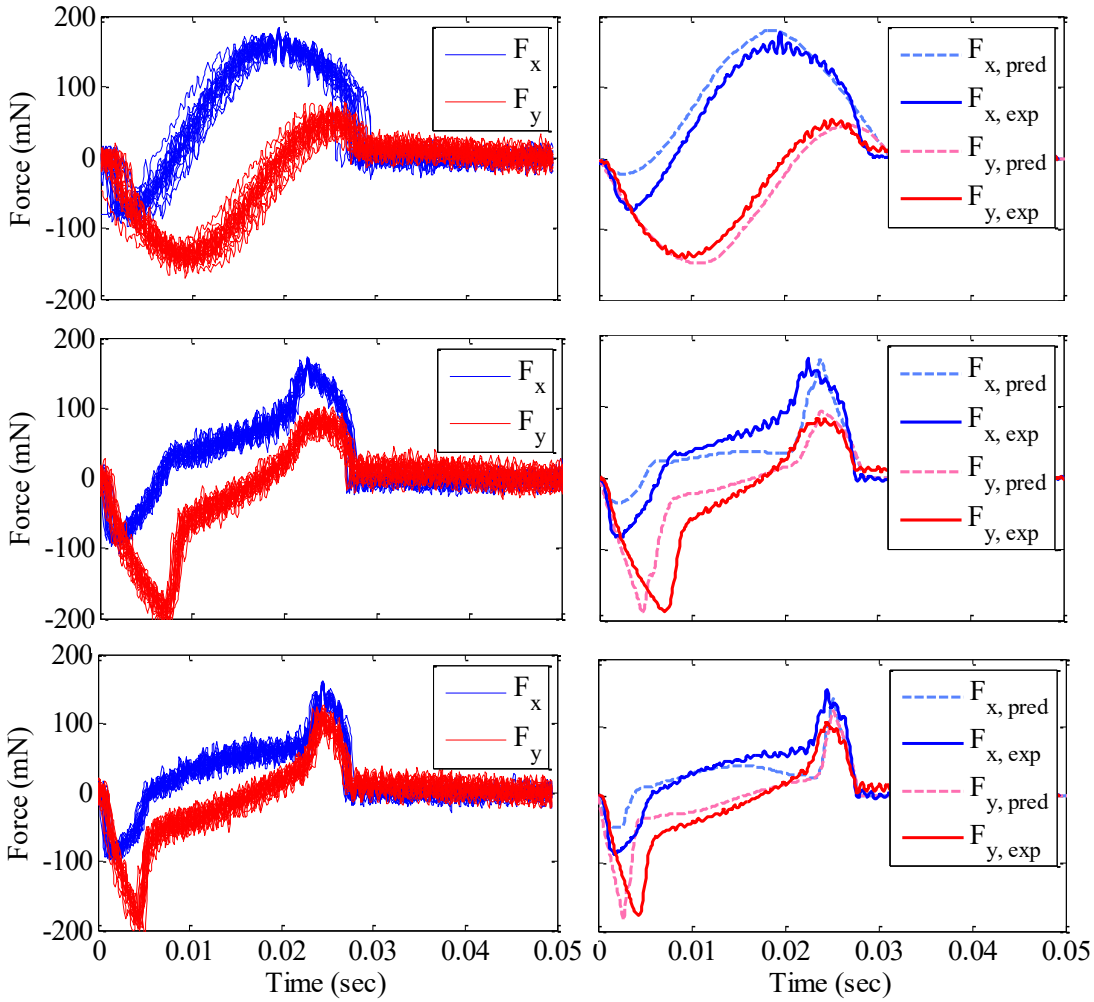

Figure 4.30: (left) 25 filtered and aligned cutting revolutions and (right) mean revolution and predicted force values for IRG 26 orthogonal slot milling at feed per revolution of (top) 400 nm, (center) 800 nm), and (bottom) 1300 nm.

At a feed rate of 400 nm per revolution, the instantaneous chip thickness never exceeded the now known critical chip thickness of 600 nm, thus the force profile obtained agreed very well with predictions and was qualitatively similar to that observed when machining a ductile metal. At higher feed rates, the critical chip thickness is exceeded over certain intervals of ϕ, resulting in reduced force magnitudes during these portions of the cut. Inspection of the figure reveals acceptable agreement between experimental results, shown by solid lines, and predicted values, shown by broken lines,

for all feed rates, as well as acceptable accuracy in predicting the onset of brittle fracture during the cut, confirming the validity of the cutting force model and prediction method. Small discrepancies between the predicted and actual values may be due to spindle speed uncertainty and sources such as tool runout which are not considered in the simplified cutting force model.

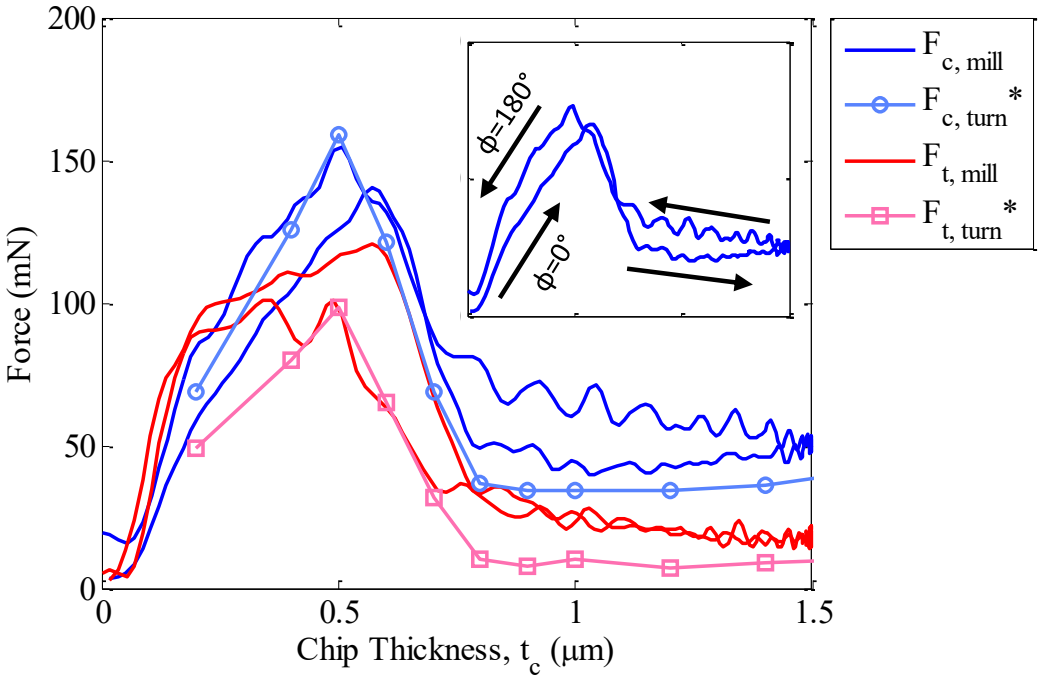

Figure 4.31: IRG 26 orthogonal slot milling, force variation with chip thickness with scaled orthogonal turning data for reference.

Discrete experiments allow comparison between predicted and experimental force magnitudes during orthogonal slot milling. However, by virtue of the process geometry, such a cutting process also provides a dense sampling of force variation with chip thickness; theoretically all chip thicknesses can be measured. Additional slotting experiments were performed at a feed rate of 1500 nm per revolution. After post-processing, the measured forces on the dynamometer reference frame were decomposed into instantaneous cutting and thrust components, and are presented as a function of chip

thickness in Figure 4.31. The previously-obtained orthogonal turning data was scaled by a factor of 2 to account for the change in depth of cut between experiments, and is shown for comparison. Forces from both milling and turning experiments show excellent agreement. While cleanup machining between discretized orthogonal turning experiments eliminated hysteresis effects, propagation of cracks ahead of the tool is unavoidable in a milling process. As a result, a slight hysteresis effect is evident and clarified in the figure inset, in which the critical chip thickness is approximately 50 nm lower when chip thickness is decreasing. The magnitude and sense of this hysteresis effect are consistent with that reported in [47].

CHAPTER 5: DIAMOND MACHINING OF GERMANIUM

5.1 Introduction

The cutting mechanics of single crystal germanium have been studied for many years and are documented in fundamental works such as [13] [17] [40]. While amorphous materials typically do not exhibit appreciable inhomogeneity within a single workpiece, it is well-known than when machining crystalline materials such as germanium, the cutting mechanics of the material are more conducive to fracture-free machining when cutting is directed along certain planar orientations of the crystal. As detailed in [13], when a wafer of germanium with the <1,1,1> crystal orientation aligned along the spindle axis is face-turned, the rotation of the specimen causes the tool to cut along all possible planar orientations, depending upon the instantaneous orientation of the workpiece on the machine spindle, and under certain conditions this can result in a tri-lobed fracture pattern indicating the most favorable and least favorable planar orientations for cutting..

A comprehensive study of orthogonal machining of <1,1,1> germanium is presented in [47]. In that work, orthogonal turning experiments were performed following a procedure similar to that described in Section 4.2 using a -25° rake angle SCD tool. Unlike the behavior observed when machining chalcogenide glasses, cutting force was found to monotonically increase with chip thickness for germanium, never exhibiting an abrupt decrease or change. However, cutting coefficients exhibited a sharp

decrease above chip thicknesses of approximately 100 nm, again suggesting a transition from a ductile-dominated to a brittle-dominated cutting mechanism. While process forces were found to generally be invariant with cutting speed when machining chalcogenide glass, they were shown to be highly sensitive to cutting speed during germanium cutting with the largest changes occurring below a cutting speed of 3 m/s.. Another notable finding of this work was that the tri-lobe pattern caused by the crystal planar orientation reverses by 180° when cutting direction is reversed. Therefore, for example, if a planing operation is performed along one of the most preferable cutting directions, simply rotating the workpiece by 180° will cause subsequent cutting to occur along one of the least preferable directions.

In this chapter, the results of which are also summarized in [63], presents round-nosed turning experiments performed on single crystal <1,1,1> germanium specimens, and the results agree well with predictions based upon orthogonal turning data from [47]. Further, to enable an initial comparison between steady and interrupted cutting processes, round-nosed flycutting experiments were performed under identical cutting conditions along the least favorable cutting direction, and were again found to be in agreement with predictions from orthogonal turning data. Surface metrology of machined specimens showed significant surface deterioration at feed rates above 2 μm per revolution but otherwise showed little difference between flycut specimens and turned specimens measured along both the most and least preferable cutting directions. Further analysis of the specimens by Raman spectroscopy indicated a monotonic increase in both residual compressive stress and subsurface damage with feed rate, with similar characteristics observed on both turned and flycut specimens. Residual compressive stresses were lower

in magnitude when measured along the least preferred planar orientation than when measured along the most preferred orientation. It is surmised that this is because fracture will relieve residual stresses while ductile deformation will cause a deformed and hence strained surface layer. Further experiments with shorter tool-workpiece interaction times would be a logical extension of this initial work and would aid with gaining a fundamental understanding of the machining behavior at different timescales.

5.2 Round-nosed Turning

Round-nosed face turning experiments were performed on 25 mm diameter, 1 mm thick <1,1,1> undoped germanium witness specimens from Novotech. The tool has a 1.0 mm radius, and a -25° rake angle. As described in Section 4.4, the tool was mounted atop the Kistler 9256C1 miniature cutting force dynamometer, and the specimen was held with a custom-designed vacuum chuck. Cutting speed was held constant at 4 m/s (corresponding to 3000 rpm), and a 5 μm depth of cut was maintained. During these experiments, force data was sampled at 200 kHz. The tool was commanded to feed into the workpiece for 75 revolutions at each feed rate which ranged from 0.5 μm/rev to 9.0 μm/rev. Three sets of 'step' tests were performed, resulting in force signals such as shown in Figure 5.1. A crossover of F_v and F_a is evident at a feed rate between 1 μm/rev and 2 μm/rev, similar to that reported in [47], indicating a more rubbing-dominated cutting behavior at low feed rates, possibly due to the edge radius of the cutting tool. Closer examination of the force signals, as shown in the inset, show a force oscillation at a frequency of three cycles per revolution of the part, due to the tri-lobed symmetry described in [13]. The magnitude of the oscillations increases with feed rate, confirming a ductile-dominated material response for certain planar orientations. At all feed rates. F_p

was much lower than the other force components. While systematic changes are visible, the component was low and was significantly affected by system noise. A low-pass 3rd order Butterworth filter with cutoff frequency of 500 Hz was applied to all raw data.

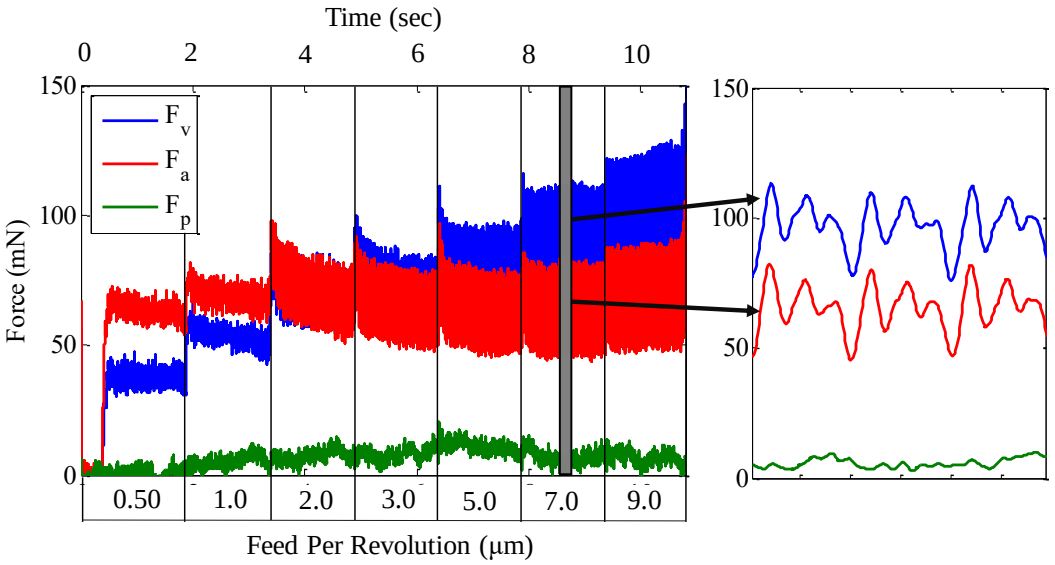

Figure 5.1: Forces during round-nosed turning of germanium.

This oscillation in forces during turning as a function of planar orientation implies that process force coefficients also vary with orientation. However, comparison of mean forces under the same conditions such as those in [47] is reasonable. . Figure 5.2 shows average process forces for the round-nosed turning experiments presented in Figure 5.1, as well as predicted force values from the orthogonal turning data of [47] and Eq. 2.3. As expected, no sharp or abrupt drop in process forces is evident, however the rate of increase (or slope) of the individual force components decreases considerably between feed rates of 0.5 and 1.0 μm/rev, confirming as shown in [47] that some transition in cutting behavior occurs around a chip thickness of 100 nm.

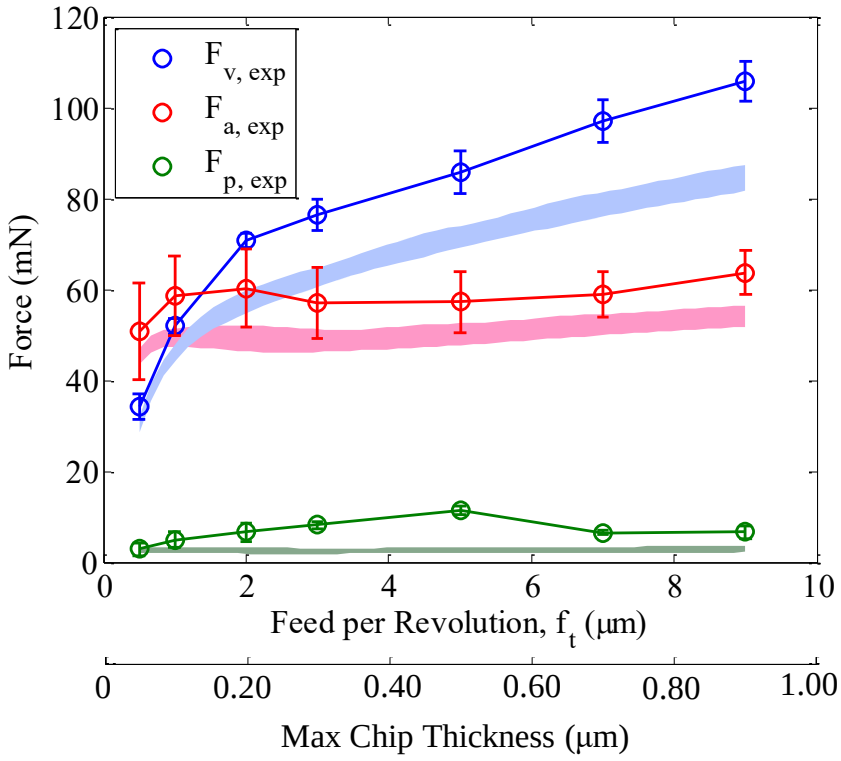

Figure 5.2: Average and predicted forces for round-nosed turning of germanium. Solid areas indicate predictions and the width of solid areas indicates uncertainties from one standard deviation of cutting force coefficients.

Predicted force bands are one standard deviation wide. The experimental and predicted force behaviors agree well, both exhibiting a crossover of force components between feed rates of 1 and 2 μm/rev, although the predicted values of F_v and F_a are somewhat lower than the experimental values. It is believed that this discrepancy is because the process coefficients used for force prediction are tool-dependent. The disagreement between predicted and experimental values of F_p is likely due to measurement noise. Although predicted force magnitudes are lower than experimental values, the overall agreement in form between the data confirms the viability of the cutting force model developed in Section 2.2.3 more convincingly than done by the round-nosed turning of IRG 26.

5.3 Round-nosed Flycutting

To enable an initial comparison of cutting mechanics during steady and interrupted cutting processes, round-nosed flycutting experiments were performed with the same tool used for the previously-described turning tests. While variation in cutting mechanics due to planar orientation is unavoidable during turning operations, unidirectional processes such as flycutting and planing encounter only a single orientation. Therefore, to ensure validity of comparison between experiments, a consistent planar orientation must be maintained at all times. Before preparation of individual specimens, six 25 mm diameter wafers were face-machined with a 5 μm depth of cut at a 3 μm/rev feed rate to produce the tri-lobed pattern necessary for identifying planar directions. All six wafers were mounted to an aluminum plate using low-temperature Crystalbond 505 wax adhesive. Three 8 mm diameter individual specimens were diced from each wafer with an orientation flat along one of the most preferable directions using a square SCD endmill, then removed and cleaned. This specimen preparation process is summarized in Figure 5.3.

Flycutting experiments were performed using a setup adapted from the one described in Section 4.5. A custom vacuum chuck was mounted to a dynamometer. The chuck was designed to hold the individual germanium specimens. When the flycutter rotated so that the tool was in its lowermost position, the cutting velocity was directed along the orientation flat on the side of the specimen, as shown in Figure 5.4. With respect to Figure 5.4, the flycutter was fed from top to bottom and thus the side of the specimen with the orientation flat was machined first.

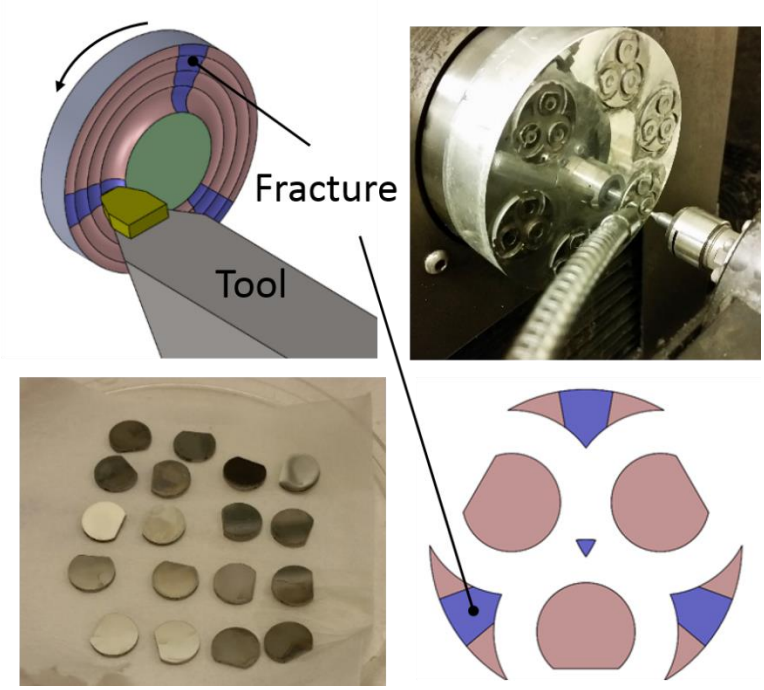

Figure 5.3: Clockwise from top left: round nosed turning to identify planar orientation of wafers, dicing of specimens using a milling cutter, planar orientation of three specimens on a single waver, diced specimens used for experiments.

In this configuration, while cutting velocity is still directed along the orientation flat, it is in a direction opposite from that of the turning test used to first identify planar orientation. Therefore, cutting during these flycutting experiments was occurring along the least preferable direction or most limiting cutting direction. Thus the machining experiments allow for the investigation of the most limiting cutting parameters translating into practical machining conditions for which fracture will not occur at any tool orientation.

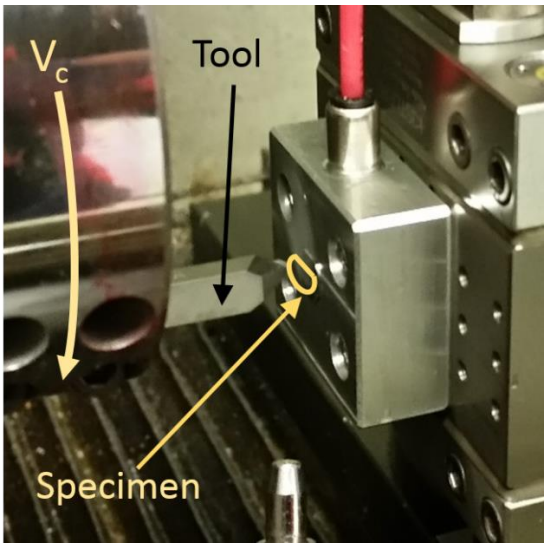

Figure 5.4: Specimen orientation during round-nosed flycutting of germanium.

Experiments were performed using identical cutting conditions as used for turning tests. The cutting speed was maintained at 4 m/s (corresponding to 700 rpm) and depth of cut was held constant at 5 μm. The entire face of an individual specimen was machined at a constant feed rate. The feedrates for generating these specimens where varied from 0.5 μm/rev to 9 μm/rev. Three sets of force data, each 10 seconds in duration were sampled at 200 kHz during the facing of each specimen. The data was post-processed using a 2.5 kHz low pass 3rd order Butterworth filter. Portions of the data during which the cutting tool was engaged in the workpiece were located using a MATLAB® algorithm which detected sharp rising edges in the force signals, then a set number of samples was after each identified rising edge were isolated. This algorithm resulted in force signals which were acceptably aligned and required no further post-processing. Average forces were then calculated from the aligned data. Many aligned portions of cutting data are shown in Figure 5.5 at example feed rates of 1 μm/rev and 9 μm/rev. These demonstrate the repeatability of the magnitude and oscillatory character of the force signal during each engagement of the flycutter, as well as the accuracy of the

alignment procedure. They also show the expected crossover between F_v and F_a between these two feedrates: in the right figure $F_a > F_v$ whereas in the left figure $F_v > F_a$.

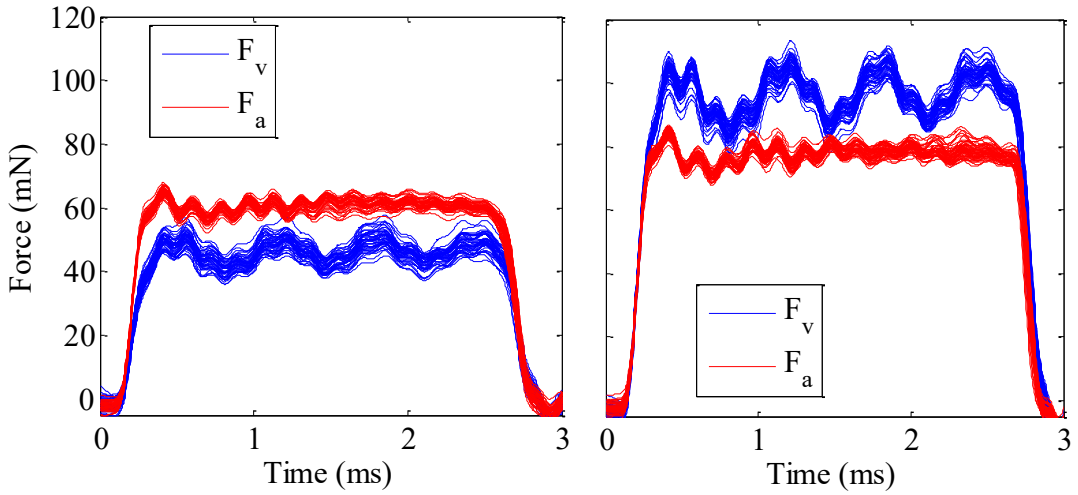

Figure 5.5: Aligned cutting force profiles for many revolutions of round-nosed flycutting of germanium at (left) 1 µm/rev, (right) 9 µm/rev.

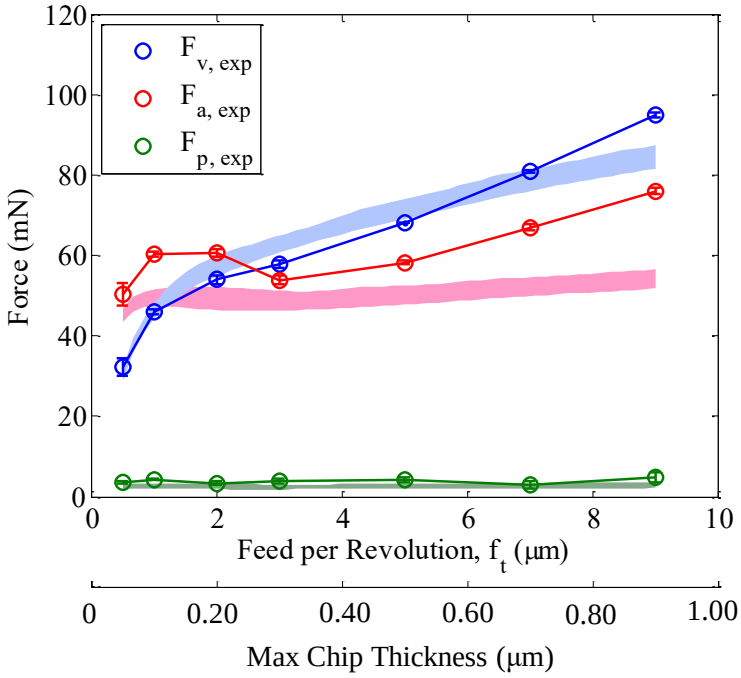

Figure 5.6: Average and predicted forces for round-nosed flycutting of germanium.

Recalling that the flycutting geometry, during cutting, is identical to the turning geometry described earlier, predictions could be made by the same numerical integration

procedure – mechanistic modeling – used for turning. Figure 5.6 shows average process forces from flycutting compared to the previously predicted values (Figure 5.2). The general form of the predicted and experimental behavior again agreed. Further, the experimental force magnitudes shown are less than those shown in Figure 5.2, confirming that during these experiments, cutting occurred along one of the least preferable (and most brittle-dominated) directions at higher feed rates. Again, a change in slope of the individual force components was observed between feed rates of 0.5 and 1.0 μm/rev, suggesting a more brittle-dominated machining condition at higher feed rates.

5.4 Metrology of Machined Specimens

Surface finish and integrity of the germanium specimens was assessed using SWLI. Three surface measurements were performed on each individual flycut specimen. Three further measurements were performed on the turned disc at locations corresponding to each feed rate along both the best and least preferred cutting directions. Areal roughness, Sa, is shown in Figure 5.7 for all specimens as a function of feed rate, There is a sharp increase in roughness at feed rates above 2 μm/rev. Closer examination of individual micrographs reveals an increase in pitting and cracking as feed rate increases. Surface integrity is also characterized by the new metric RI_{80} in Figure 5.8, indicating similar trends above feed rates of 2 μm/rev. Comparing Figure 5.7 and Figure 5.8, it is evident that the RI_{80} seems to be a more sensitive indicator of surface damage than Sa in this case.

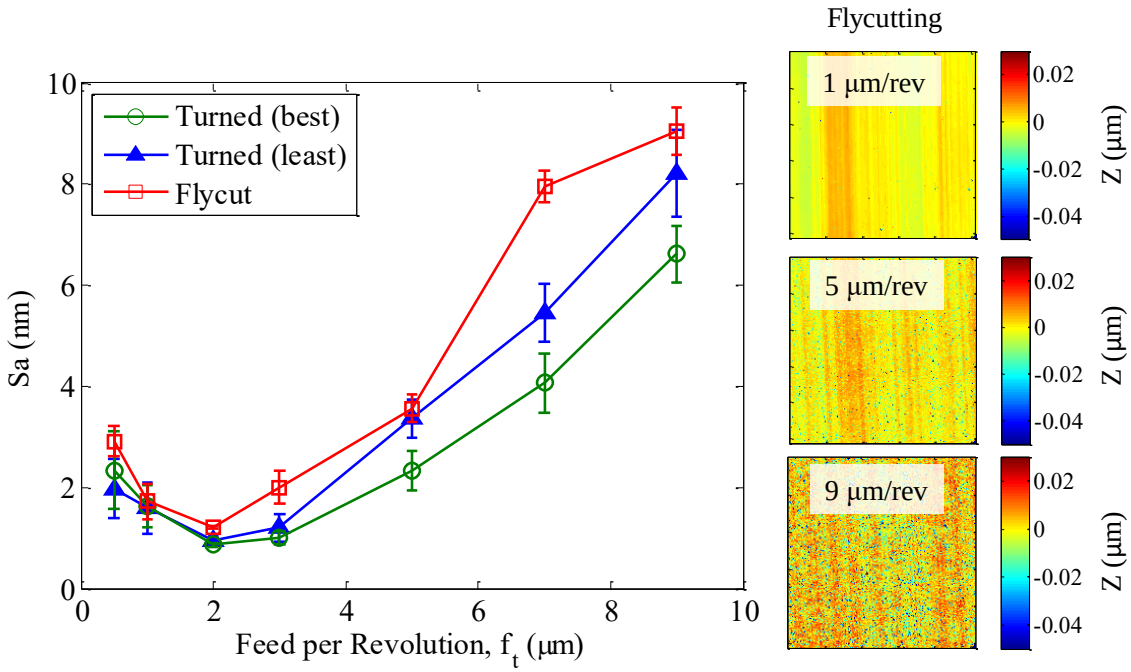

Figure 5.7: (left) Sa of round-nosed machined germanium, (right) SWLI micrographs of flycut specimens at 1, 5, and 9 µm/rev feed. FOV is a 408 µm square.

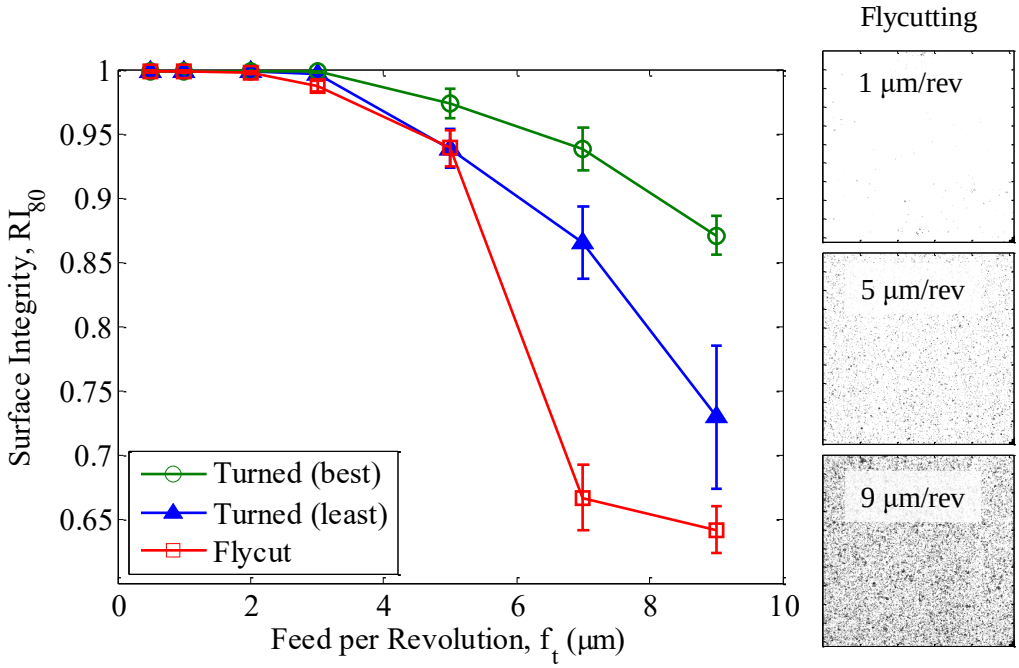

Figure 5.8: (left) RI_{80} of round-nosed machined germanium, (right) SWLI intensity maps of flycut specimens at 1, 5, and 9 µm/rev feed. FOV is a 408 µm square.

Both metrics show the flycut specimen surfaces indicate that the flycut specimens have a decreased surface quality when compared to the turned specimens at the same parameters. This becomes more pronounced at feed rates above 2 μm/rev. Due to geometrical restrictions, the extension of the tool was greater in flycutting than in turning. As a result, flycutting operations were more prone to tool vibration. Vibrations can clearly be seen in Figure 5.5 for both cases and are particularly pronounced for the 9 μm/rev case. This is likely responsible for this surface degradation in flycutting. Furthering this notion, below 2 μm/rev, the vibration is less pronounced and the surface integrity of turned and flycut specimens is nearly identical within the experimental uncertainty. While it was hypothesized that interrupted cutting operations are sometimes more conducive to ductile-dominated machining, it is possible that no change in behavior was evident because the tool-workpiece interaction times produced by this configuration were much longer, on order of 25 ms, than those expected during typical milling operations.

It is well-known that surface finish and condition are not reliable indicators of subsurface characteristics, which become increasingly important for higher-power applications. Raman spectroscopy of the flycut specimens was performed as detailed in [63], and this analysis was extended to the turned specimen as well. Raman peak shifts and the FWHM of measured Raman peaks are shown in Figure 5.9 for the flycut specimen and for scans of the turned specimen along the most favorable and least favorable directions (i.e. along undamaged and damaged lobes.) At each examination location, a 50 x 50 μm, 100 x 100 pixel square scan area was analyzed, resulting in a total of 22500 acquired spectra. Examination of spectra from an as-received germanium wafer

before machining indicated a Raman peak with wavenumber of 300.5 cm^{-1}. It was observed that as feed per revolution increased, the Raman peak was shifted to a higher wavenumber, indicating a change to a smaller crystalline lattice spacing due to residual compressive stress.

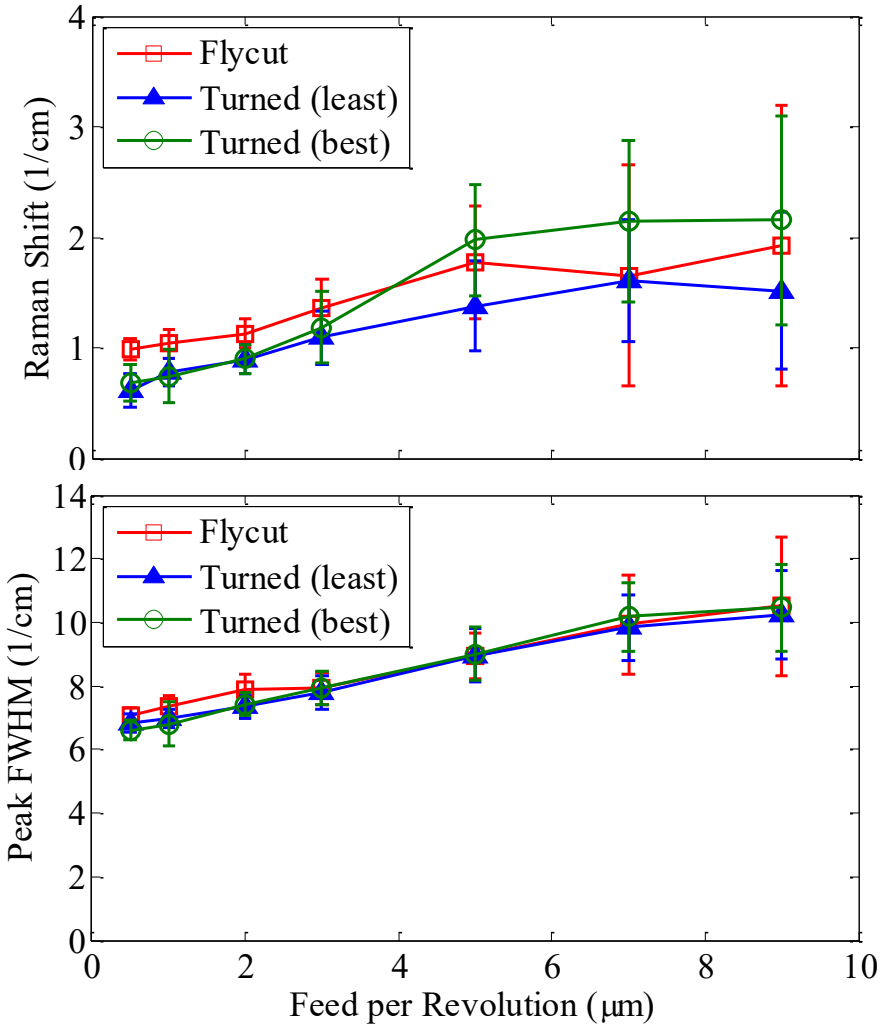

Figure 5.9: Measured Raman wavenumber shift (top) and shifted peak FWHM (bottom) of machined germanium specimens.

Below feed rates of 5 μm per revolution, the flycut specimens had higher compressive stress than the turned specimen, which exhibited similar Raman peak shift (Figure 5.9, top). However, above 5 μm, the mean residual stresses in the flycut

specimen were between those of the two orientations measured on the turned specimen. Further, the turned specimen had more compressive stress along the most preferred direction (undamaged lobe) than along the least preferred direction. It is speculated that less residual compressive stress would be generated during fracture dominated machining because the fractures relieve the stresses leaving undamaged crystal, whereas ductile deformation leaves a deformed surface layer with residual lattice strain. For all specimens, the peak FWHM was found to increase monotonically with feed rate, indicating a corresponding increase in subsurface damage and lattice disorder, with similar FWHM values observed regardless of specimen machining method.

CHAPTER 6: SLOW TOOL SERVO PROCESS DEVELOPMENT

6.1 Introduction

While axisymmetric parts are easily produced by conventional diamond turning and nearly arbitrary freeform surfaces can be generated by ultraprecision diamond milling, slow- or fast-tool servo machining is often the most efficient way to produce freeform surfaces with sufficiently mild surface departures. A detailed study of the process dynamics and control loop of the Moore Nanotechnology 350UPL is presented in [64] [65], and is also applicable to the 350FG (see Section 3.2) used in this dissertation. Although fast-tool servo systems which mount on top of existing machine axes are available and can operate at bandwidths, often above 1 kHz, such systems typically are stroke-limited to less than 1 mm and are often cost-prohibitive. The performance of an STS configuration is limited only by the bandwidth of the machine control loop, making STS more robust than FTS and more economical as well, as it requires no additional equipment to be purchased beyond that available on a now typical ultraprecision machine. Given the stiffness and precision of contemporary ultraprecision machines, assuming appropriate thermal control, resulting workpiece errors are dominated by slope-dependent tool errors due to tool mislocation (e.g. decenter etc.) and shape error (e.g. waviness), as well machine axis waviness.

The most common arrangement for STS configuration uses an encoder on the main spindle of a conventional diamond turning lathe (C-axis), forming a three axis (X-

Z-C) system. The cutting tool is oriented such that the entire cutting edge lies in the X-Z plane, and at any point on the part, cutting action occurs at a location on the rounded portion of the tool nose. This configuration, illustrated in Figure 6.1, is as used for operations described in this dissertation, and suggests expression of surface form in right cylindrical coordinates. Optical designers may use multiple coordinate system representations and functional basis sets when describing optical prescriptions. This requires an appropriate coordinate change to generate STS machine positions. The analysis and toolpath development presented in this chapter are performed in right cylindrical coordinates. The methodology developed is for the case of zero-rake, constant-radius tools, though it could be extended to tooling of any geometry.

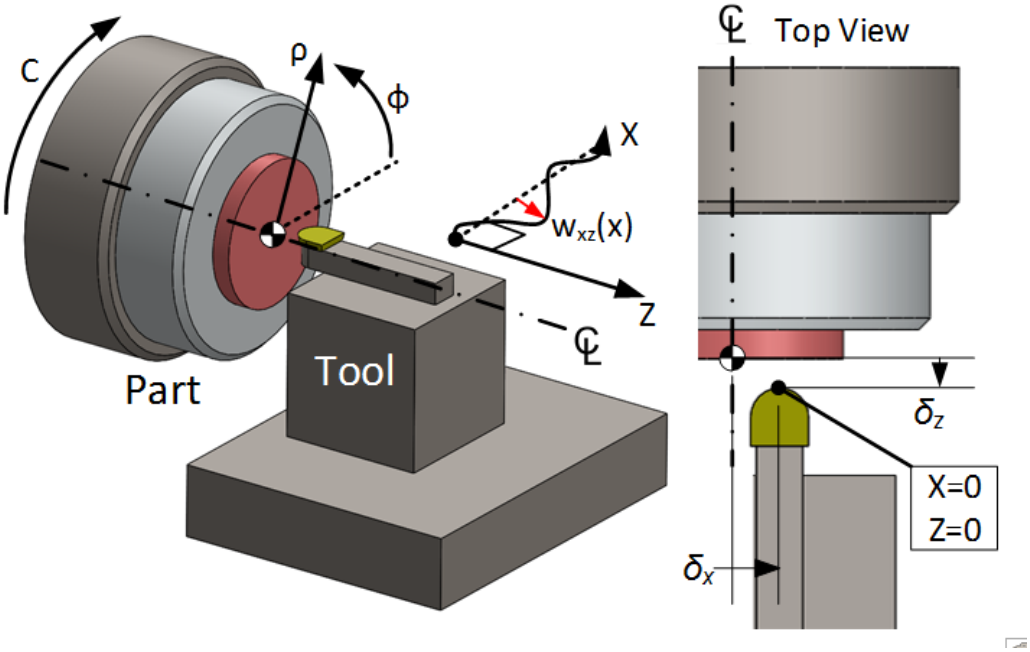

Figure 6.1: STS axis configuration and part coordinate system.

6.2 Tool Selection

Once a desired surface has been prescribed in the form of Eq. 6.1, slope and curvature analysis must be performed to select a cutting tool with appropriate reach and

access to cut the part without interference. The radius of the tool nose must be smaller than the minimum radius of curvature in any given ρ-z plane, while the tool clearance angle must be greater than the maximum slope in any given ρ-ϕ plane. These conditions are expressed in Eq. 6.2 and Eq. 6.3, respectively. While a tool may be specified as having a single radius, in practice, such tools have edge waviness which can be modeled as a radius deviation, dR_{ct}, which varies with location on the tool nose, as shown in Figure 6.2. These radius deviations can be as small as 50 nm for controlled-waviness tools, and as large as several micrometers for uncontrolled tools. In practice, these deviations can be modeled as a polynomial function of tool sweep angle, θ, using the notation of Eq. 6.4, or using any of the many appropriate spline-based techniques. For the optics manufactured here, a simple polynomial representation was sufficient.

Although the axes of the diamond turning machine are nominally assumed to be "perfect" in orthogonality and straightness, machine tool axis waviness often exists, affecting part accuracy. As most optics have a clear aperture radius which is much greater than the total surface sag, waviness of the X-axis will have the most profound effect on figure. As shown in Figure 6.1, this waviness can be modeled as a polynomial function of radial position, W_{xz}, indicating the waviness of the X-axis along the Z-direction.

$$\vec{\boldsymbol{s}} = \langle \rho, \phi, z(\rho,\phi) \rangle = \rho\hat{\boldsymbol{\rho}} + \rho\phi\hat{\boldsymbol{\phi}} + z(\rho,\phi)\hat{\boldsymbol{z}} \qquad \text{Eq. 6.1}$$

$$R_{ct} \leq \min\left(\left| \left(1 + \left(\frac{\partial z(\rho,\phi)}{\partial \rho} \right)^2 \right)^{3/2} \Big/ \frac{\partial^2 z(\rho,\phi)}{\partial \rho^2} \right| \right) \qquad \text{Eq. 6.2}$$

$$\beta_t \geq \left(\left| \tan^{-1}\left(\frac{\partial z(\rho,\phi)}{\rho \partial \phi} \right) \right| \right) \qquad \text{Eq. 6.3}$$

$$dR_{ct}(\theta) = \sum_{i=1}^{N} a_i \theta^i + \Delta R_{ct} \qquad \text{Eq. 6.4}$$

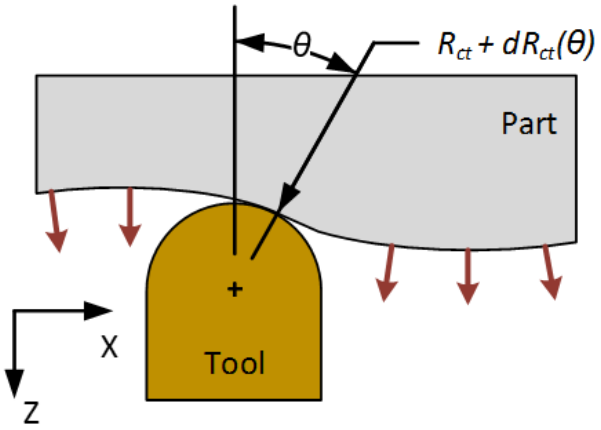

Figure 6.2: Tool edge near cutting zone.

6.3 Toolpath Generation

Conventionally-machined macroscale parts are well-represented in modern CAD/CAM packages by primitive solids and spline-based or NURBS surfaces. However, for optical components, which are typically described by a surface equation or prescription, representation of the prescription in a like manner can introduce unacceptable errors due to fitting and approximation schemes. Further these commercial software packages are not typically designed for optical tolerances and typically do not incorporate modules for compensation for tool waviness and machine axis non-orthogonality. Although several schemes [66] [67] have been developed for optimal selection of discrete toolpath point locations based on machine controller interpolation characteristics and control loop behavior, such work is beyond the scope of this dissertation. Instead, a simplified, robust analytical scheme is presented.

Toolpath generation begins with selection of raw, discrete coordinates on the part surface to be cut. A spiral of specified pitch from the maximum radius of the part to zero

radius is constructed on (ρ, ϕ), then the surface equation $z(\rho, \phi)$ is evaluated at each point on the spiral. The pitch, or stepover, of this toolpath spiral is selected to achieve a desired surface finish as computed by Eq. 2.4, or for brittle materials, to maintain a maximum chip thickness from Eq. 2.6 less than the critical value, whichever is more restrictive. The spacing between points on the toolpath spiral can be determined by prescribing a constant chord length or constant angular increment between points. By prescribing a nominal tolerable figure error (typically on the order of 20 nm) and determining the minimum radius of curvature in any ρ-ϕ plane on the surface, the maximum chord spacing between spiral points can be calculated from Eq. 6.5, from which an appropriate maximum angular increment can be calculated if desired.

$$r_{\phi z,min} = min\left(\left(1+\left(\frac{\partial z(\rho,\phi)}{\rho\partial\phi}\right)^2\right)^{3/2} \Big/ \frac{\partial^2 z(\rho,\phi)}{\rho^2\partial\phi^2}\right) \qquad \text{Eq. 6.5}$$

$$\gamma_{max} = 2\sqrt{e_{max}\left(2r_{\phi z,min} - e_{max}\right)}$$

The surface equation, in the form of Eq. 6.1, is then evaluated at each point on the toolpath spiral, and these surface points are offset by the tool radius along the direction of the component of the outward normal vector which lay in the ρ-z plane, given by Eq. 6.6. If tool waviness is known as a function of tool sweep angle, it can be compensated for at this time, because, as shown in Eq. 6.7, tool sweep angle is an exclusive function of part geometry. Finally, using Eq. 6.8, any known machine axis waviness can be compensated for after tool nose radius compensation.

$$\vec{\boldsymbol{n}} = -\frac{\partial z(\rho,\phi)}{\partial\rho}\hat{\boldsymbol{\rho}} + \hat{\boldsymbol{z}} \qquad \text{Eq. 6.6}$$

$$\hat{\boldsymbol{n}} = \vec{\boldsymbol{n}}/_{|\vec{\boldsymbol{n}}|}$$

$$\vec{\boldsymbol{g}} = \vec{\boldsymbol{s}} + \vec{\boldsymbol{n}}\big(R_{ct} + dR_{ct}(\theta)\big) = \langle g_\rho, g_\phi, g_z \rangle$$
$$\theta = \tan^{-1}\left(\frac{\partial z(\rho,\phi)}{\partial \rho}\right) \qquad \text{Eq. 6.7}$$

$$\vec{\boldsymbol{h}} = \vec{\boldsymbol{g}} + W_{xz}(g_\rho)\hat{\boldsymbol{z}} \qquad \text{Eq. 6.8}$$

A MATLAB® implementation of this toolpath generation strategy for STS operations is given in Appendix B.1 for reference.

6.4 Toolpath Verification

Commercially available CAM packages allow simulation, also known as backplotting, to validate generated toolpaths before physical machining begins. Likewise, when machining ultraprecision components using a novel path generation strategy such as presented, it is imperative to evaluate toolpath accuracy before cutting begins. Source code for a MATLAB® backplotter which accompanies the toolpath generator is given in Appendix B.2. This code includes necessary functionality to simulate effects due to tool and axis waviness, as well as tool offset error, which is discussed further in Section 6.5.1. This backplotter functions as follows:

1. A collection of *(ρ,ϕ)* backplot points, spaced closer than the toolpath points, is selected and generated. The optical surface equation *z(ρ,ϕ)* is evaluated at these points and this surface matrix is then shifted in the +Z direction by the intended depth of cut to represent the initial stock.
2. An interpolation is performed to determine the tool tip location along the Z-axis at each backplot point, assuming tool motion is along discrete linear segments between toolpath points. In practice, mechanical

smoothing of the toolpath will always be present due to machine axis inertial effects, but the assumption of linear motion allows simplification and in most situations represents the worst case scenario of resulting part error.

3. The tool is modeled numerically with its tip located at each point along the interpolated toolpath. At each point, the tool edge is compared to the stock and the lowest Z values are retained.
4. After simulation at each backplot point, the desired surface is subtracted from the cut surface to evaluate error. The resulting error map will include high spatial frequency content due to surface roughness as dictated by the cutting parameters and backplot point spacing, which can be removed by filtering if desired. Examination of the error map will indicate mid-spatial and form errors due to tool waviness, tool offset error, axis waviness, or toolpath inaccuracy if they exist.

To demonstrate the techniques, Figure 6.3 shows the results of toolpath backplotting with uncompensated and compensated toolpaths for a 10 mm diameter clear aperture, 10 mm radius of curvature concave sphere with the tool and axis waviness values given in Table 6.1. The tool and axis waviness values used here and elsewhere in simulation were chosen arbitrarily to generate form error trends which were easily observed, yet were of micrometer- or sub-micrometer magnitude, in order to verify the backplotter and toolpath generator to optical-level precision. Significant form error is evident in the backplot of the uncompensated toolpath, while the backplot of the compensated toolpath is free of form and mid-spatial errors, and is dominated by the

expected high spatial frequency sources such as surface roughness, confirming the validity of the demonstrated approach. Both toolpaths were generated with a stepover of 0.05 mm per revolution, which should correspond to a peak to valley cusp height of approximately 200 nm as calculated by Eq. 2.4, again confirmed by the simulation with acceptable accuracy.

Table 6.1: Error sources for Figure 6.3.

W_{xz}	-3.5e-5 mm/mm
a_1	2e-5/°
a_2	1e-5/°^{2}
a_3	-3e-7/°^{3}

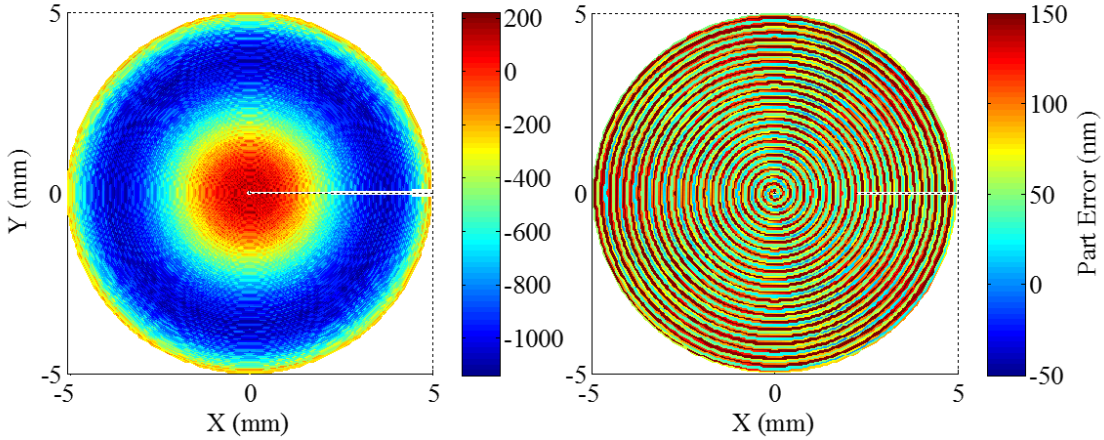

Figure 6.3: Backplotter simulations of uncompensated (left) and compensated (right) toolpaths for a concave sphere with error sources given in Table 6.1.

6.5 Tool Setup

Tool setup for a machining operation begins with initial location of the tool nose, accurate to approximately ±10 μm, using an on-machine tool locating microscope to program appropriate values into the numerically-controlled machine's tool offset table, and continues with face-machining of a planar artifact. If the tool tip is above the spindle centerline, a cone-shaped center defect will remain in the center of the artifact, while a tool that is too low will leave a cylindrical defect. Measurement of the center defect using the on-machine microscope, adjusting, and repeating is generally sufficient to set

tool tip height (y) origin within ±500 nm of the spindle centerline. In a similar manner, by plunging the tool into the workpiece at a commanded diameter and measuring the actual diameter of the resulting toric depression, indicated and actual tool radial (x) origin can be collocated within ±1 μm with respect to the spindle centerline. The top surface of the part is then typically located by advancing the tool towards the workpiece and recording the position at which an observable chip is first formed on the tool tip (touch-off).

6.5.1 Tool Offset Error

Any error in setting tool origin offsets in the machine tool controller will cause the actual tool location relative to the part origin to differ. For the STS configuration shown in Figure 6.1, a tool offset error along the Z axis will lead to a piston error term, while an offset error along the X direction will lead to a slope-dependent error which will be convolved with tool waviness effects. In this orientation, tool offset errors, δ_x and δ_z, are defined as positive when, the tool is actually located at a more positive axis coordinate than indicated by the machine.

While easily corrected, if known, by adjusting controller offsets, tool offset errors will result in part errors which can be determined by examining the cutting geometry shown in Figure 6.4 In the figure, one side of the tool nose is shown in the coordinate frame (x_t, z_t) whose origin is coincident with the nominal center of curvature of the tool edge. If the tool position as indicated by the machine controller is x, yet a tool offset error exists, the cutting action along the tool nose occurs at a location z_a instead of the intended z_i, resulting in a part error given by Eq. 6.9.

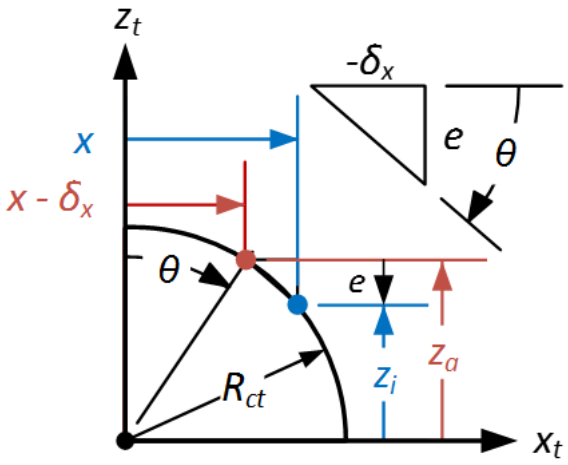

Figure 6.4: Cutting geometry used for derivation of Eq. 6.12.

$$e(\theta) = \delta_z + z_i - z_a \qquad \text{Eq. 6.9}$$

But, from basic geometry,

$$\begin{Bmatrix} x_t \\ z_t \end{Bmatrix} = R_{ct} \begin{Bmatrix} \sin\theta \\ \cos\theta \end{Bmatrix} \qquad \text{Eq. 6.10}$$

$$\begin{Bmatrix} z_i \\ z_a \end{Bmatrix} = \begin{Bmatrix} \sqrt{Rct^2 - x^2} \\ \sqrt{Rct^2 - (x_t - \delta_x)^2} \end{Bmatrix} \qquad \text{Eq. 6.11}$$

Therefore,

$$e(\theta) = \delta_z - R_{ct}cos\theta + \sqrt{{R_{ct}}^2\cos^2\theta + 2R_{ct}\delta_x\sin\theta - \delta_x^2} \qquad \text{Eq. 6.12}$$

But, if $Rct \gg \delta x$, tool sweep angle is small, so:

$$\begin{Bmatrix} \sin\theta \\ \cos\theta \\ \tan\theta \end{Bmatrix} \approx \begin{Bmatrix} \theta \\ 1 \\ \theta \end{Bmatrix} \qquad \text{Eq. 6.13}$$

And,

$$e(\theta) \approx \delta_z + R_{ct} - \sqrt{R_{ct}^2 + 2R_{ct}\delta_x\tan\theta} \qquad \text{Eq. 6.14}$$

Further,

$$R_{ct}^2 + 2R_{ct}\delta_x \tan\theta \approx R_{ct}^2 + 2R_{ct}\delta_x \tan\theta + \delta_x^2 \tan 2\theta = (R_{ct} + \delta_x \tan\theta)^2 \quad \text{Eq. 6.15}$$

So, if $Rct \gg \delta x$, Eq. 6.9 can be reduced to Eq. 6.16.

$$e(\theta) \approx \delta_z - \delta_x \tan\theta \quad \text{Eq. 6.16}$$

6.5.2 Tool Radius Deviation

The description of tool waviness given in Eq. 6.4, includes higher-order tool sweep-dependent terms as well as a deviation, ΔR_{ct}, between the specified and actual tool radius of curvature. In practice, as described in Section 6.5, the Z-axis position of the tool is set up for a cutting operation by physically touching the tool to the part and recording the position where a chip is first formed on the tip of the tool. Therefore, the tool is located relative to the part with reference to its tip, not its center of curvature. As a consequence of this arrangement, a deviation in tool radius will not simply result in a constant measured slope-dependent error. However, by simple geometric construction, it can be shown that the form error along the Z-axis of the part, resulting from a tool radius deviation is as given in Eq. 6.17

$$e(\theta) = \Delta R_{ct}(\cos\theta - 1) \quad \text{Eq. 6.17}$$

Therefore, Eq. 6.18 gives the total slope-dependent error present on a workpiece due to tool waviness and radius deviation, projected along the Z-axis of the part.

$$e(\theta) = \cos\theta \sum_{i=1}^{N} a_i \theta^i + \Delta R_{ct}(\cos\theta - 1) \quad \text{Eq. 6.18}$$

6.6 Calibration Artifacts

After initial tool setup, it is often useful to machine a calibration artifact to identify remaining tool offset errors, tool waviness, and axis waviness. The use of turned and milled artifacts for this purpose is described in [47]. However, the precision air bearing spindles used in typical diamond turning machines often exhibit different error motions when operated in position-controlled (STS) mode than when operated in spindle (turning) mode. Therefore, it is desirable to machine the calibration artifact in STS mode. Two types of calibration artifacts are viable, as described briefly in [68]: flats and spheres, which are easily measured using Fizeau interferometry.

6.6.1 Tilted Flat

For applications where small, nearly equal portions of both sides of the tool nose are utilized in cutting an optic, a tilted flat artifact of an appropriate angle to sample the necessary tool sweep is appropriate. However, the clearance angle of the tool must be greater than that of the tilted flat to prevent tool-workpiece collisions, limiting the maximum tool sweep that can be mapped using this technique. When feasible, tilted flats allow machine axis and tool error sources to be easily separated. Tool offset error can be determined directly by fitting Eq. 6.16 to the measured data. After subtracting errors attributable to tool offset error, axis waviness, can be discerned from radial slices of an artifact measurement, and tool waviness can be determined from circular slices of the measurement. Figure 6.5 presents predicted and simulated (backplotter) error maps due to various error sources for a 10 mm diameter, 3° tilted flat described by Eq. 6.19 and cut using an uncompensated toolpath and a 1.5 mm radius tool. Excellent agreement between simulation and prediction is evident.

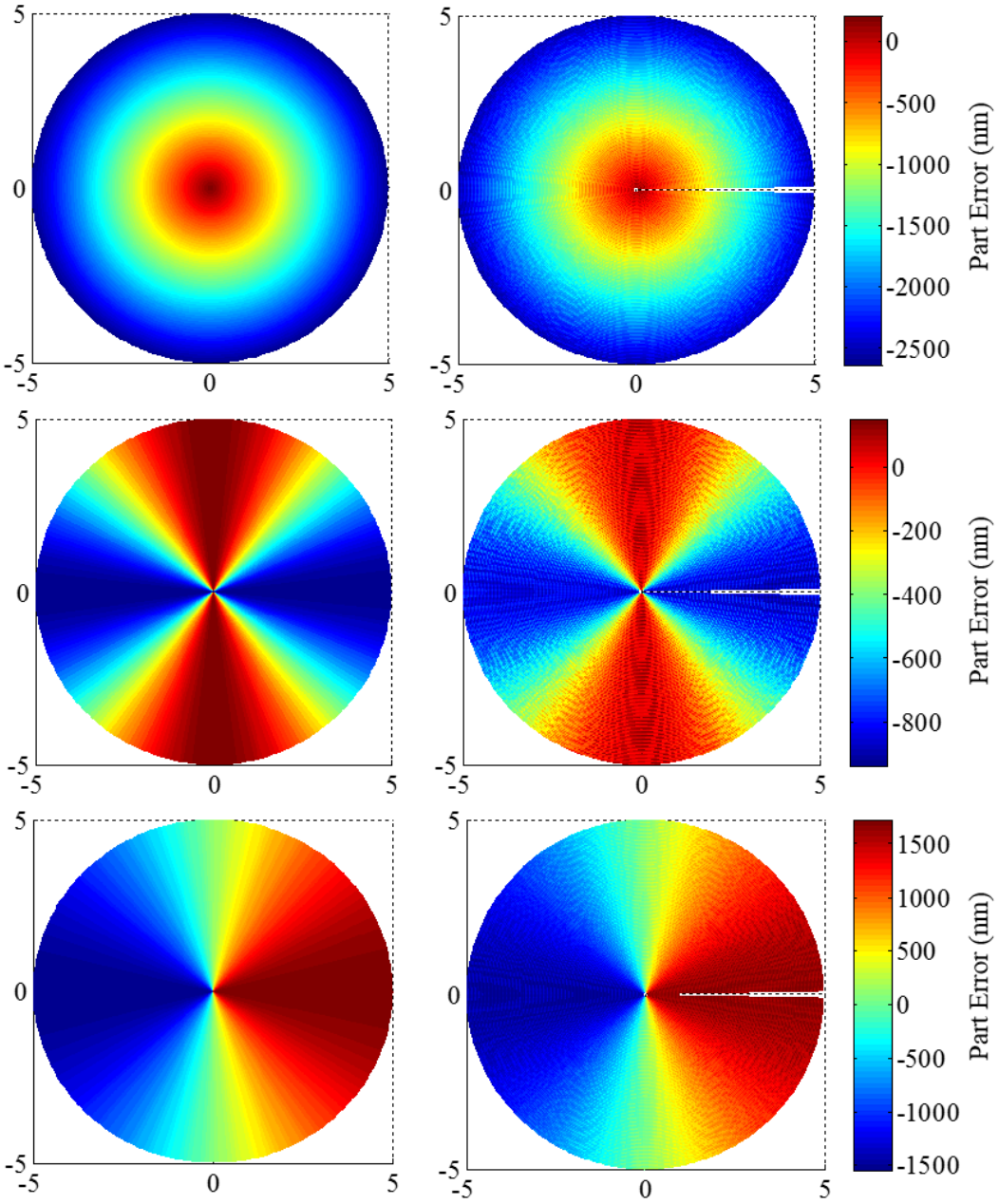

Figure 6.5: Predicted (left) and simulated (right) error maps for tilted flat from various error sources. (Top) axis waviness W_{xz}=5.2e-4 mm/mm, (center) tool waviness a_2=7e-5/°^{2}, (bottom) tool offset error δ_x=-0.03 mm.

$$z(\rho, \phi) = \tan(3°)\rho\cos\phi \qquad \text{Eq. 6.19}$$

As discussed previously, tool radius deviation cannot be determined simply from a plot of slope dependent error, but it may be calculated from a fit of the form of Eq.

6.17. The tool clearance limitations imposed by the geometry of the tilted flat prevent sampling of tool sweeps beyond approximately 7° for typical tools, for which the radius of curvature will have been measured and specified by the manufacturer to within ±1 μm or so. For these small tool sweep angles and small radius deviations, the resulting form error component is often much smaller than that due to other sources, and is difficult to separate from a parabolic (dependent upon θ^2) waviness trend. While this might initially seem to limit the practicality of the approach, for the purposes of producing an accurate part, its acceptable to compensate the toolpath for either a tool radius deviation or for second order tool waviness, as long as the chosen setup artifact samples the entirety of the tool edge to be used in part manufacture.

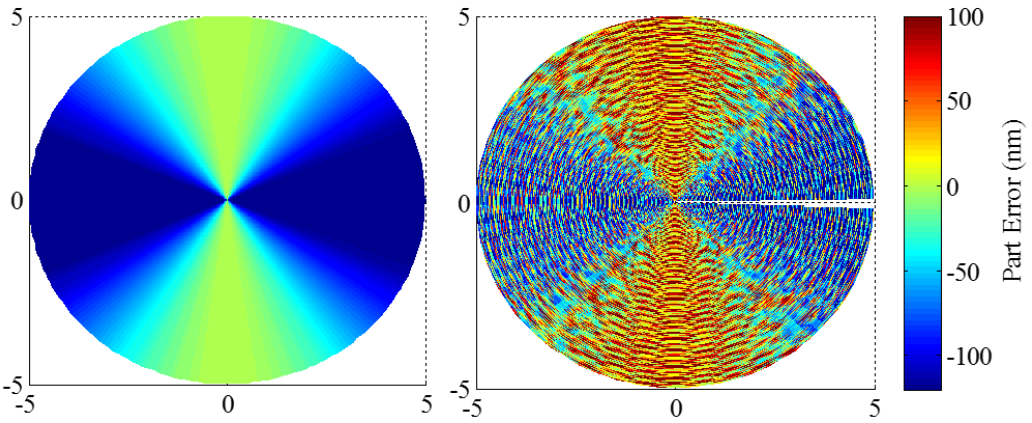

Figure 6.6: Predicted (left) and simulated (right) error maps for 3° tilted flat with tool radius deviation of ΔR_{ct}=0.1 mm.

Figure 6.6 compares predicted (from Eq. 6.17) and simulated error maps resulting from tool radius deviation for the 3° tilted flat. Although agreement exists between predicted and simulated results, even for such an exaggerated value, the error magnitude due to tool radius deviation is much smaller than other components, and is on order of that produced by cusp structure from tool feed motion across the part.

6.6.2 Concave Sphere

For applications where larger portions of a single side of the tool nose are used, a concave sphere is a suitable artifact, and allows mapping large tool sweeps while requiring less tool clearance than a tilted flat. If only one side of the tool must be mapped, a centered concave sphere can be machined in STS mode and requires minimal tool clearance. If a small portion of one side of the tool nose and a much larger portion of the other side are to be utilized during machining, both can be mapped using a single artifact if the concave sphere is slightly decentered (see [68]). However, a decentered sphere places more stringent constraints on required tool clearance as radial decenter increases. If large portions of both sides of the tool are required, there is little alternative other than to machine two separate artifacts to fully map the tool.

Unlike a tilted flat, for the case of a centered sphere, tool and machine error sources are both apparent in radial slices of the artifact measurement and are not easily separable. Figure 6.7 presents error maps in the style of Figure 6.5 for a centered concave sphere with a 10 mm diameter clear aperture and a 10 mm radius of curvature, cut using a 1.5 mm radius tool and an uncompensated toolpath. Again, agreement between prediction and simulation is evident, confirming the geometrical models developed earlier in this chapter.

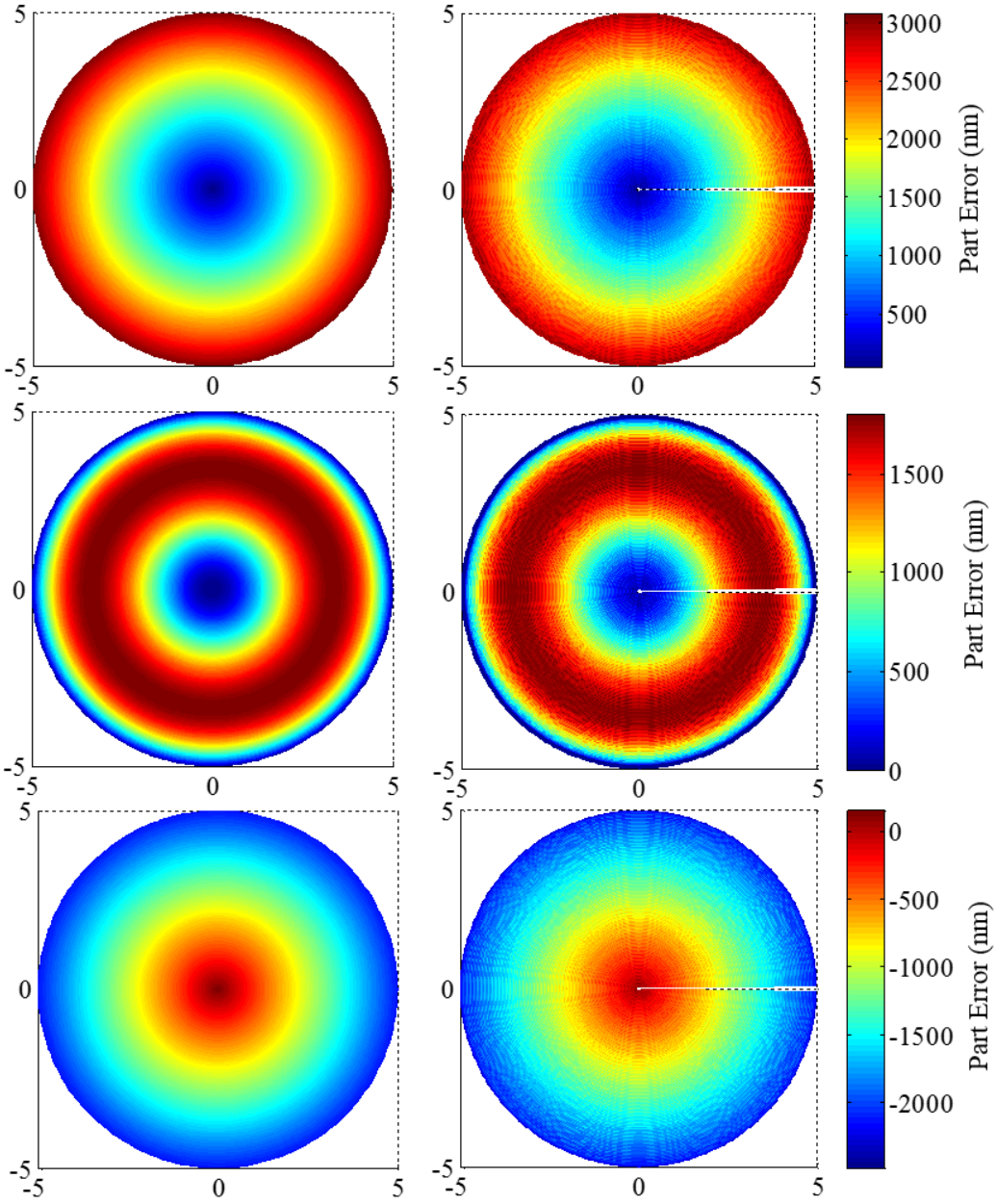

Figure 6.7: Predicted (left) and simulated (right) error maps for concave centered sphere from various error sources. (Top) axis waviness W_{xz}=-5.2e-4 mm/mm, (center) tool waviness a_3= 4e-7/°^{3}, a_2=-1.2e-5/°^{2}, (bottom) tool offset error δ_x=-0.005 mm.

Tool offset error results in an ogive-shaped true error trend on a centered concave sphere, as illustrated in Figure 6.8 for several values of δ_x. When Fizeau interferometry is used to measure form of a concave sphere, confocal alignment places the center of curvature of the part under test with that of the transmission sphere used to create a

spherical reference wavefront. By virtue of this arrangement, the Fizeau interferometer measures departures from a best fit sphere, and not from the ideal sphere. Therefore, the true form errors given in Figure 6.8 are manifest as characteristic M- or W- shaped errors in the resulting Fizeau measurement, as shown in Figure 6.9.

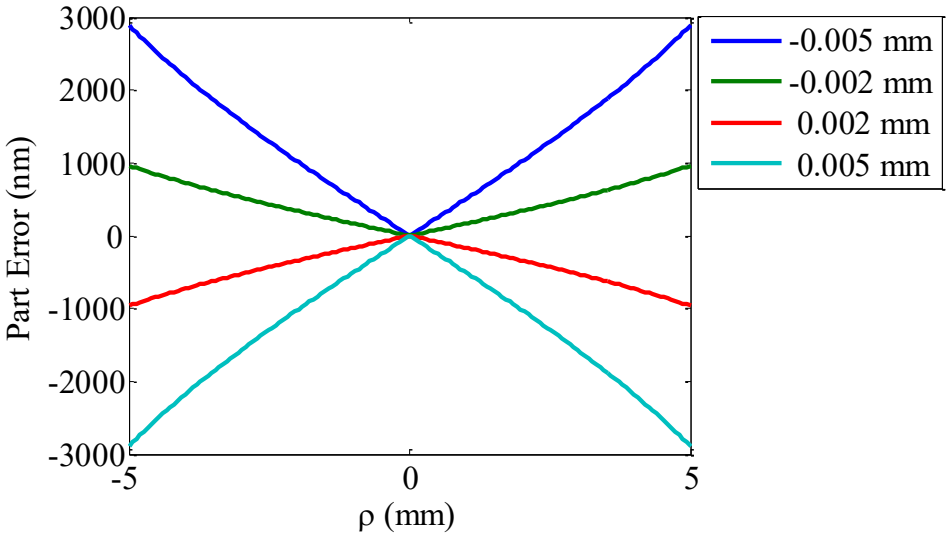

Figure 6.8: True form errors due to tool offset error δ_x.

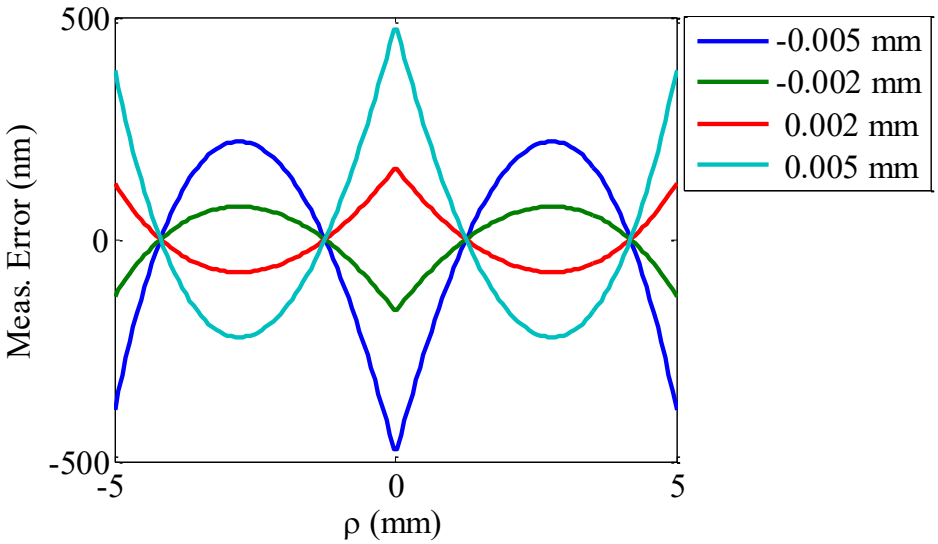

Figure 6.9: Apparent form errors due to tool offset error δ_x.

If no other error sources such as tool waviness or axis misalignment are present, the tool offset error, δ_x, can be estimated with Eq. 6.20 using the artifact radius of curvature, clear aperture diameter, and the peak to valley magnitude of departure from best fit sphere, $e_{pv,fiz}$, determined from the Fizeau measurement. This relation, which is given in the operator's manual for all Moore Nanotechnology machine tools, is also valid for artifact form measurements performed using a profilometer.

$$\delta_x \approx \frac{8\,ROC}{CA} e_{pv,fiz} \qquad \text{Eq. 6.20}$$

In practice, however, the presence of other error sources prohibits direct determination of tool offset error, and because the Fizeau interferometer measures departures from a best fit, not the ideal sphere, tool offset error cannot be calculated from Eq. 6.16. Instead, to determine tool offset error, a recursive numerical process must be performed which is detailed in [47] and proceeds as follows:

1. The ideal spherical artifact geometry is added to the Fizeau measurement and all data points are converted to a right spherical coordinate system representation.
2. A test shift value is added to the radial coordinate values.
3. A best fit sphere is removed from the radially-shifted coordinates.
4. Steps 1-3 are repeated until a radial shift value is determined which minimizes the peak to valley error resulting from step 3. This value is the tool offset error.

After isolating and removing error due to tool offset error, analysis and determination of tool and axis waviness can proceed as for a tilted flat artifact. However, as indicated by

Eq. 6.17, the effect of tool radius deviation on a sphere will only be to produce a spherical geometry of differing radius than desired. Due to the nature of the Fizeau interferometer which measures departures from best fit sphere when placed at confocal alignment, tool radius deviation will be indistinguishable in the measurement. To properly observe tool radius deviation on a spherical component using a Fizeau interferometer, two measurements must be made using a radius bench configuration to note the distance between confocal and cateye alignment positions. If no radius bench apparatus is accessible, a rudimentary confirmation of tool radius may be made by using the on-machine microscope to compare the theoretical and actual clear aperture diameter of the spherical recess.

CHAPTER 7: SLOW TOOL SERVO PROCESS VERIFICATION

7.1 IRG 26 Freeform Lens Pair

As presented in previous chapters, the main steps for manufacture of a freeform optics are: (1) selection of appropriate cutting parameters; and (2) generation of a machine toolpath, corrected for machine and tool errors, in MATLAB® from the optical prescription. This chapter presents a verification of the STS process methodology through manufacturing, metrology, and functional testing of a chalcogenide glass freeform lens pair, an Alvarez lens, which is also presented in [68].

The original Alvarez lens design, as described in the patent [5] [69], described a variable-focus system using identical freeform surfaces which are described by the polynomial in Eq. 7.1, where A and C are the Alvarez constant and surface base height, respectively. When two of these identical surfaces are placed opposing each other with collocated origins, the composite of the two surfaces forms a plane and light rays passing through the composite surface will not be deflected. If a small lateral shearing displacement, d, along the x-axis is introduced between the surfaces, the composite is equivalent to a spherical element which can have positive or negative optical power, depending on shear direction, as illustrated in Figure 7.1. The effective focal length, f, of such as system is given in Eq. 7.2, where n is the index of refraction of the lens material.

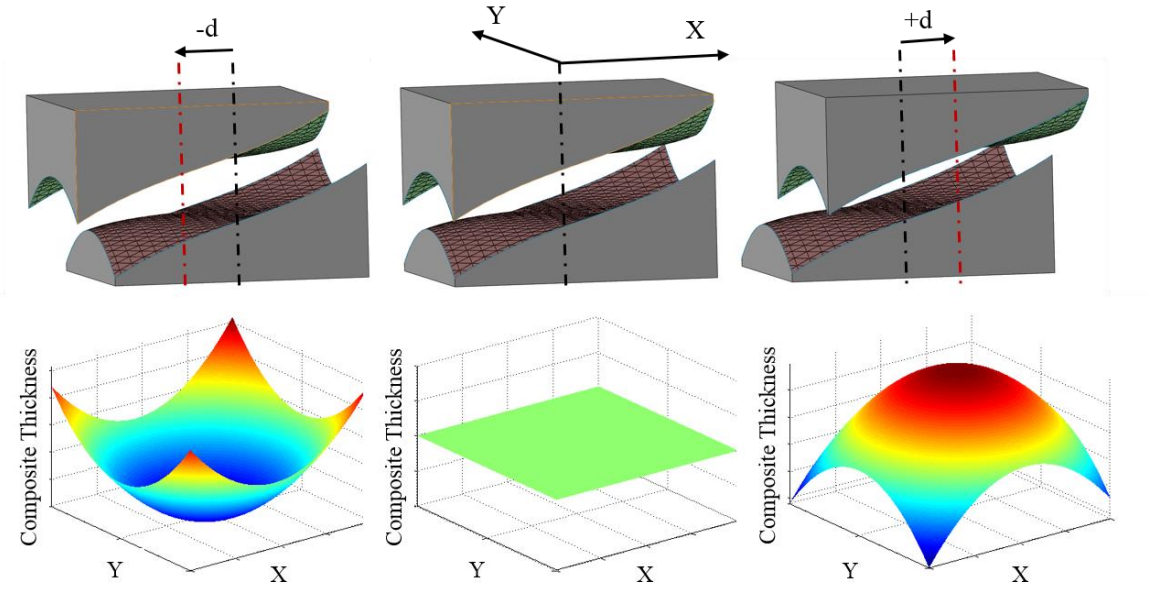

Figure 7.1: Composite thickness of displaced cubic Alvarez surfaces.

$$z(x,y) = Ax\left(\frac{x^2}{3} + y^2\right) + C \qquad \text{Eq. 7.1}$$

$$f = \frac{1}{4Ad(n-1)} \qquad \text{Eq. 7.2}$$

While a cubic Alvarez pair has zero optical power at zero shear (d=0), some system designs require positive power at zero shift. Further, focal length change with for a negative power arrangement is not easily evaluated in a functional testing setup. Using Zemax®, colleagues designed a software-optimized variable-focus system of 14.5 mm clear aperture diameter using polynomial terms up to 14th order, such that over a shear of ±1.8 mm, the focal length at zero shear (d=0) was approximately 77 mm and could be varied from 38.5 mm to infinity. The surface prescription for the optics is given in Appendix A.1 for reference. The optics were designed for thermal imaging using IRG 26 at wavelengths from 3 to 5 μm. By utilizing these higher order terms, the peak to valley height of the optical surface was reduced in comparison to the equivalent Alvarez surface from Eq. 7.1 needed to produce a given focal length. This improved manufacturability by

reducing the amount of material that had to be removed. The functional surface of one of the two identical elements is shown in Figure 7.2. The total sag is approximately 200 micrometers.

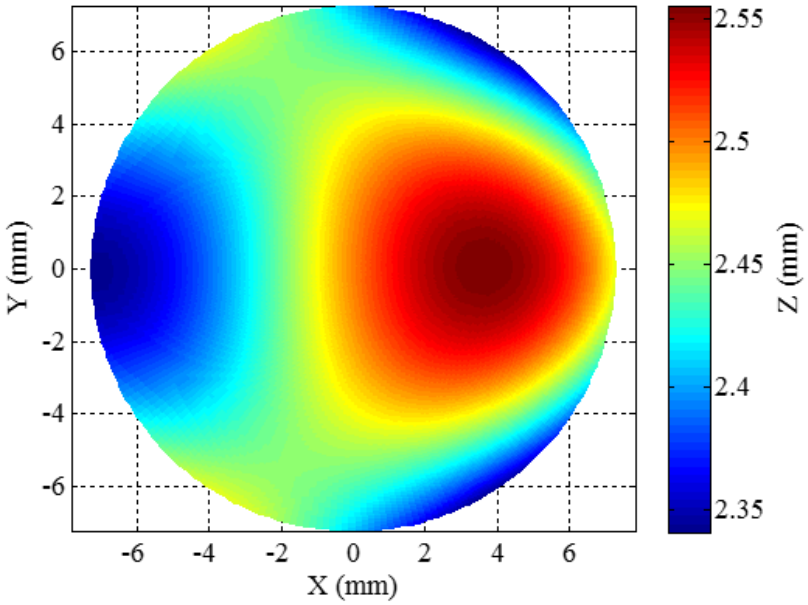

Figure 7.2: Optical surface of IRG 26 high order freeform lens.

7.2 Manufacturing

Slope analysis of the optical surface, shown in Figure 7.3, indicated that for STS cutting of the optics the effective rake angle of the tool would vary by ±1.5°. Further, only ±4° of the tool nose would be used in the cutting. Curvature analysis indicated that the maximum tool possible tool radius, as determined by Eq. 6.2 was 42.1 mm. Because it is known from Section 4.4.3 that positive effective rake angles of 1.5° produce optical finish in IRG 26, a zero-rake controlled waviness tool with a 1.5 mm nose radius and 5° clearance was selected for machining these components.

After initial tool setup, tool waviness was mapped by STS machining of a tilted flat. To sample nearly the full range of tool sweeps (±4°) used for this part while

minimizing required tool clearance for the artifact machining and using the same region of the machine axes intended for machining the final part, a 3° tilted flat was machined on a 12.5 mm diameter oxygen free high thermal conductivity (OFHC) copper workpiece with an orientation flat along one side.

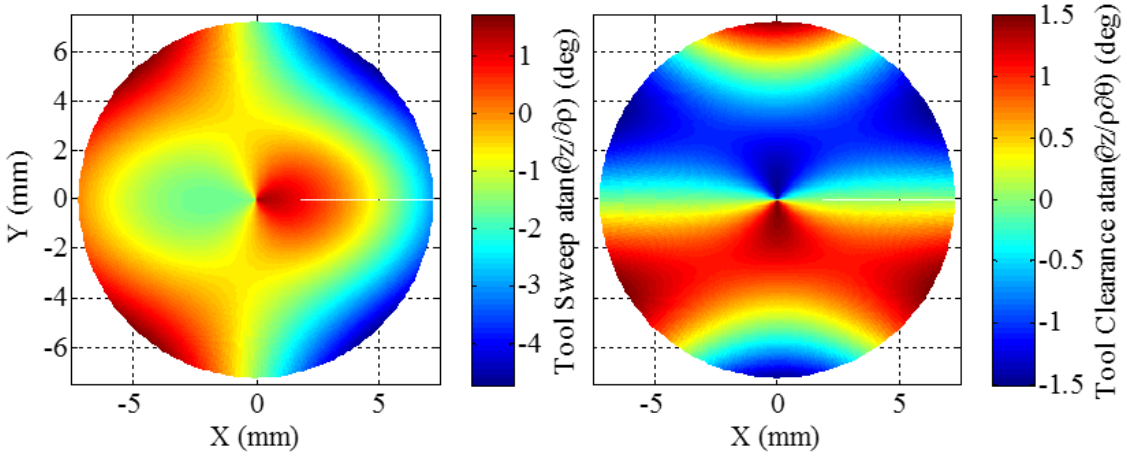

Figure 7.3: (Left) required tool sweep and (right) required tool clearance for IRG 26 freeform lens pair.

Machining parameters for this artifact were selected to minimize cutting time and produce a surface finish of approximately 3 nm Ra. The artifact was machined to a near-net shape using a conventional CNC machining center, then mounted on the Moore Nanotech 350FG and allowed to come to thermal equilibrium over a 10 hour period. Rough machining was performed with a 25 µm depth of cut, 25 µm feed per revolution, and a light mineral oil mist. Finish machining was conducted with a 5 µm depth of cut, a 10 µm feed per revolution, and lubrication via a thin jet of mineral oil directed through a hypodermic needle towards the cutting zone. In coordinated axis machining C axis positions must be directly specified. The angular resolution for C axis positions was 1° for both roughing and finish operations. After machining the artifact with an uncompensated toolpath, the flat was measured using the Zygo VeriFire ATZ. Results

are shown in Figure 7.4. The uncompensated artifact had a P-V form error of 140 nm. While a waviness trend was not apparent, a slight cone-shaped error trend, likely due to machine axis misalignment. This was compensated in the toolpath, the artifact was recut, and the results are shown in Figure 7.5.

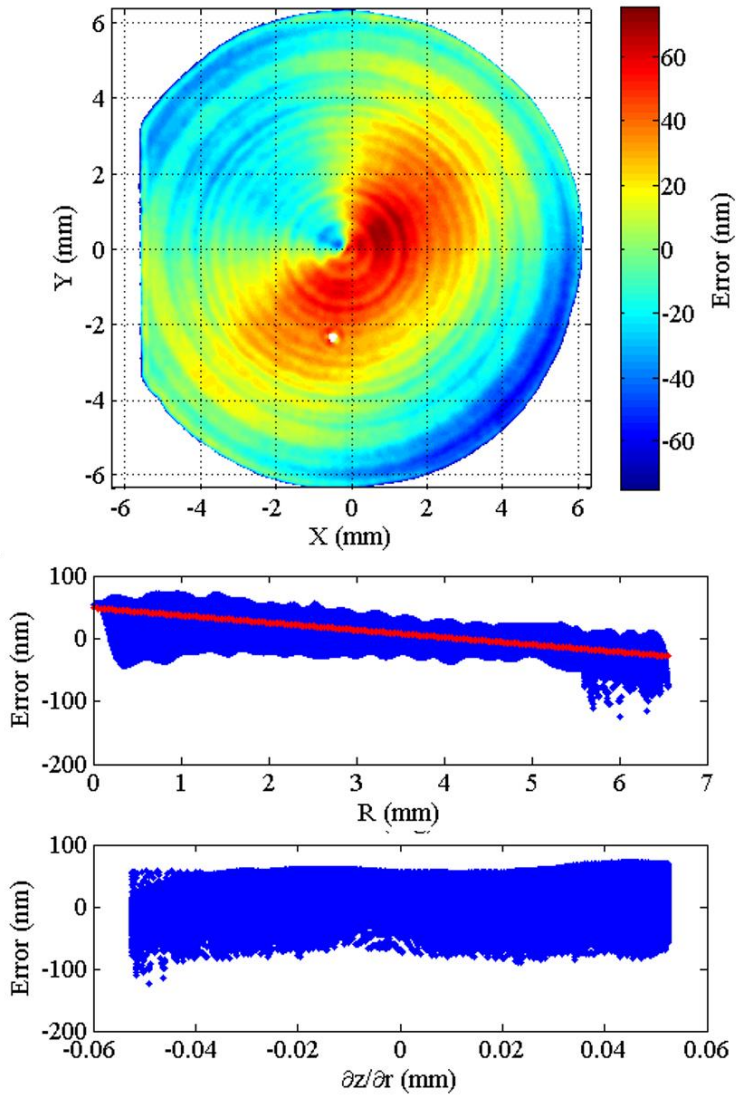

Figure 7.4: Uncompensated setup artifact measurement. From top: error map, error vs. part radius, error vs part slope $\partial z/\partial r$.

After removing erroneous data near a small dust spot near the bottom-right of the measurement, the corrected artifact had a P-V form error of approximately 100 nm. An

erroneous region still persisted in the upper left quadrant of the measurement near the center of the part, which was also present in the uncorrected artifact. Form errors of similar magnitude and a similar upper-left quadrant error were observed in a larger-diameter tilted flat in [65] machined by the machine tool manufacturer, suggesting that for this cutting configuration, a lower bound on form accuracy may have been reached. These same errors were expected to be reproduced on the actual optic, and were not large enough to cause the part to be out of tolerance for this application.

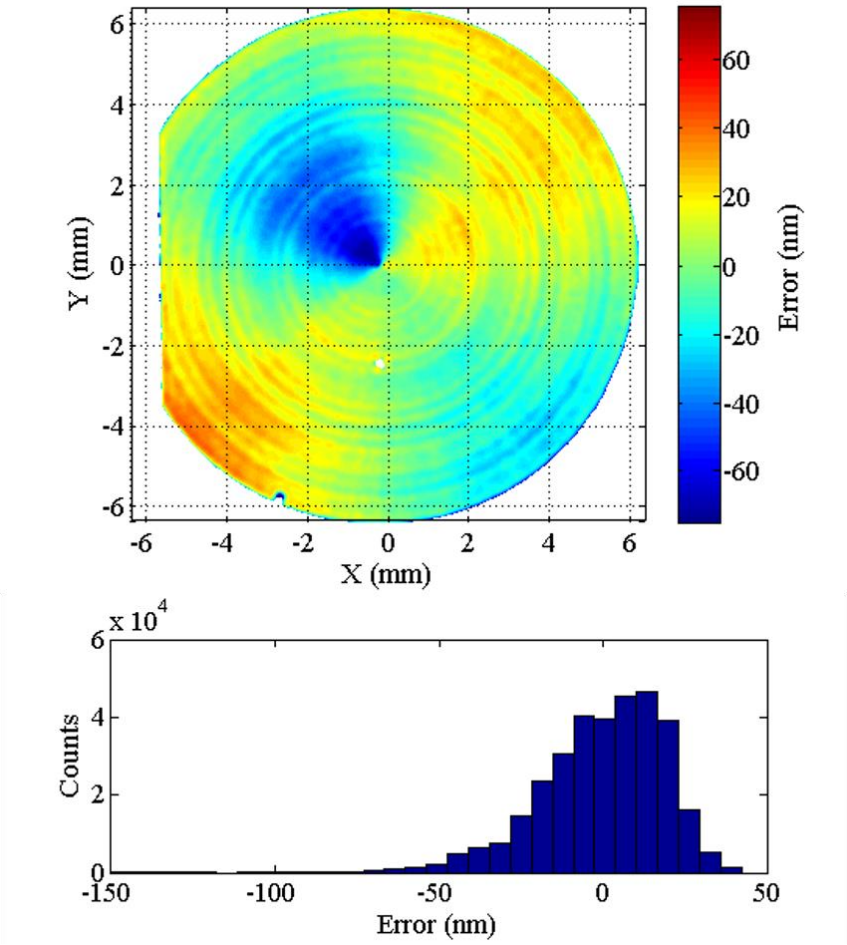

Figure 7.5: Measurement of compensated setup artifact with error histogram.

After machining and analysis of the setup artifact, the high order freeform lenses were machined from 25.4 mm diameter, 4 mm thick IRG 26 cylindrical blanks. The

blanks were first prepared by face turning one side to a thickness of approximately 3 mm. The part was flipped, then the part was faced on the other side to a final thickness of approximately 2.65 mm. The outer diameters were turned to 25.3 mm, then the workpieces were machined to leave a 14.5 mm diameter pedestal above a 1.5 mm thick base. After preparation, the functional surfaces were machined using the STS process.

To allow thermal equilibration, roughing passes were performed in air above the part for 12 hours. All toolpaths were generated with an angular spacing of 0.1°. To maximize material removal rate, 15 roughing passes were performed in a brittle-dominated mode with 25 μm depth of cut and 25 μm feed per revolution, corresponding to a 4 μm maximum chip thickness, with a light mist of mineral oil lubrication. To remove forward-propagated damage due to brittle-dominated rough machining and produce the final optical surface, 4 finishing passes were then performed at 7.5 μm depth of cut and a 2 μm feed per revolution, corresponding to a 200 nm maximum chip thickness. Chip evacuation during roughing operations was unsatisfactory, so a fine jet of mineral oil directed at the cutting zone was used for finish machining to reduce adhesion of chips to the part. Based upon operator judgment that a finish of 2 nm P-V or better would be appropriate, these finishing parameters were selected to provide a theoretical 1.3 nm P-V surface finish, and given this surface finish restriction, were not limited by the critical chip thickness at which brittle-dominated machining begins. Finish cuts were performed using the error source compensation parameters identified in the machining of the tilted-flat setup artifact. These cutting parameters are summarized in Table 7.1. A portion of the toolpath used for the roughing passes, as well as the final optics, is shown in Figure 7.6.

After STS machining, two 1.95 mm wide slots, as well as an orientation flat, were milled into each substrate using a 1 mm diameter carbide endmill at 39000 rpm. These features mated with a custom-designed lens holder in the functional test set-up.

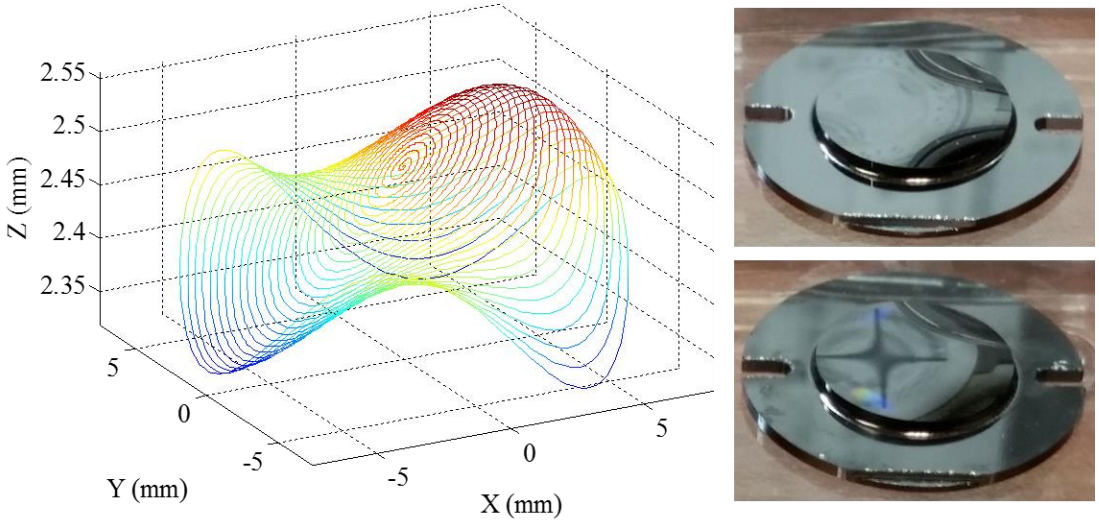

Figure 7.6: STS freeform lens toolpath (left) and final optics (right)

Table 7.1: IRG 26 freeform lens pair machining parameters

	Roughing	Finishing
Depth of cut	25 µm	7.5 µm
Feed per revolution	25 µm	2.0 µm
Point spacing (angular)	0.1°	0.1°
Lubrication	Mist	Flood
Cycle time (per pass)	18 min	224 min

7.3 Metrology

Examination of the STS freeform lens pair with SWLI at 50x indicated a surface roughness of 2 nm Sa, as measured at six places on each lens. To enable an initial form verification, an 11x11 grid of SWLI measurements at 5x magnification (1.66 mm square FOV) was taken on one of the lenses with 30% overlap and was stitched together. The part was soft-fixtured using clay to a rigid aluminum plate for measurement. Locations on the lens surface with local slope greater than the objective's acceptance limit of

approximately 3° were excluded from further analysis. Because this stitched measurement represented only a floating point cloud, a least-squares routine which minimized the error difference between the measured and target points was utilized to align the measured data to the nominal lens prescription, indicating a peak to valley form error of 1.726 μm with an RMS deviation of 100 nm. For comparative purposes, the same lens was mounted with clay to a steel gauge pin and measured with the OptiPro UltraSurf 5x instrument, using a chromatic confocal probe with 25° acceptance angle and sampling data every 0.05 mm. To reduce noise, a 6x6 Gaussian filter was applied, then the filtered data was again aligned to the nominal part prescription using a least squares minimization routine, indicating a peak to valley form error of 1.660 μm with an RMS deviation of 256 nm. Both measurements are shown in Figure 7.7.

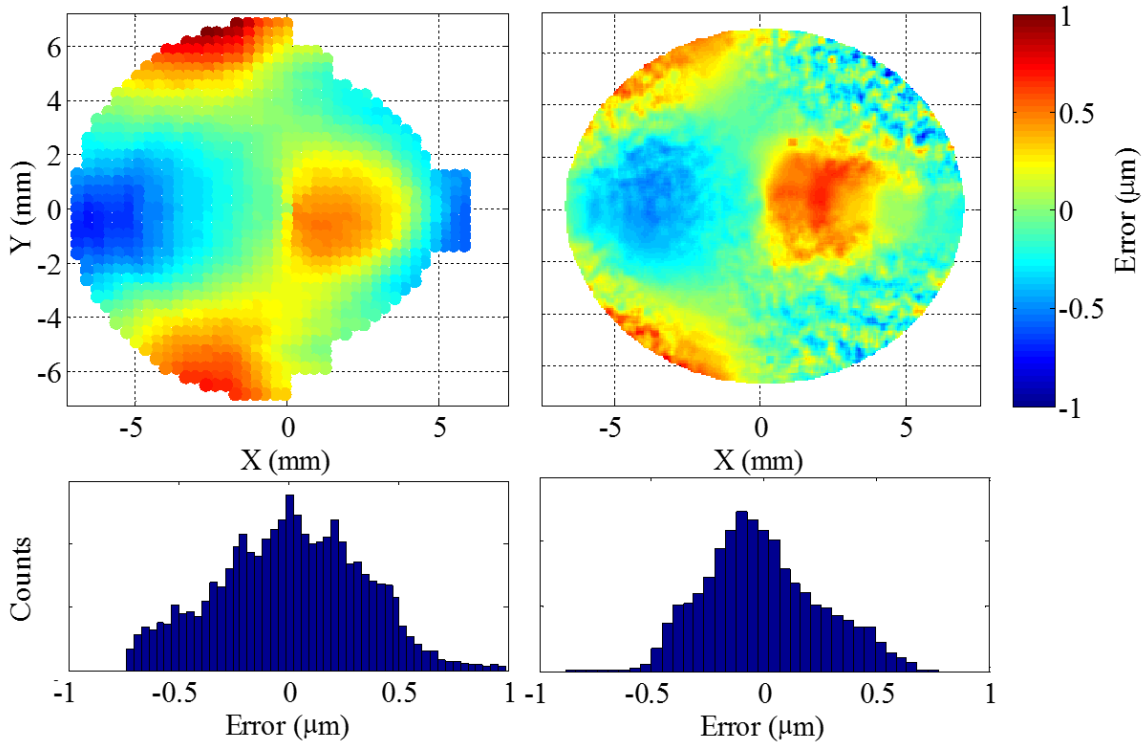

Figure 7.7: (Left) SWLI stitch and (right) UltraSurf measurement of STS freeform lens pair.

Measurements agree both qualitatively and quantitatively. It is highly unlikely that the tool edge state changed between machining of the setup artifact and component, so tool waviness can be discarded as a likely cause of the errors. Further, no value of tool offset could be determined using Eq. 6.16 which would produce an error trend that correlated with the measurement. Visual comparison shows the part error to be similar in form to the actual part prescription (for example, the minima and maxima of the form error and surface prescription are visually coincident), suggesting that these form errors may be caused by the machine tool's axis dynamics, possibly a motion overshoot error. This hypothesis is reasonable, considering that during machining of this part at approximately 16 rpm, the machine's Z-axis oscillated on order 200 μm and the X-axis on order of 750 μm during each revolution of the part (0.27 Hz), but a complete

characterization of the machine axis dynamics similar to that in [65] would be necessary for confirmation.

7.3.1 Uncertainty Sources

While the SWLI stitch and UltraSurf measurement of the lens agree and provide reasonable cross-validation, both are plagued by many uncertainty sources. A full uncertainty evaluation of either instrument is beyond the scope of this dissertation. However, it is notable that both measurements resulted in a floating point cloud which was registered to the nominal prescription using the same least squares minimization routine.

To evaluate the presence of any errors due to the point cloud registration scheme, a Monte Carlo simulation was performed. During each iteration of the simulation, a sparse, random sampling (360 points) of points was taken from the nominal freeform lens pair prescription. Then, random rotations (R_x, R_y, R_z) between ±5° were applied about the X, Y, and Z axes. Random translations (T_x, T_y, T_z) between ±5 mm were applied along the same axes. The least squares minimization routine was then used to register the rotated and translated data to the original data points, recovering the applied rotations and translation. 5000 iterations of the simulation were performed, and as illustrated in Figure 7.8, the applied rigid body transformations were generally well-recovered. Values of recovered rotations and translations were in agreement with values recovered using several available implementations of the iterative close point (ICP) algorithm, indicating that improper point cloud registration was not a significant contributor to the measured lens form error.

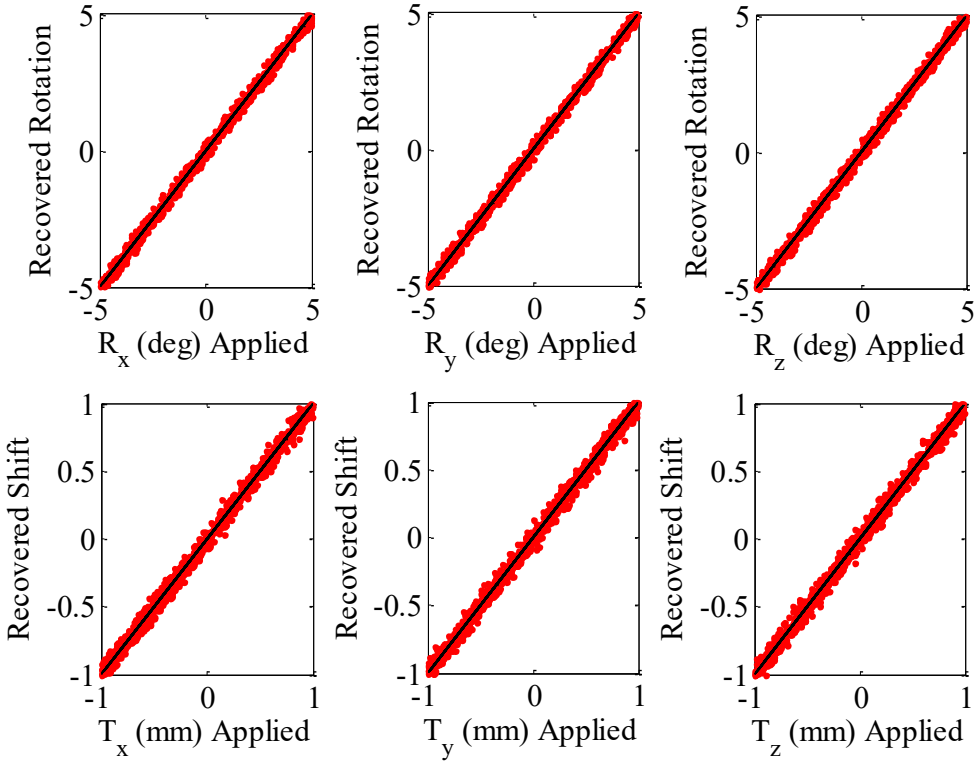

Figure 7.8: Results of Monte Carlo simulation of least squares minimization routine for point cloud registration.

To separate the accuracy of the SWLI stitching technique from the accuracy of the point cloud registration technique, the compensated setup artifact was measured using a 9x9 stitched grid of 5x (1.66 mm square FOV) measurements with 30% overlap. This part geometry does not require a 6 degree of freedom registration. Instead, removal of only a best fit plane and appropriate clocking as indicated by the orientation flat yields a measurement which can be directly compared with results of a well-known and accepted technique such as Fizeau interferometry. Figure 7.9 presents the stitched measurement as well as the Fizeau measurement from Figure 7.5, replotted for comparative purposes.

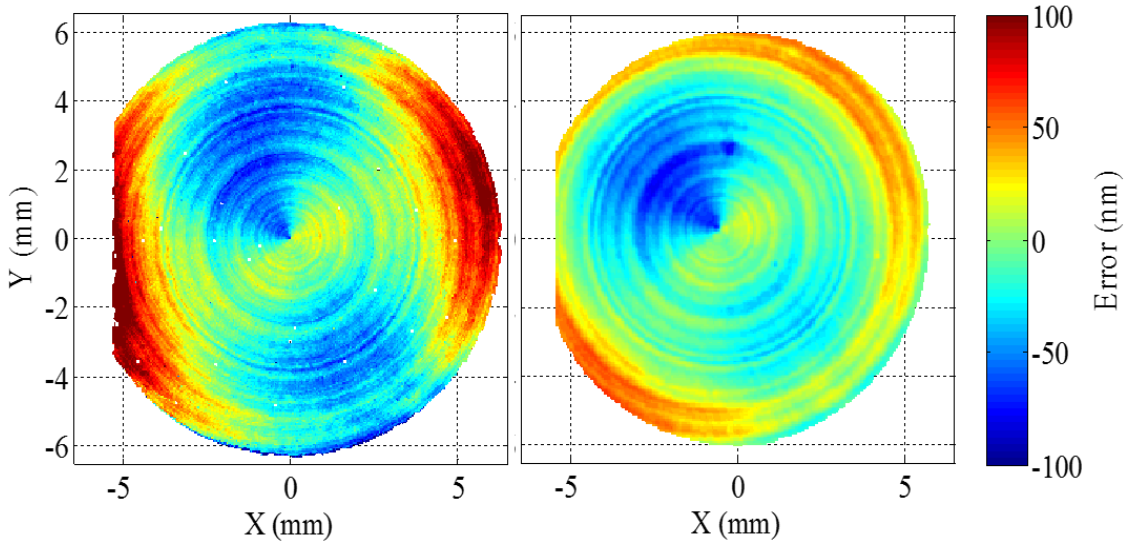

Figure 7.9: (Left) SWLI stitch and (right) Fizeau measurement of compensated setup artifact.

The form and magnitude of the stitched and Fizeau measurements are in agreement to within approximately 20 nm, indicating that over the slope and size range sampled on these parts, uncertainty in the SWLI hardware or stitching algorithm is not a significant contributor to the measured component error. The findings of this evaluation of error source candidates, as well as the general agreement between stitched and UltraSurf measurements of the lens, indicate that in the absence of other explanation, the measured form errors are accurate representations of the true form error of the measured lens.

7.4 Functional Testing

After machining and metrology, each freeform element was mounted to a three-axis micrometer-driven optical stage using a custom-built bracket and mounting ring. Both stages were mounted to a fixturing plate appropriately to provide a 500 μm gap between the lenses, and this completed lens assembly was mounted atop a Newport ILS linear motion stage, which was placed in front of and driven along the optical axis of an

Indigo Phoenix thermal imaging camera. This liquid nitrogen-cooled camera has 30 μm square pixels and detects wavelengths between 3 μm and 5 μm. A hot plate, located approximately 2.5 m away, was used as a thermal source, and an adjustable pinhole was used to block stray light. This test arrangement is shown in Figure 7.10.

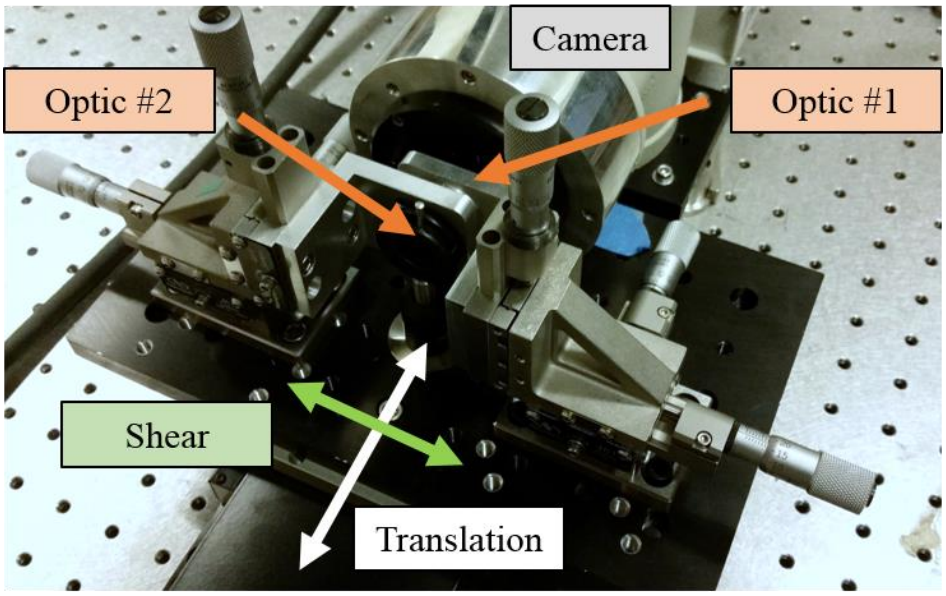

Figure 7.10: Setup for functional testing of freeform lens pair.

After initial alignment, the entire lens assembly was translated along the linear motion stage while monitoring the camera image. The best focus position was located for shear displacements from -0.8 to +1.0 mm. In a similar testing procedure described in [27], shear displacement was introduced by translating only one optic, which led to tilted images. In this investigation, shearing was introduced by displacing each optic an equal distance away from the camera's optical axis. The procedure was repeated three times for each shear displacement value. Overall performance of the system was excellent, clearly demonstrating the variable-focus mechanism, as shown in Figure 7.11. Sample images of the hot plate, predicted focal lengths, as well as measured focal lengths for an identical system machined using a ball end-milling process [47] are shown for reference.

Over the majority of the test range, both theoretical and milled focal lengths lie within the experimental uncertainty. For large negative shear displacements, deviations from predicted values are larger. At these displacements, focus is more difficult to find due to increased depth of field and reduced image magnification, and consequently, image fidelity.

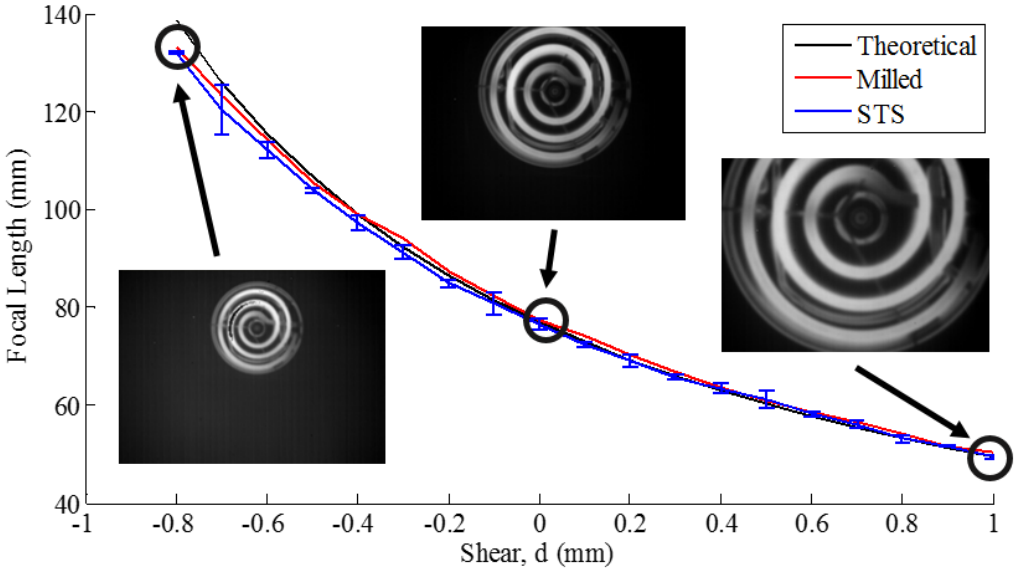

Figure 7.11: Focal length variation of freeform lens pair system.

CHAPTER 8: APPLICATION: FREEFORM IMAGING SPECTROMETER

8.1 Introduction and System Overview

While the ability of freeform optics to enable novel surface function was demonstrated in the previous chapter, freeform surfaces can also be used to improve performance and reduce overall system volume of traditionally designed optical systems [3]. The traditional Offner-Chrisp imaging spectrometer [70] [71] [72] consists of an entrance slit, three concentric spherical surfaces, and a detector array. The primary and tertiary optics are concave spherical mirrors, while the secondary optic is a convex spherical grating. As demonstrated in [73], the use of freeform surfaces for the primary and tertiary optics allows an approximate 5x reduction in overall system volume, adds additional degrees of freedom for correction of spectral broadening and distortion, and generally produces a smaller system with performance equal or better than that of the traditional design. The final system design developed by Reimers et al. utilizes a convex spherical secondary optic with blazed grating and specifies the primary and tertiary optics as combinations of base concave spheres and surfaces from the fringe Zernike set. The surface prescriptions, as well as a table of the fringe Zernike polynomials in cylindrical coordinates are given in Appendices A.2 and A.3. Although a complete description of the optical design is beyond the scope of tis dissertation, a brief summary of the system specifications is given in Table 8.1. This chapter presents the design of an

optomechanical solution for physical realization of the device, as well as manufacturing and initial metrology of the primary and tertiary mirrors.

Table 8.1: Imaging spectrometer specifications

Type	Freeform Offner-Chrisp
Entrance slit width	10 μm
Field of view	10 mm
Spectrical dispersion	100 nm/mm
Wavelength range	500-100 nm
F number	F/3.8

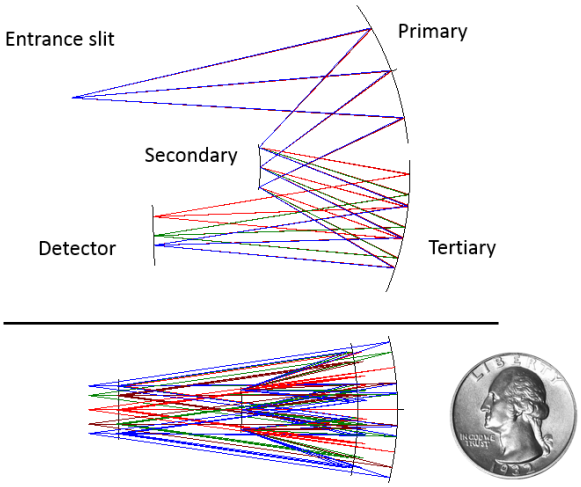

Figure 8.1: Imaging spectrometer raytrace diagram from CODE V software in (top) plane containing chief rays and (bottom) perpendicular plane. US quarter shown as size reference.

Raytrace diagrams of the optical system are shown in Figure 8.1, along with a United States quarter dollar as a size reference for the full system. Figure 8.2 shows the opto-mechanical system design which utilizes a two-piece aluminum housing to which the optics, entrance slit, and detector are mounted externally. The optics and two housing components are attached to each other using precision 3 mm diameter pins for location and M3 socket head cap screws for fastening. This assembly scheme was chosen to maintain specified assembly tolerances of ±25 μm in location, ±170 μrad in tip/tilt, and

±1 mrad in clocking for all components. The primary and tertiary optics were constructed from 50 mm diameter OFHC cylindrical blanks, while the secondary convex grating was manufactured from brass 464. In this design, diamond-turned mounting flanges locate each optic precisely along the system optical axis. To aid in post-manufacturing metrology, a 5.25 mm radius of curvature, 3.2 mm diameter concave spherical fiducial geometry was selected, and 8 fiducials are machined on the mounting flange of each optic. An option is provided to attach the tertiary optic to the housing rigidly using close-fitting pins and screws. However, translation of the tertiary optic was determined to be an effective system defocus compensator, and thus another option was to attach it using loose-fitting pins and utilize a micrometer-driven, flexure-based 2 degree of freedom translator (push-around) to achieve final location. The entire optomechanical assembly is slightly larger than a 75 mm diameter baseball, as shown in the figure inset, and has a system mass of 1100 g with, and 900 g without, the tertiary translator installed. An array of tapped holes on either side of the device allowed mounting to a variety of optical tables and other stock components.

A section view of the designed system is shown in Figure 8.3. The housing was designed to be manufactured by multi-axis milling. The inner form of the housing was designed to produce a tightly-choked beam path which ensures beam clearance but minimizes reflections and effects due to stray light. Due to the relatively loose assembly tolerances made possible by the freeform design, it was acceptable to manufacture the housing on a conventional CNC machining center. Further, conventional machining could be used to produce the primary and tertiary optics to near-net form, requiring use of

UPM only for final machining of the optical surfaces, mounting flanges, and fiducial markings.

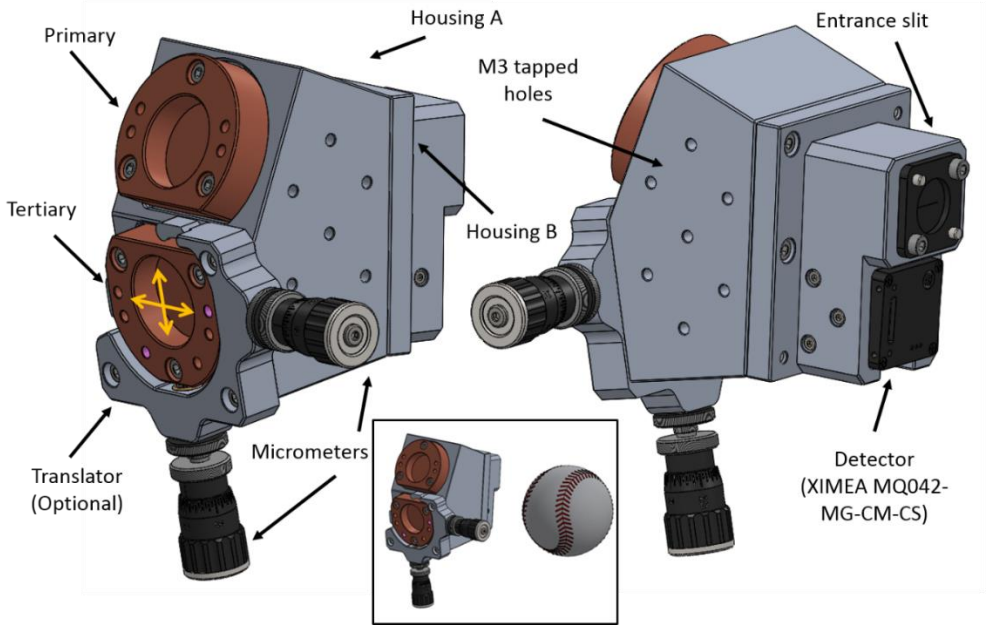

Figure 8.2: Imaging spectrometer optomechanical design. Inset depicts completed assembly with baseball (75 mm diameter sphere) for size reference.

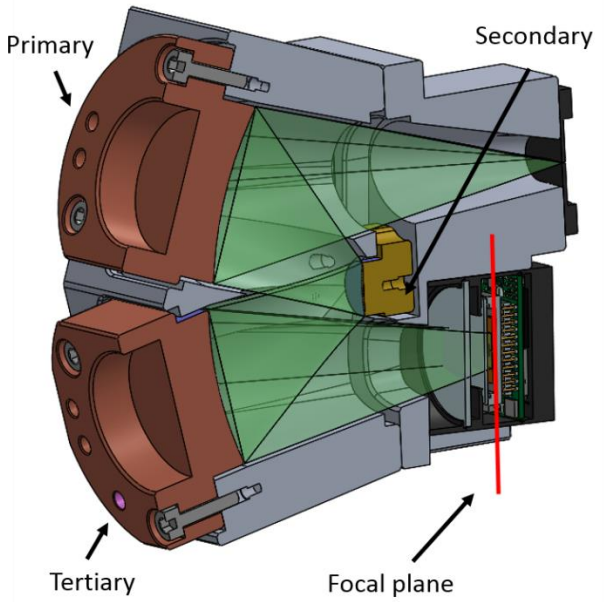

Figure 8.3: Section view of imaging spectrometer assembly.

Form, finish, and assembly tolerances for the optomechanical system are summarized in Table 8.2. All form and finish tolerances specified by the optical designer were intended to be best-effort tolerances on the part of the fabricator.

Table 8.2: Imaging spectrometer system tolerances

Tolerance	Optic	Fiducial
Form	±200 nm P-V	±400 nm P-V
Finish	2 nm Sa	10 nm Sa
Assembly, location	±25 μm	
Assembly, tip/tilt	±170 μrad	
Assembly, clocking	±1000 μrad	

8.2 Manufacture of Freeform Mirrors

Rough machining of the primary and tertiary mirrors from bar stock was performed using a Haas TM1 vertical machining center. Both components were machined to the intended finished size, with a nominal 100 μm of material left on the optical surfaces for finish machining on the Moore Nanotechnology 350FG machine. This process is shown in Figure 8.4. After rough machining, each optic blank was fixed to a brass puck using low temperature wax. It was found in this research that changing the Moore Nanotechnology 350FG from spindle-mode to coordinated axis mode can cause a shift in the workpiece position on the order of 1 micrometer. Thus, the process was designed so that the machine could remain in coordinated axis mode throughout final machining of both parts. In the process, each puck-blank was first mounted on the diamond turning machine, and the mounting flanges turned flat using a 25 μm turning tool. After turning of the mounting flanges, each was removed and placed aside for later

machining of the optical surface, the machine was changed to C-axis mode, and the manufacturing process was continued with tool selection and setup artifact machining. After this change to C-axis mode, any positional shift of the spindle along the Z-axis on the micrometer level would be inconsequential with respect to system assembly tolerances, and any shift along the X-axis was to be mapped using a calibration artifact.

Analyses of the primary and tertiary optical surfaces are presented in Figure 8.5 and Figure 8.6. Because both optics have small (less than 100 μm) departure from a best-fit sphere, they are well-suited for STS manufacturing. In order to ensure correct communication with the optical designer, sag tables and lens prescriptions were requested. The optical designers sag tables were then compared to calculations using the lens prescriptions. Comparison indicated differences of less than 1 nm due only to round-off errors, thus verifying correct interpretation of the prescriptions. The prescriptions were then used to generate the machine code.

Figure 8.4: Primary mirror conventional CNC machining. Clockwise from center: machined component, raw bar stock blank, resulting chips.

Curvature analysis indicated that in order to use a single tool to finish both optics, a maximum tool sweep of 14° and a minimum tool clearance of 0.2° was required. As in

the previous chapter's example, the curvature of the part is rather small allowing a relatively large permissible tool radius of approximately 60 mm. Further examination indicated that the entire optical surface of either component would require cutting on only one side of the tool (in other words, tool sweep angle was positive at all points along the surface).

To comply with these restrictions, a 1.0 mm radius, 0° rake, 10° clearance SCD turning tool from available inventory was selected for finish machining of these optics. Profilometer measurements provided by the manufacturer indicated a peak to valley deviation of less than 25 nm over the range of tool sweep used.

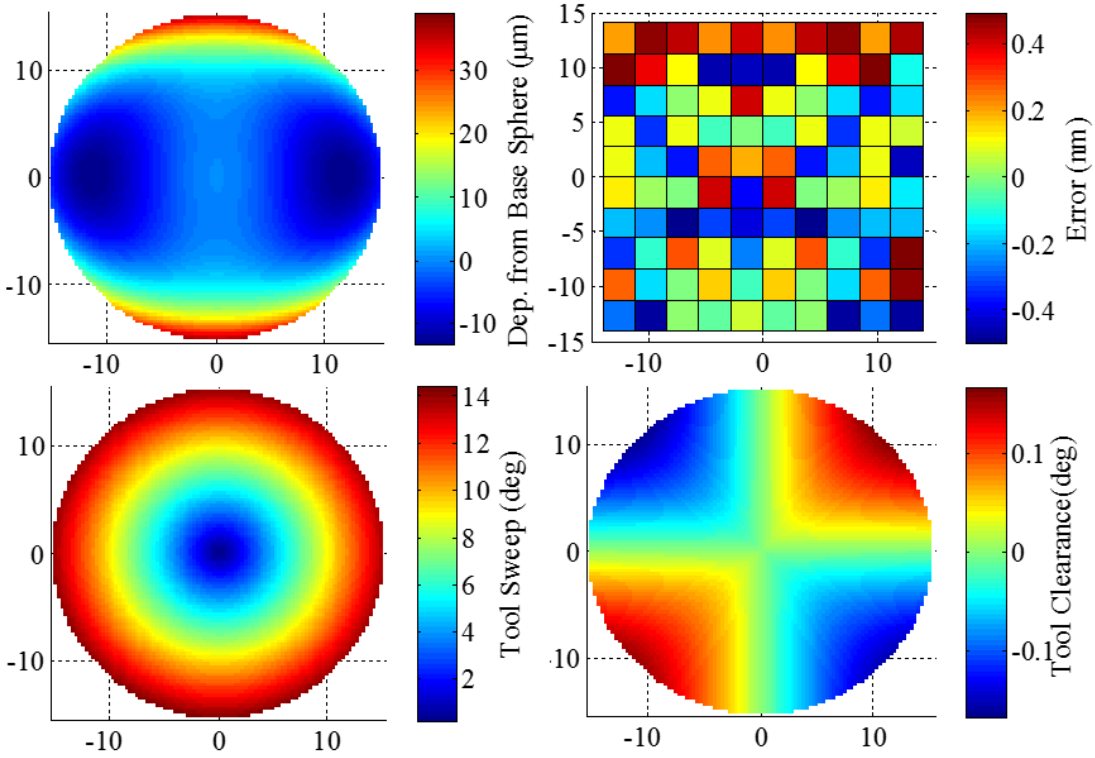

Figure 8.5: Primary mirror surface analysis. Clockwise from top left: Departures from base sphere, validation of sag table, required tool clearance, required tool sweep.

Eq. 6.5 suggested that in the absence of tool waviness and any other unidentified error sources, a maximum 2.3° angular spacing between toolpath points (C-axis

command positions) was required for both optics in order to remain below a theoretical 20 nm form error. Implementing a factor of safety of approximately two, a 1° angular increment was selected. The Moore 350FG machine has a maximum processing speed of 1000 blocks or lines per second. To avoid data overload a conservative program execution speed of 670 lines per second was selected. This execution speed and selected toolpath point spacing produced a nominal spindle rotational rate of approximately 110 rpm, which was suitable considering the low required Z stroke per revolution. Previous face-machining experiments on an OFHC sample from the same material batch as the optical blanks indicated that surface finishes of 1 nm - 2 nm Sa were achievable at 1 μm depth of cut and 2 μm feed per revolution. These parameters were selected for finish machining of the final optics, resulting in a relatively low finish cycle time of approximately 60 minutes. While suitable for prototyping, even lower cycle times would be preferred for higher-volume production, and could be achieved using tooling with larger radius of curvature. To maintain a given surface finish, as determined from Eq. 2.4, permissible feed per revolution, or toolpath stepover, increases with the square root of the tool radius. Thus, the acquisition and use of 10 mm radius tooling would enable a reduction in cycle time to approximately 20 minutes. If machine tool following errors do not become excessive, further reduction of cycle time may also be possible through selection of a larger C-axis spacing between toolpath points, resulting in a faster spindle rotation rate for a given number of program blocks processed per second.

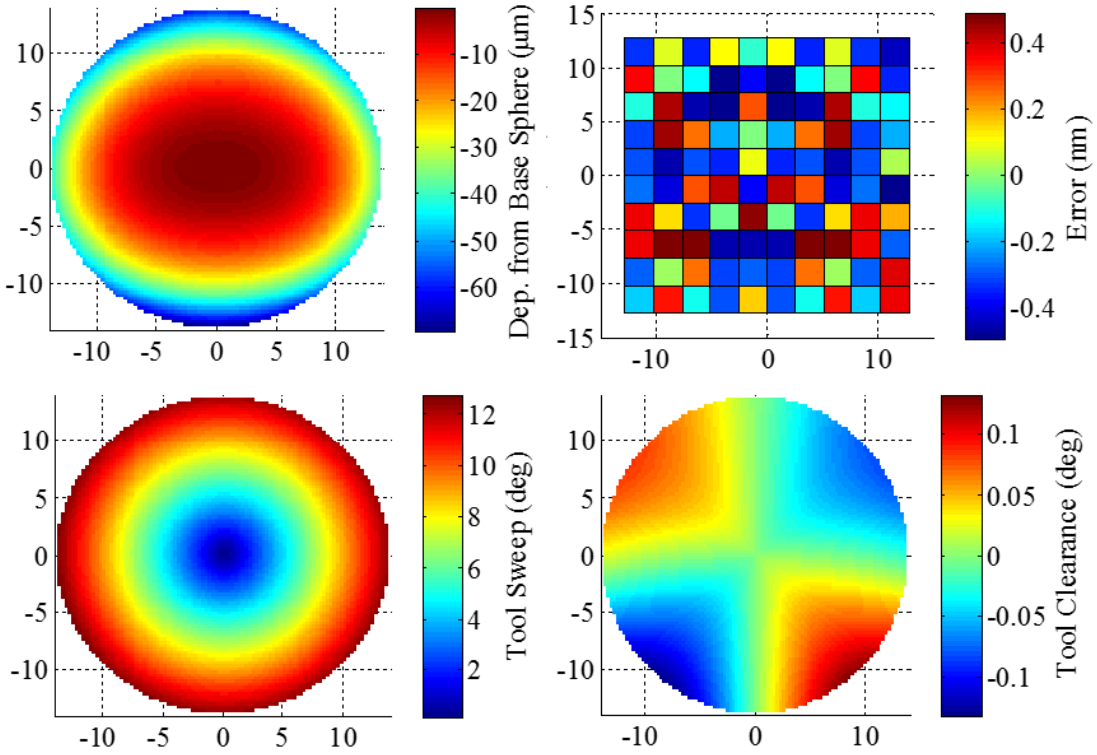

Figure 8.6: Tertiary mirror surface analysis. Clockwise from top left: Departures from base sphere, validation of sag table, required tool clearance, required tool sweep.

To completely map the range of tool sweeps utilized when machining the primary and tertiary optical surfaces, a 12 mm diameter clear aperture, 12 mm radius of curvature concave centered sphere was chosen as an appropriate setup artifact. This artifact maps up to 30° of sweep on a single side of the tool. In order that the spindle error motions might be mapped at a similar speed to that intended for final machining, the artifact was also machined at 670 lines per second with a C-axis point spacing of 1°. As surface finish was not critical for this artifact, a 3 µm depth of cut and feed per revolution was used. The machined artifact was then measured using a Zygo VeriFIRE ATZ Fizeau interferometer. Results are shown in Figure 8.7.

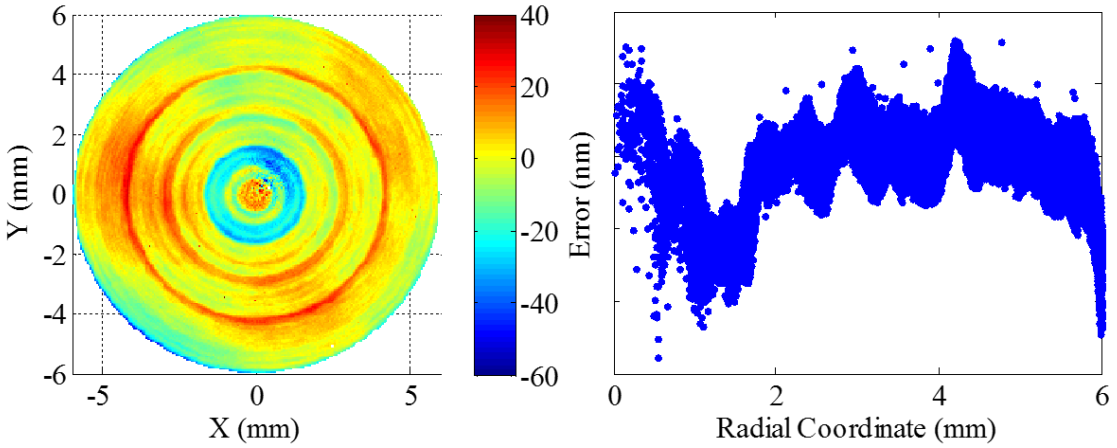

Figure 8.7: STS setup artifact error map (left) and error vs radial coordinate (right).

The measurement of the setup artifact indicated a park to valley form error of 143 nm with an RMS form error of 10.2 nm. Analysis of the error map did not suggest a significant error trend due to tool offset error, however, small fluctuations on order of 25 nm magnitude are evident at radial increments of approximately 2 mm. These were most likely caused by thermal cycling of the machine's main spindle chiller. Plotting the measured error with versus radius also did not show a significant and correctable tool waviness or axis misalignment error. Therefore, no further compensation was performed, and no controller offset corrections were made for this tool.

In a similar manner, a 1.0 mm radius, 0° rake round-nosed, single flute, single crystal diamond milling cutter was selected for machining of the fiducial markings. To map errors on the milling tool, the fiducial geometry itself was used as a setup artifact. In a manner following that described in [47], the artifact was first machined using an inward spiraling toolpath and measured. A 6 μm radial shift (in this case due to error in positioning of the diamond on the milling tool shank, instead of tool offset error) and a residual waviness trend were compensated for, and the artifact was re-machined and measured again. Measurements of the uncompensated and compensated milling tool

artifact are given in Figure 8.8. The peak to valley form error of the artifact was reduced from 760 nm to 213 nm using this approach. Slight residual tool waviness or fluctuations due to thermal cycling of the milling spindle chiller was evident. Nonetheless form error was well within the specified tolerance limits and no further compensation was required.

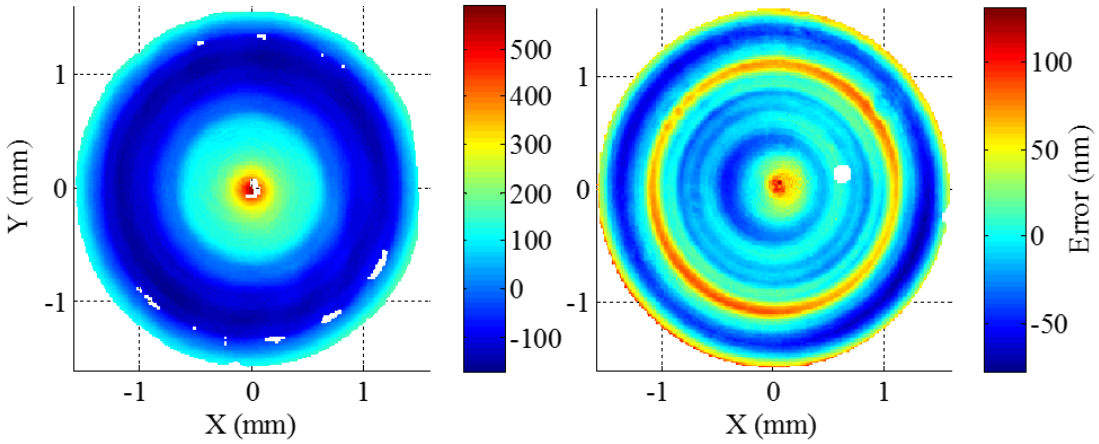

Figure 8.8: Uncompensated (left) and compensated (right) milling tool setup artifacts.

After setup artifact machining, the Moore 350FG machine was left in C-axis mode to complete final machining of the imaging spectrometer optics. For process verification, each toolpath was simulated using the backplotter described previously to verify the machine program. Results are shown in Figure 8.9. These simulations confirmed the validity of the toolpaths, suggesting a most acceptable 1 nm form error component due to toolpath inaccuracy. While effective design communication between designers and manufacturers is often a limiting challenge, the utilized combination of sag table comparison and toolpath backplotting facilitated bipartisan confidence in the process outcomes before manufacturing ensued.

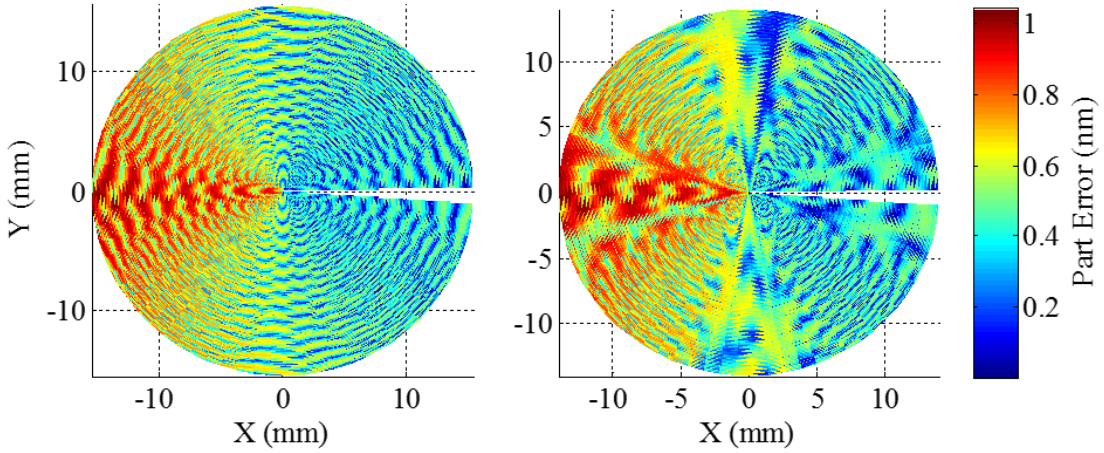

Figure 8.9: Toolpath simulations/backplots for (left) primary and (right) tertiary mirrors.

Further, as an additional monitoring step, for each optic, the base spherical component of each prescription was machined 100 µm above the location of the final optical surface as an in-situ artifact. After measurement of the base spherical component to confirm process stability, the final optical surface was machined using cutting parameters summarized in Table 8.3.

Table 8.3: STS machining parameters

	Roughing	Semi-Finishing	Finishing
Depth of Cut	25 µm	2 µm	1 µm
Stepover	15 µm/rev	2 µm/rev	2 µm/rev
C-Axis Point Spacing	3°	1°	1°
Number of Passes	8	2	1
Cycle Time per Pass	5 min	60 min	60 min
Lubrication	Mist	Mist	Mist

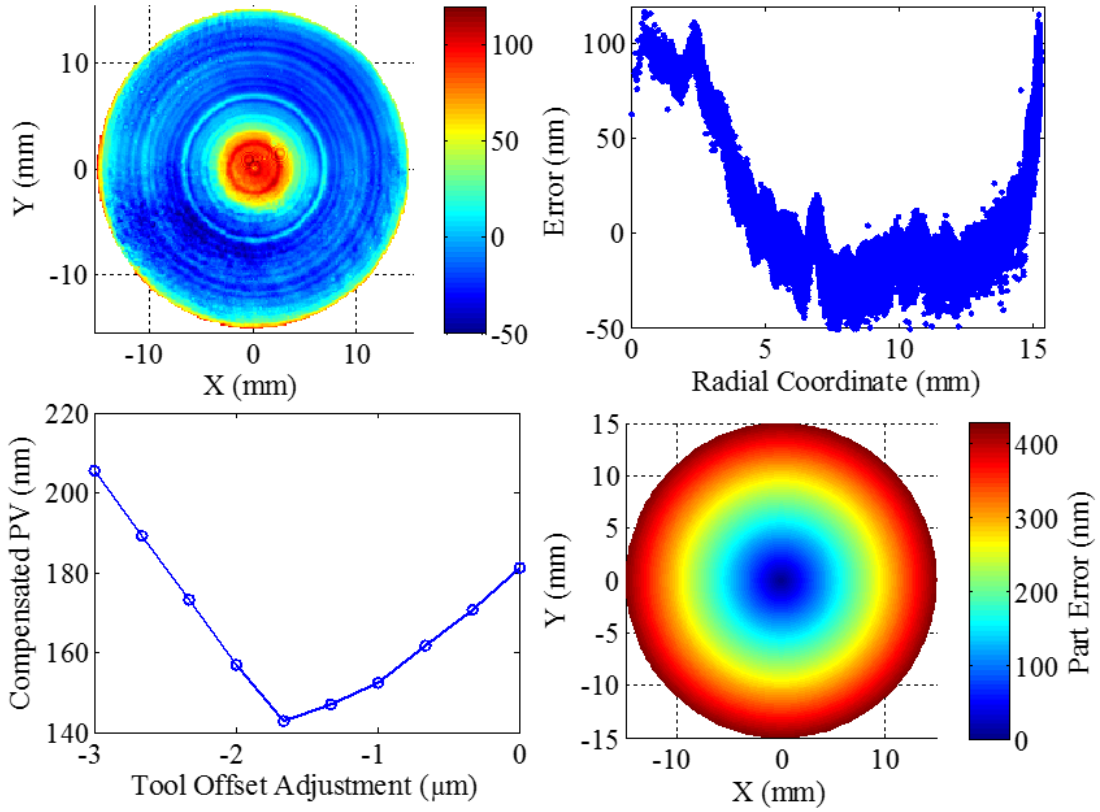

Figure 8.10: Primary mirror base sphere verification. Clockwise from top left: error map as measured, error as a function of radial coordinate, determination of optimum tool offset adjustment, predicted true error due to tool offset error.

Verification of the primary mirror base spherical component is shown in Figure 8.10. No changes were made to tool offsets between final machining of the setup artifact and machining of this base sphere and the machine was left in coordinated axis mode through the process with the same spindle speed. However, an apparent tool offset error was evident in the measurement. Analysis of the measurement suggested that the peak to valley measured error would be minimized if a tool offset adjustment of -1.7 μm was applied. However, the source of this tool offset error remains unknown, as linear axis drift of this magnitude is unlikely.

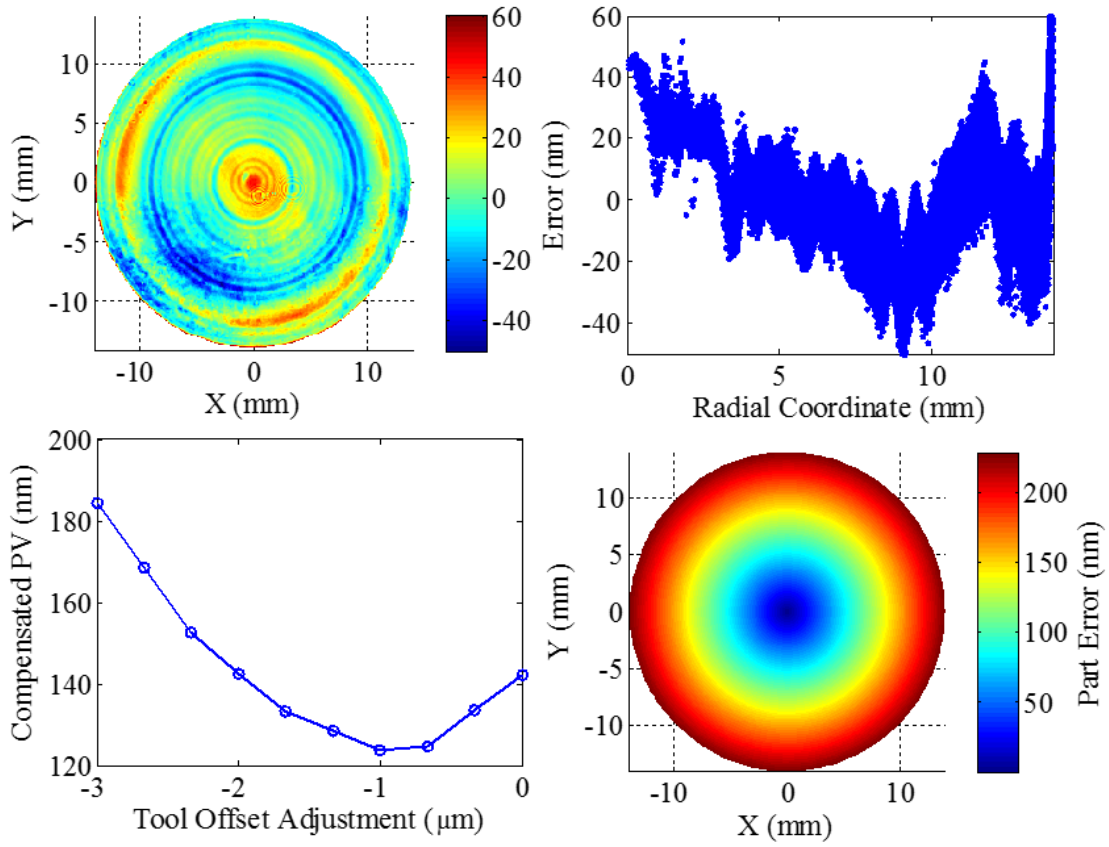

Figure 8.11: Tertiary mirror base sphere verification. Clockwise from top left: error map as measured, error as a function of radial coordinate, determination of optimum tool offset adjustment, predicted true error due to tool offset error.

It was suspected that the spindle shifted slightly on ceasing rotation after machining the setup artifact. It remained stationary during measurement of the artifact and mounting of the part blank and then resumed rotation. As shown in the figure, if this apparent tool offset error was to persist during final optic machining, peak to valley form error on order of 400 nm would result as calculated by Eq. 6.16. While this exceeds the target form tolerance, it would be inappropriate to adjust or compensate for an error component which does not appear repeatable. Therefore, machining of the primary optic continued without tool offset correction or additional toolpath compensation.

After machining of the primary optic, the tertiary blank was mounted, and again the base spherical component of that prescription was machined 100 μm above the intended location of the final optical surface and was measured and analyzed, as presented in Figure 8.11. In this analysis, a suggested tool offset adjustment of -1.0 μm would minimize the peak to valley measurement error. If this apparent tool offset error persisted during machining of the final optical surface, a peak to valley form error of approximately 250 nm would follow from Eq. 6.16. The differing in magnitude of this apparent tool offset error from that of the primary base spherical artifact lends further credibility to the hypothesis that in C-axis mode, the spindle moves slightly each time rotation is ceased and resumed. Again, since this error does not appear repeatable no offset adjustment or additional toolpath compensation was applied, and machining of the tertiary optical surface continued directly. Post-machining discussions led to the hypothesis that even though the spindle appears to move slightly each time rotation is ceased and resumed, that it might gradually return to a singular position over time. Therefore, in future machining efforts, this effect might be remedied by: (1) programming the spindle to rotate in C-axis mode at the desired speed for some stabilization period, perhaps an hour or so, before each error mapping or cutting operation, and (2) by minimizing the amount of time that the spindle sits idle, stopping it only for part mount-dismount cycles and allowing it to remain rotating during off-machine measurement operations.

The final primary and tertiary optics are shown in Figure 8.12. While the exact tool location (and therefore error state, due the previously-mentioned drifting of the C-axis) was not known precisely for each component, it was expected that the components

would be within or only slightly exceed the specified form tolerance, which was acceptable considering the best-effort nature of the tolerances. However, from the process monitoring performed, an ogive-shaped error trend due to tool offset error (caused by spindle drift) was not unexpected.

Figure 8.12: Imaging spectrometer primary (left) and tertiary (right) optics.

8.3 Component Metrology

To evaluate surface finish, SWLI measurements were performed at six locations on each optic using a 50x Mirau-type interferometric objective. Selected measurements are shown in Figure 8.9. The surface texture appeared to be caused by material grain relief. OFHC copper has large grains and cutting along different directions with respect to the grain orientations will cause a change in force and hence slightly different tool deflections and/or elastic recovery in the surface. Thus, the grains of the material can typically be seen in the surface finish. Nonetheless, at all locations sampled, after removing a best fit sphere from the data, an in-tolerance finish of 1-2 nm Sa was measured.

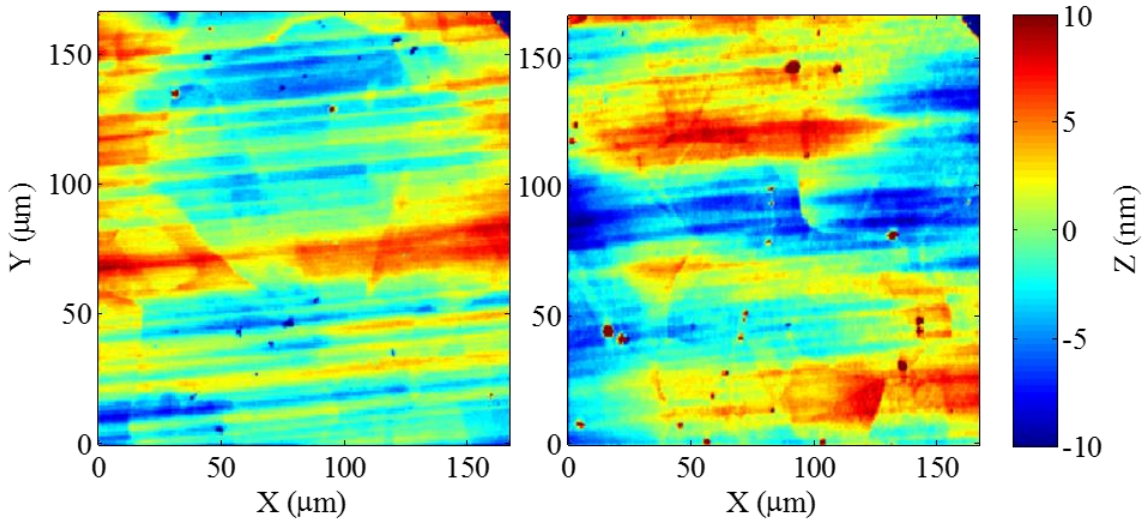

Figure 8.13: SWLI measurements of (left) primary mirror near aperture edge, (right) tertiary mirror near center. 166 μm square FOV.

Initial form verification was performed with the OptiPro UltraSurf 5x, using a white light chromatic confocal probe. For both mirrors, data was acquired at a spacing of 0.1 mm. Due to the diameter of the confocal probe, initial alignment of the primary mirror using the concave spherical fiducials was not possible without causing the probe to collide with the part. After application of a 2x2 Gaussian filter to remove spikes, the data points were aligned to the nominal prescription using the least squares minimization algorithm described in Section 7.3, then form error was determined by subtracting the nominal from the measured form.

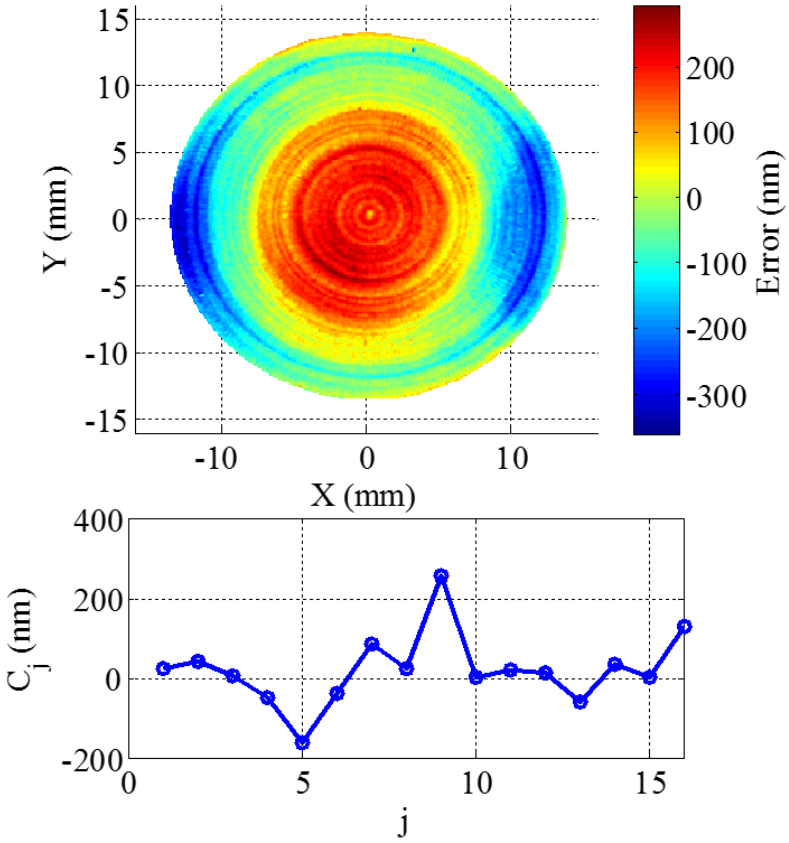

Figure 8.14: UltraSurf (top) form measurement and Zernike polynomial coefficients (bottom) of primary mirror.

The measured form error of the primary mirror is shown in Figure 8.14, indicating a peak to valley error of 655 nm with an RMS value of 133 nm. . As shown, the form error is dominated by Fringe Zernike (see Appendix A.3) terms 5, 9, and 16, corresponding to defocus, cosinusoidal (0° orientation) astigmatism, and spherical aberration. Although exceeding the desired tolerance of 400 nm, freeform optics and metrology are a new research area, so this was considered a successful first best-effort attempt. Further, preliminary analysis indicates that the device will still perform as desired and so functional testing is the proposed next step.

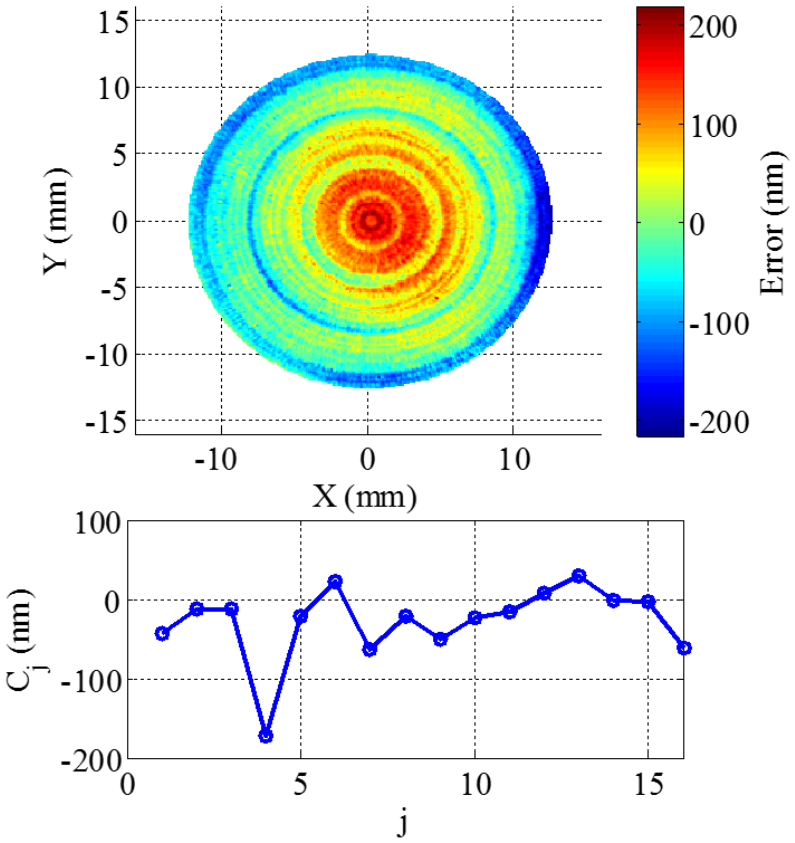

Figure 8.15: UltraSurf (top) form measurement and Zernike polynomial coefficients (bottom) of tertiary mirror.

Similarly, the measured form error of the tertiary mirror is shown in Figure 8.15, evidencing a peak to valley error of 435 nm with an RMS value of 72 nm. The form of this mirror is nearly within the desired tolerance. Errors are dominated by the Fringe Zernike term 4, corresponding to sinusoidal (45° orientation) astigmatism.

While defocus and spherical aberration error terms were expected on these components as results of the manufacturing process, due to tool offset error and tool radius deviation, the presence of astigmatism was not expected, and may be indicative of distortion during machining due to the mounting technique (wax attachment to a brass puck) used. Since both mirrors were machined from nearly identically sized blanks,

further credibility is lent to this hypothesis by the similar magnitudes of astigmatic error on both components.

However, since the uncertainty in the measurement equipment is not completely understood, further independent metrology is necessary to confirm the magnitude and shape of the form errors before attempting to isolate and compensate for process-related sources.

8.4 System Assembly

The assembled imaging spectrometer is shown in Figure 8.16. Following assembly and procurement of the detector, system performance testing is to commence at the University of Rochester.

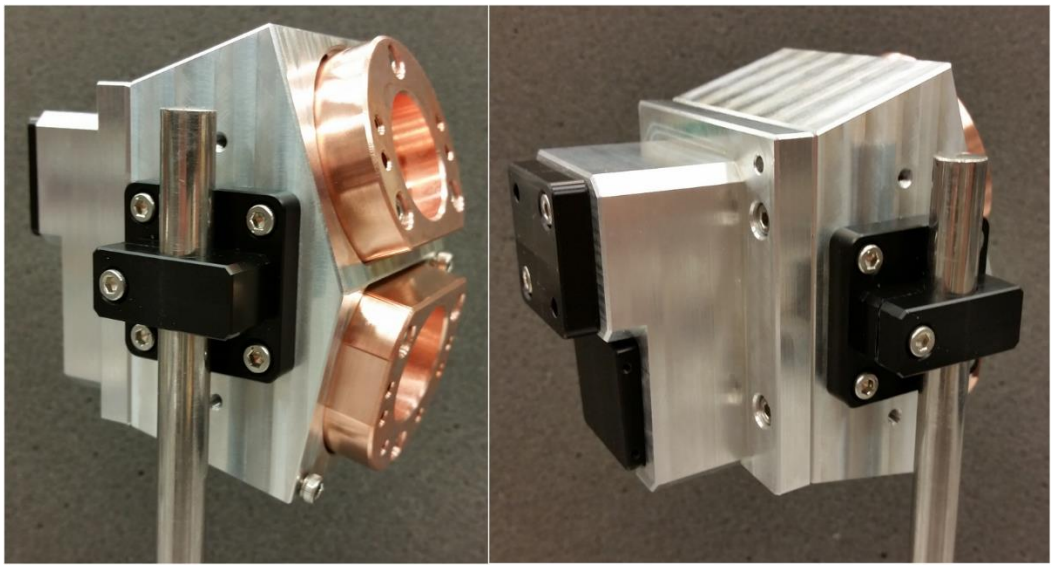

Figure 8.16: Two views of completed and assembled imaging spectrometer.

CHAPTER 9: SUMMARY OF FINDINGS AND FUTURE WORK

9.1 Diamond Machining of IRG 26

During the orthogonal turning of IRG 26 ($As_{40}Se_{60}$) chalcogenide, a transition from a ductile-dominated, plastic deformation dominated cutting mechanism to a brittle-dominated, fracture-driven mechanism was apparent when uncut chip thickness exceeded a critical value of approximately 600 nm. The results obtained were similar in form to those previously reported in [47], however the transition occurred at a lower chip thickness in this work, likely due to variation between material batches and/or differences in tool cutting edges. No evidence of thermal softening at high cutting speeds was apparent, and the critical chip thickness did not change significantly with cutting speed. Further, side cutting edge angle was also found to have negligible effect on cutting behavior. Consistent with expectation and [37], negative-rake tooling was found to suppress brittle fracture and allow ductile-dominated machining at higher feed rates than possible with zero-rake tooling, as evidenced by force measurement and metrology of machined surfaces. Under appropriate cutting conditions, slightly positive rake angles were also found to produce optical quality surfaces. Flycutting experiments designed to produce a wide range of interaction times from 88 μs to several ms evidenced no effect of interaction time on force magnitude or critical chip thickness. Orthogonal turning data was utilized to predict process forces during round nosed turning operations as well as square and round nosed milling, and yielded acceptable agreement with experimental

results. However, during round nosed turning operations, the transition from ductile-dominated to brittle-dominated cutting regimes occurred at a higher uncut chip thickness than predicted by the developed mechanistic cutting model. While this may have been due to tool edge condition (it may be true that round-nosed tools typically have a larger edge radius than pointed or square tools, simply due to the tool manufacturing process), it could also be indicative of additional cutting mechanics complexity in regions of slowly-varying chip thickness. Additional work is suggested to isolate the cause of this effect in round nosed (turning and milling) operations, as well as to investigate the batch homogeneity of this material. Further, IRG 26 is only one of a series of similar AsGeSe IR glasses of which the cutting mechanics are largely uncharacterized.

9.2 Diamond Machining of Germanium

Operator experience holds that germanium is more readily diamond milled than diamond turned to produce a fracture-free surface of optical quality, suggesting a change in cutting mechanics at short timescales. During round-nosed turning and flycutting of monocrystalline <1,1,1> germanium using -25° rake tooling, a sharp, clearly marked drop in process forces in the style of that observed during chalcogenide glass machining was not observed. For both machining processes, which had identical cutting geometries and differed only in the steady or interrupted nature of the cut, general agreement was observed between experimentally measured process forces and predicted values using previously documented orthogonal machining data. Further characterization of machined specimens using SWLI and Raman spectroscopy indicated a monotonic increase of surface roughness, surface pitting, residual compressive stress, and subsurface damage and lattice disorder with increasing feed rate (and therefore increasing chip thickness).

No noticeable difference in surface or subsurface condition or process force behavior was observed between flycut and diamond turned specimens. However, the flycutting experiments performed in this initial work produced tool-workpiece interaction times of on order of several ms, which is a much longer timescale than encountered during typical milling operations. Due to the semiconducting nature of germanium, it is proposed that the material could exhibit a transition to a metallic phase under certain cutting conditions, which could be investigated by modifying existing experimental apparatus to allow in situ measurements of specimen conductivity or resistivity. Although custom tooling would be required to proceed in the manner demonstrated in chalcogenide glass, further work is necessary to examine the cutting mechanics of germanium under much shorter contact times and fully investigate the existence of a timescale dependence.

9.3 Slow-Tool-Servo Ultraprecision Machining

Conventional CAM packages are incapable of accurately representing complex optical surfaces, and also are unable to compensate for microscale error sources such as tool waviness and machine axis misalignment which are negligible at the macroscale. A pre-process artifact-based methodology for mapping of tool waviness and offset errors, as well as machine axis errors was presented, and utilized in conjunction with an optical surface equation-driven analytical toolpath generation strategy for manufacturing of a transmissive chalcogenide glass high order freeform lens pair, and two reflective freeform mirrors for an imaging spectrometer. A combination of sag table comparison and toolpath backplotting facilitated streamlined communication between optical designers and fabricators, allowing complete confidence in process outcomes prior to the start of machining. The validity of the toolpath generation strategy was demonstrated

post-process component metrology and testing. Functional testing of the chalcogenide freeform lens pair demonstrated desired performance, although form errors as indicated by both optical CMM and stitching SWLI were higher than predicted by the tilted flat setup artifact. Similarly, the form errors of the freeform mirror pair for the imaging spectrometer were larger than predicted by the concave sphere setup artifact, yet were of an order which suggested that satisfactory system performance will be obtainable. For both sets of components, measured form errors were higher than expected and could not be correlated to tool-based sources which would have been evident on the setup artifact. To improve the quality of subsequent optics, further investigation is necessary to determine the source of these errors, which could be due to mounting distortions, more complex machine dynamic effects during freeform manufacturing, or other undetermined sources.

REFERENCES

[1] J. Anderson and R. Porter, "Ronchi's method of optical testing," *Astrophysical Journal,* vol. 70, pp. 175-181, 1929.

[2] D. Harbour and W. e. Welker, Understanding Foucault: A primer for beginners, Netzari, 2008.

[3] K. Thompson and J. Rolland, "Freeform optics: A revolution in imaging system design," *Optics and Photonics News,* vol. 23, no. 6, pp. 30-35, 2012.

[4] F. Fang, X. Zhang, A. Weckenmann, G. Zhang and C. Evans, "Manufacturing and measurement of freeform optics," *CIRP Annals - Manufacturing Technology,* vol. 62, pp. 832-846, 2013.

[5] L. Alvarez, "Two-element variable-power spherical lens". United States of America Patent 3,305,294, 1967.

[6] M. Schinker and W. Döll, "Turning of optical glasses at room temperature," *Proc. SPIE: In-Process Optical Metrology for Precision Machining,* vol. 402, pp. 70-80, 1987.

[7] T. Bifano, T. Dow and R. Scattergood, "Ductile-regime grinding: a new technology for machining brittle materials," *J. Engineering for Industry,* vol. 113, no. 1, pp. 184-189, 1991.

[8] Z. Pei, S. Billingsliey and S. Miura, "Grinding induced subsurface cracks in silicon wafers," *Int. J. Machine Tools and Manufacture,* vol. 39, pp. 1103-1116, 1999.

[9] Z. Pei, G. Fisher and J. Liu, "Grinding of silicon wafers: a review from historical perspectives," *Int. J. Machine Tools and Manufacture,* vol. 48, pp. 1297-1307, 2008.

[10] A. Haapalinna, S. Nevas and D. Pähler, "Rotational grinding of silicon wafers - sub-surface damage inspection," *Materials Science and Engineering B,* vol. B107, pp. 321-331, 2004.

[11] K. Puttick, M. Rudman, K. Smith, A. Franks and K. Lindsey, "Single-point diamond machining of glass," *J. Roy. Soc. London A,* vol. 426, pp. 19-30, 1989.

[12] R. Brehm, K. van Dun, J. Teunissen and J. Haisma, "Transparent single-point turning of optical glass: a phenomenological presentation," *Precision Engineering,* pp. 207-213, 1979.

[13] T. Nakasuji, S. Kodera, S. Hara and H. Matsunaga, "Diamond turning of brittle materials for optical components," *Annals of CIRP*, vol. 39, no. 1, pp. 89-92, 1990.

[14] T. Moriwaki, E. Shamoto and K. Inoue, "Ultraprecision ductile cutting of glass by applying ultrasonic vibration," *Annals of CIRP*, vol. 41, no. 1, pp. 141-144, 1992.

[15] O. Ogura and Y. Okizaki, "Ductile-regime turning of brittle materials by single point diamond," in *ASPE 15th Annual Meeting*, Scottsdale, AZ, 2000.

[16] F. Fang, X. Liu and L. Lee, "Micro-machining of optical glasses - a review of diamond-cutting glasses," *Sadhana*, vol. 28, no. 5, pp. 945-955, 2003.

[17] P. Blake and R. Scattergood, "Ductile-regime machining of germanium and silicon," *J. Am. Ceram. Soc.*, vol. 73, no. 4, pp. 949-957, 1990.

[18] J. Drescher and T. Dow, "Tool force model development for diamond turning," *Precision Engineering*, vol. 12, no. 1, pp. 29-35, 1990.

[19] J. Giovanola and I. Finnie, "On the machining of glass," *J. Materials Science*, vol. 15, no. 1, pp. 2508-2514, 1980.

[20] D. Ravindra and J. Patten, "Ductile regime single point diamond turning of quartz resulting in an improved and damage-free surface," *Machining Science and Technology*, vol. 15, pp. 357-375, 2011.

[21] J. Yan, K. Maekawa, J. Tamaki and A. Kubo, "Experimental study on the ultraprecision ductile machinability of single-crystal germanium," *JSME Int. J. C*, vol. 47, no. 1, pp. 29-36, 2004.

[22] P. Pawase, P. Brahmankar, P. R. and R. Balasubramanium, "Analysis of machining mechanism in diamond turning of germanium lenses," *Procedia Materials Science*, vol. 5, pp. 2363-2368, 2014.

[23] J. Bryan, "System and method for forming a non-rotationally symmetric portion of a workpiece". United States Patent US7089835 B2, 2 July 2003.

[24] M. Arif, M. Rahman and W. Yoke San, "Analytical model to determine the critical feed per edge for ductile-brittle transition in milling process of brittle materials," *International Journal of Machine Tools and Manufacture*, vol. 51, no. 1, pp. 180-181, 2011.

[25] T. Matsumura, T. Hiramatsu and T. Shirakashi, "A study on cutting force in the milling process of glass," *Journal of Manufacturing Processes*, vol. 7, no. 2, pp. 102-108, 2005.

[26] B. Dutterer, J. Lineberger, P. Smilie, D. Hildebrand, T. Harriman, M. Davies, T. Suleski and D. Lucca, "Diamond milling of an Alvarez lens in germanium," *Precision Engineering,* vol. 38, pp. 398-408, 2014.

[27] P. Smilie, B. Dutterer, J. Lineberger, M. Davies and T. Suleski, "Freeform micromachining of an infrared Alvarez lens," *Proc. SPIE* , vol. 7927, no. 79270K, 2011.

[28] T. Rusnaldy and H. Kim, "Micro-end-milling of single-crystal silicon," *Int. J. Machine Tools and Manufacture,* vol. 47, pp. 2111-2119, 2007.

[29] W. Chiu, W. Endres and M. Thouless, "An experimental study of orthogonal machining of glass," *Machining Science and Technology,* vol. 4, no. 2, pp. 253-275, 2000.

[30] B. Lawn and M. Swain, "Microfracture beneath point indentations in brittle solids," *Journal of Materials Science,* vol. 10, pp. 113-122, 1975.

[31] B. Lawn and A. Evans, "A model for crack initiation in elastic/plastic indentation fields," *J. Materials Sci.,* vol. 12, no. 1, pp. 2195-2199, 1977.

[32] D. Marshall, B. Lawn and A. Evans, "Elastic/plastic indentation damage in ceramics: the lateral crack system," *J. Am. Ceramic. Soc.,* vol. 65, no. 11, pp. 561-566, 1982.

[33] B. Lawn, A. Evans and D. Marshall, "Elastic/plastic indentation damage in ceramics: the median/radial crack system," *J. Am. Ceramic Soc.,* vol. 63, no. 10, pp. 574-581, 1980.

[34] B. Lawn and R. Wilshaw, "Indentation fracture: principles and applications," *J. Materials Sci,* vol. 10, no. 1, pp. 1049-1081, 1975.

[35] E. Le Bourhis and T. Rouxel, "Indentation response of glass with temperature," *Journal of Non-crystalline solids,* vol. 316, no. 1, pp. 153-159, 2003.

[36] E. Le Bourhis, P. Gadaud, J. Guin, N. Tournerie, X. Zhang, J. Lucas and T. Rouxel, "Temperature dependence of the mechanical behaviour of a GeAsSe glass," *Scripta Materiala,* vol. 45, no. 1, pp. 317-323, 2001.

[37] P. Bridgman and I. Simon, "Effects of very high pressures on glass," *J. Applied Physics,* vol. 24, no. 4, pp. 405-413, 1953.

[38] G. Sheldon and I. Finnie, "The mechanism of material removal in the erosive cutting of brittle materials," *J. Engineering for Industry,* vol. 88, no. 4, pp. 393-399, 1966.

[39] W. Blackley and R. Scattergood, "Ductile-regime machining model for diamond turning of brittle materials," *Precision Engineering,* vol. 13, no. 2, pp. 95-103, 1991.

[40] D. Lucca, P. Chou and H. R., "Effect of tool edge geometry on the nanometric cutting of ge," *Annals of CIRP,* vol. 47, no. 1, pp. 475-478, 1997.

[41] E. Brinksmeier, W. R. Preuss, O. Riemer and R. Rentsch, "Ultraprecision high speed cutting," in *30th ASPE Annual Meeting*, Austin, TX, 2015.

[42] W. Blackley and R. Scattergood, "Chip topography for ductile-regime machining of germanium," *J. Engineering for Industry*, vol. 116, pp. 263-266, 1994.

[43] J. Troutman, J. Owen, M. Davies and T. Schmitz, "Cutting force measurement during diamond flycutting of chalcogenide glass," in *30th ASPE Annual Meeting*, Austin, TX, 2015.

[44] M. Merchant, "Mechanics of the metal cutting process I: orthgonal cutting and a type 2 chip," *J. Applied Physics,* vol. 16, pp. 267-275, 1945.

[45] M. Merchant, "Mechanics of the metal cutting process II: plasticity conditions in orthogonal cutting," *J. Applied Physics,* vol. 16, pp. 318-324, 1945.

[46] A. Markopoulos, "Ch. 2: Cutting mechanics and analytial modeling," in *Finte Element Method in Machining Processes*, New York, Springer, 2013, pp. 11-27.

[47] J. Owen, *"Manufacture of infrared optics in brittle materials". Ph.D. dissertation, UNC Charlotte, Charlotte, NC, 2015.*.

[48] T. Schmitz and K. Smith, Machining Dynamics: Frequency Response to Improved Productivity, New York: Springer, 2009.

[49] G. Tlusty, Manufacturing Equipment and Processes, Upper Saddle River, NJ: Prentice-Hall, 2000.

[50] J. Owen, M. Davies, D. Schmidt and E. Urruti, "On the ultra-precision diamond machining of chalcogenide glass," *CIRP Annals - Manufacturing Technology,* vol. 64, pp. 113-116, 2015.

[51] L. Kumanchik and T. Schmitz, "Improved analytical chip thickness model for milling," *Precision Engineering,* vol. 31, no. 1, pp. 317-324, 2007.

[52] E. Fess, F. Wolfs, S. DeFisher and J. Ross, "Acylinder and Freeform Optical Manufacturing," in *SPIE Optifab,* Rochester, NY, USA, 2015.

[53] M. Fox, Optical Properties of Solids, New York: Oxford University Press, 2012.

[54] Manufacturing Laboratories, Inc., "MetalMAX: The complete package for machine tool dynamic characterization," [Online]. Available: http://www.mfg-labs.com/live/?page_id=211.

[55] Schott AG, "Infrared Chalcogenide Glass IRG 26," 17 October 2013. [Online]. Available: http://www.schott.com/advanced_optics/english/download/schott-infrared-chalcogenide-glasses-irg26-october-2013-eng.pdf. [Accessed 29 September 2015].

[56] R. Rhorer and C. Evans, "Fabrication of Optics by Diamond Turning," in *Handbook of Optics: Vol II*, Columbus, McGraw-Hill, 2010, pp. 41.1-41.13.

[57] C. Syn and J. Taylor, "Ductile-brittle transition of cutting mode in diamond turning of single crystal silicon and glass," in *ASPE/IPES Poster Session*, Monterey, 1989.

[58] S. Ozturk and E. Altan, "Slip-line metal cutting model with negative rake angle," *J. Braz. Soc. Mech. Sci. & Eng.*, vol. 34, no. 3, pp. 246-252, 2012.

[59] A. Sohn, "Rake angle variation in diamond turning," in *22nd ASPE Annual Meeting*, Dallas, TX, 2007.

[60] J. Troutman, J. Owen, A. Zare, T. Harriman, D. Lucca and M. Davies, "Cutting mechanics and subsurface integrity in diamond machining of chalcogenide glass," in *3rd CIRP Conference on Surface Integrity*, Charlotte, 2016.

[61] M. Rubeo and T. Schmitz, "Time domain modeling of compliant workpiece milling," in *30th ASPE Annual Meeting*, Austin, TX, 2015.

[62] E. Korkmaz, B. Gozen, B. Bediz and O. Ozdoganlar, "High-frequency compensation of dynamic distortions in micromachining force measurements," *Procedia Manufacturing*, vol. 1, no. 1, pp. 534-545, 2015.

[63] J. Owen, J. Troutman, T. Harriman, S. Shojaee, A. Zare, D. Lucca and M. Davies, "The mechanics of freeform milling of germanium for IR applications," *CIRP Annals Manufacturing Technology*, 2016.

[64] Y. Tohme and J. Lowe, "Machining of Freeform Optical Surfaces by Slow Slide Servo Method," in *18th ASPE Annual Meeting*, Portland, OR, 2003.

[65] Y. Tohme and J. Lowe, "Machining of freeform optical surfaces by slow slide servo method," 2005. [Online]. Available: http://www.nanotechsys.com/wp-

content/uploads/file/PDFs/MachiningOfFreeformOptical.PDF. [Accessed 16 November 2015].

[66] X. Wang, X. Fu, C. Li and M. Kang, "Tool path generation for slow tool servo turning of complex optical surfaces," *The International Journal of Advanced Manufacturing Technology,* vol. 79, no. 1, pp. 437-448, 2015.

[67] C. Chen, Y. Cheng, W. Hsu, H. Chou, P. Wang and D. Tsai, "Slow tool servo diamond turning of optical freeform surface for astigmatic contact lens," in *SPIE 8126, Optical Manufacturing and Testing IX*, 2011.

[68] J. Troutman, D. Barnhardt, J. Shultz, J. Owen, S. DeFisher, M. Davies and T. Suleski, "Machining and metrology of a chalcogenide glass freeform lens pair," *Procedia Manufacturing,* 2016.

[69] L. Alvarez and W. Humphrey, "Variable-power lens and system". United States of America Patent US3507565 A, 21 April 1970.

[70] M. Chrisp, "Convex diffraction grating imaging spectrometer". United States of America Patent 5,880,834, 9 March 1999.

[71] A. Offner, "Unit power imaging catoptric anastigmat". United States of America Patent 3,748,015, 24 July 1973.

[72] L. Cook and J. Silny, "Imaging spectrometer trade studies: a detailed comparision of the Offner-Chrisp and reflective triplet optical design forms," in *SPIE Remote Sensing System Engineering III*, San Diego, 2010.

[73] J. Reimers, E. Schiesser, K. Thompson, K. Whiteaker, D. Yates and J. Rolland, "Comparson of freeform imaging spectrometer design forms using spectral full field displays," in *OSA Imaging and Applied Optics*, Arlington, VA, 2015.

APPENDIX A: OPTICAL PRESCRIPTIONS

A.1 Freeform Variable-Focus Lens Pair Prescription

The freeform variable focus lens pair described in Chapter 7 has a surface prescription given in Cartesian coordinates as follows:

$$z(x,y) = \sum_{k=1}^{n} \frac{1}{2} a_{2,k}(x^2+y^2)^k + \sum_{k=1}^{n} b_{2,k} \int (x^2+y^2)^k dx + c_0 x$$

The two high order freeform lenses have identical prescriptions with the following coefficients and constants:

k	$\mathbf{a_{2,k}}$	$\mathbf{b_{2,k}}$	$\mathbf{c_k}$
0			0.0262
1	-3.62E-03	-1.01E-03	
2	8.50E-08	9.45E-08	
3	-4.00E-12	-1.78E-11	
4	2.88E-16	4.39E-15	
5	-1.61E-18	-7.61E-18	
6	2.31E-20	9.49E-20	
7	-1.31E-22	-5.34E-22	

Before analyzing and machining these components using the methodology described in Chapter 6, the given surface prescriptions required conversion to the more appropriate right cylindrical coordinate system, using the familiar transformation:

$$\begin{Bmatrix} \rho \\ \phi \\ z \end{Bmatrix} = \begin{Bmatrix} \sqrt{(x^2+y^2)} \\ \text{atan}(y/x\,) \\ z \end{Bmatrix}$$

A.2 Imaging Spectrometer Surface Prescriptions

The compact freeform imaging spectrometer described in Chapter 8 makes use of primary and tertiary mirrors which are described in right cylindrical coordinates using the following equation:

$$z(\rho,\phi) = \frac{c\rho^2}{1+\sqrt{1-(1+\kappa)c^2\rho^2}} + \sum_{j=1}^{21} C_j Z_j$$

In this equation,

c = curvature of surface, $c = 1/R_{curv}$

κ = conic constant

C_j = amplitude coefficient for the j_{th} fringe Zernike polynomial function

Z_j = j_{th} fringe Zernike polynomial function $Z(\rho,\ \phi),\ R = \rho/R_{norm}$

The prescriptions for both mirrors are proprietary; therefore, only approximate values are given as follows:

Term	**Primary**	**Tertiary**
$\boldsymbol{\kappa}$	-1.50	1.25
$\mathbf{R_{curv}}$	-61.5	-62.5
$\mathbf{R_{norm}}$	15.4	14.0
$\mathbf{C_j}$	-0.02<$\mathbf{C_j}$<0.02	-0.02< $\mathbf{C_j}$ <0.02

A.3 Table of Fringe Zernike Polynomials

The first 25 Zernike polynomials from the fringe ordering, as used in the lens prescriptions in Appendix A.2 are given as follows in right-handed cylindrical coordinates $Z_j(R = {\rho}/{R_{norm}}, \phi)$:

Z_1	1
Z_2	$R\cos(\phi)$
Z_3	$R\sin(\phi)$
Z_4	$2R^2 - 1$
Z_5	$R^2\cos(2\phi)$
Z_6	$R^2\sin(2\phi)$
Z_7	$(3R^2 - 2R)\cos(\phi)$
Z_8	$(3R^2 - 2R)\sin(\phi)$
Z_9	$6R^4 - 6R^2 + 1$
Z_{10}	$R^3\cos(3\phi)$
Z_{11}	$R^3\sin(3\phi)$
Z_{12}	$(4R^3 - 3R^2)\cos(2\phi)$
Z_{13}	$(4R^3 - 3R^2)\sin(2\phi)$
Z_{14}	$(10R^5 - 12R^3 + 3R)\cos(\phi)$
Z_{15}	$(10R^5 - 12R^3 + 3R)\sin(\phi)$
Z_{16}	$20R^6 - 30R^4 + 12R^4 - 1$
Z_{17}	$R^4\cos(4\phi)$
Z_{18}	$R^4\sin(4\phi)$
Z_{19}	$(5R^5 - 4R^3)\cos(3\phi)$
Z_{20}	$(5R^5 - 4R^3)\sin(3\phi)$
Z_{21}	$(15R^6 - 20R^4 + 6R^2)\cos(2\phi)$
Z_{22}	$(15R^6 - 20R^4 + 6R^2)\sin(2\phi)$
Z_{23}	$(35R^7 - 60R^5 + 30R^3 - 4R)\cos(\phi)$
Z_{24}	$(35R^7 - 60R^5 + 30R^3 - 4R)\sin(\phi)$
Z_{25}	$70R^8 - 140R^6 + 90R^4 - 20R^2 + 1$

APPENDIX B: MATLAB CODES

B.1 STS Toolpath Generator

```
% caxturn_zerorake_circtool_tpgen
%
% generates toolpath for a coordinated C-X-Z turning process
%   - only for tools of constant radius
%   - only for zero-rake tools
%
% outputs nc code for the nanotech 350FG
%   - outputs a list of coordinates for machining in G93
%   - spindle can rotate in either direction
%   - naming convention from 350FG operator manual
%       - 'ccw' (M04) rotates ccw looking at spindle face along -Z dir
%           - c goes from 0 -> -2pi
%       - 'cw'  (M03) rotates cw looking at spindle face along -Z dir
%           - c goes from 0 -> +2pi (usual way)
%   - all inputs, outputs are in units of mm, mm/min, or min/mm
%
% works in constant angular spacing mode if 'angle' is switched
% works in constant chord spacing mode if 'chord' is switched
%     - reverts to constant angle spacing when the radius becomes small
%       enough to require an angular increment greater than dpmax
%
%
% machine and tool coordinate system
% z = 0 at final part top face
%
% requires the structure 'part', pertaining to the part to be cut, to
% already be defined through some other script. part contains the
% following important variables and function at minimum:
%   - z_f is function for the surface equation z(phi, rho)
%       - defines part surface in right cylindrical coordinates
%   - dz_dr_f is function for surface partial derivative dz/drho
%   - diameter is the part max diameter
%
% works with 4xN matrices where row 1 is C, row 2 is X, row3 is Y, row
4 is Z.
% adds the ability later to have y-axis moves
%
% John R. Troutman
% 12-23-2015

%%%%%%%%%%%%%%%%%%%%%%%%% USER INPUTS %%%%%%%%%%%%%%%%%%%%%%%%%%%%%%%%

% cutting parameters
cut.dir = 'cw';         % spindle rotation direction
cut.type = 'angle';     % constant 'angle' or constant 'chord' spacing
cut.stepover = 0.05;        % stepover per rev (mm)
cut.chord = 0.01;           % chord length on toolpath spiral between
points
cut.dpmax = deg2rad(2);     % max angular increment (rad) between points
```

```
cut.leadin = 0.25;          % how far to extend toolpath past part max R

% tool parameters
tool.roc = 1.5;                 % tool nose radius (mm)

% tool waviness: polynomial coefficients
% tool radius deviation (+ outward) as function of tool sweep (theta)
% theta (degrees) measured +ve clockwise from tool tip as viewed from
above
tool.wav_coeff = [-3e-7 +1e-5 +2e-5 0];    % mm/deg^n
cut.sw_twc = 1;                             % perform TWC if == 1

% machine error components
% dxz: angular misalignment of x, z axes
% positive if greater than 90 deg between axes
mach.dxz =  -0.02;           % dxz (degrees)
cut.sw_conecomp = 1;         % comp for cone error if == 1

% output
out.plot = 0;       % plot toolpath stuff
out.negz = 0;       % make all z-values negative (shift down) if == 1

out.write = 0;       % actually write file if = 1
out.maxlines = 4e6;  % max num of lines in one file

%%%%%%%%%%%%%%%%%%%%%%%%%%%%%%%%%%%%%%%%%%%%%%%%%%%%%%%%%%%%%%%%%%%%%%%%%%%

%% load the structure 'part'
partfilename = uigetfile('*.mat', 'Select saved .MAT file.');
load(partfilename);

%% constant which handles spindle direction
if strcmp(cut.dir, 'ccw') == 1
    cut.dirsw = -1;
elseif strcmp(cut.dir, 'cw') == 1
    cut.dirsw = 1;
end

%% build the base toolpath spiral across the part
cut.xstart = (part.diameter/2) + cut.leadin;

% constant chord type
if strcmp(cut.type, 'chord') == 1
    % estimate the number of points required
    rcrit = cut.chord/cut.dpmax;
    dpmin = cut.chord/cut.xstart;
    num_points_est = (2*pi*rcrit)/(cut.stepover*cut.dpmax);
    num_points_est = num_points_est + ((cut.xstart - rcrit)*2*pi)...
        /(cut.stepover*dpmin);
    num_points_est = ceil(num_points_est);

    if rcrit>cut.xstart
    % switch to constant angular spacing if maximum angle increment
    % is already exceeded at starting radius
```

```
        disp('NOTE: Max angular increment exceeded at start radius.')
      disp(Reverting to constant-angle mode.')
        cut.type = 'angle';
    else
    % generate a constant chord spiral, switching to constant angular
    % spacing at the point where the max angular increment is exceeded
        % preallocate
        coords_raw = NaN*ones(2, num_points_est);

        % first position
        coords_raw(2,1) = cut.dirsw*cut.xstart;
        coords_raw(1,1) = 0;
        cnt = 1;

        % generate spiral
        while cut.dirsw*coords_raw(2,cnt)>=0.0001;
            dp = abs(cut.chord/coords_raw(2,cnt));

            if dp>cut.dpmax
                dp = cut.dpmax;
            end

            coords_raw(1,cnt+1) = coords_raw(1,cnt) + cut.dirsw*dp;
            coords_raw(2,cnt+1) = coords_raw(2,cnt) ...
                - cut.dirsw*cut.stepover*dp/(2*pi);

            cnt = cnt + 1;
            if cnt + 1 > size(coords_raw,2)
                error('Insufficient preallocation size.')
            end
        end

        % trim out the unused part of the preallocated vectors
        coords_raw(:,(cnt+1):size(coords_raw,2)) = [];
        clear dp cnt j
    end

    clear num_points rcrit
end

% constant angle type
if strcmp(cut.type, 'angle') == 1
    num_points = (cut.xstart/cut.stepover)*(2*pi/cut.dpmax);
    cut.dx = cut.stepover*cut.dpmax/(2*pi);
    coords_raw = cut.dirsw*(0:num_points)*cut.dpmax;
    coords_raw(2,:) = cut.dirsw*fliplr(0:num_points)*cut.dx;
end

% wrap the c coordinates to the proper multiples of pi
coords_raw(1,:) = cut.dirsw*wrapTo2Pi(cut.dirsw*coords_raw(1,:));

%% raw part Z coordinates
coords_raw(4,:) = part.z_f(coords_raw(1,:), coords_raw(2,:));
```

```
%% compute TRC (tool radius compensation)
% outward normalized gradient at all points on the part (X,Z)
part.grad = zeros(2, size(coords_raw,2));
part.grad = [-part.dz_dr_f(coords_raw(1,:), coords_raw(2,:)); ...
    ones(size(coords_raw(1,:)))];
part.grad_on = part.grad./repmat((sqrt(sum(part.grad.^2))), [2,1]);
vals_trc = zeros(size(coords_raw));
vals_trc(2,:) = part.grad_on(1,:).*tool.roc;
vals_trc(4,:) = part.grad_on(2,:).*tool.roc - tool.roc;

%% compute TWC (tool waviness compensation) if desired
% this waviness compensation is based on two assumptions:
%   1. slope change is negligible due to the waviness (waviness <<
r_tool)
%   2. r_tool < max permissible r_tool, so I don't worry about
overcutting
%       or undercutting

vals_theta_deg = atan(part.dz_dr_f(coords_raw(1,:),
coords_raw(2,:)))*180/pi;
vals_twc = zeros(size(coords_raw));
if cut.sw_twc == 1
    vals_twc(2,:) = polyval(tool.wav_coeff, ...
        vals_theta_deg).*part.grad_on(1,:);
    vals_twc(4,:) = polyval(tool.wav_coeff, ...
        vals_theta_deg).*part.grad_on(2,:) - tool.wav_coeff(end);
end

%% apply TWC and TRC
coords_comp = coords_raw + vals_trc + vals_twc;

%% apply MEC (machine error comp)
vals_mec = zeros(size(coords_raw));
if cut.sw_conecomp == 1
    vals_mec(4,:) = vals_mec(4,:) +
sin(mach.dxz*pi/180)*coords_comp(2,:);
end

coords_comp = coords_comp + vals_mec;

%% shift Z values to be negative if desired
if out.negz == 1
    coords_comp(4,:) = coords_comp(4,:) - max(coords_comp(4,:));
end

%% perform any machine-specific post processing
coords_out = coords_comp;

%% output the nc code

if out.write == 1
    % get the base filename
    out.filebase = uiputfile('*.nc', 'Enter NC base filename');
    out.filebase = out.filebase(1:end-3);
```

```
    % broken up into segments if necessary
    out.numfiles = ceil(size(coords_raw,2)./out.maxlines);

    % start and end indices for each file segment
    out.indstart = out.maxlines*((1:out.numfiles) - 1) + 1;
    out.indend= out.maxlines*((1:out.numfiles));
    out.indend(end) = size(coords_raw,2);

    for cnt2 = 1:out.numfiles
        ncfilename = sprintf('%s_%d.nc', out.filebase, cnt2);
        fid = fopen(ncfilename, 'W+t');

        for cnt1 = out.indstart(cnt2):out.indend(cnt2)
            fprintf(fid, 'C%.5f X%.6f Z%.6f\n'...
                , coords_out(1,cnt1)*(180/pi), coords_out(2,cnt1)...
                , coords_out(4,cnt1));
            % fprintf(fid, 'line %d\n', cnt1);
        end

        fprintf(fid, 'M99\n');
        fclose(fid);
    end

    clear cnt1 cnt2 fid
end

%% option to save the toolpath coordinates in a .MAT file
pathfilename = uiputfile('*.mat', 'Enter filename to save as .MAT');
save(pathfilename, 'part', 'tool', 'cut', 'out', 'mach', 'coords_out',
'coords_raw', 'coords_comp');
```

B.2 STS Toolpath Backplotter

```
% caxturn_zerorake_circtool_bplot

% backplots slow tool servo operations with a circular zero rake tool
% loads the part structure and toolpath points from a saved MAT file
% uses the tool definition (radius, waviness) defined in the MAT file
%
% this code uses linear interpolation between toolpath points,
% just like an actual machine tool.
%
% this code assumes the starting stock is the 'perfect' part plus some
% stock allowance on top for the finishing depth of cut.

% John R. Troutman
% 12-23-2015



% backplot parameters
bplot.dp = deg2rad(1);          % backplot angular point spacing
bplot.dr = 0.005;               % backplot radial point spacing
bplot.doc = 0.01;               % simulated finish DOC

filename = uigetfile('*.mat', 'Select saved .MAT file');
load(filename);

%% redefine the tool and machine if desired to simulate errors
% % tool parameters
% tool.roc = 5.0;                 % tool nose radius (mm)
%
% tool radial shift: positive in the direction of increasing diameter
% (the tool is too far towards the part OD).  actual correction in the
% controller will depend on the spindle direction
% tool.radialshift = -0.005;

% tool waviness: polynomial coefficients
% tool radius deviation (+ outward) as function of tool sweep (theta)
% theta (degrees) measured +ve clockwise from tool tip
% tool.wav_coeff = [-3e-7 +1e-5 +2e-5 0];   % mm/deg^n
% cut.sw_twc = 1;                    % perform TWC if == 1
%
% % machine error components
% % dxz: angular misalignment of x, z axes
% % positive if greater than 90 deg between axes
% mach.dxz =  -0.02;           % dxz (degrees)
% cut.sw_conecomp = 1;         % comp for cone error if == 1

%% generate uncut surface (C,X,Y,Z)
c_unwrap = unwrap(coords_raw(1,:));
c_bplot = bplot.dp:sign(c_unwrap(end))*bplot.dp:2*pi-bplot.dp;
r_bplot = bplot.dr:sign(coords_raw(2,1))*bplot.dr:coords_raw(2,1);
[R_bplot, C_bplot] = meshgrid(r_bplot, c_bplot);

surf_ideal = cat(3, C_bplot, R_bplot);
```

```
surf_ideal(:,:,4) = part.z_f(surf_ideal(:,:,1), surf_ideal(:,:,2));
if out.negz == 1
    surf_ideal(:,:,4) = surf_ideal(:,:,4) -
max(max(surf_ideal(:,:,4)));
end
clear R_bplot C_bplot


%% build a gridded interpolant representing the tool at (0,0)
% this can be shifted around.
if isfield(tool, 'radialshift') == 0;
    tool.radialshift = 0;
end

bplot.tportion = 0.95;
points_tool = -
bplot.tportion*tool.roc:bplot.dr*1:bplot.tportion*tool.roc;
points_tool(3,:) = -sqrt(tool.roc.^2 - (points_tool(1,:) ...
    - cut.dirsw*tool.radialshift).^2) + tool.roc;
if cut.sw_twc == 1
    tool_dzdx = (points_tool(1,:) ...
        - cut.dirsw*tool.radialshift)./(tool.roc - points_tool(3,:));
    tool_theta_deg = atan(tool_dzdx)*180/pi;
    points_tool_wav = points_tool;
    points_tool_wav(1,:) = points_tool_wav(1,:) ...
        +
polyval(tool.wav_coeff,tool_theta_deg).*sin(tool_theta_deg*pi/180);
    points_tool_wav(3,:) = points_tool_wav(3,:) ...
        -
polyval(tool.wav_coeff,tool_theta_deg).*cos(tool_theta_deg*pi/180);
    points_tool_wav(3,:) = points_tool_wav(3,:) + tool.wav_coeff(end);
    points_tool(3,:) = interp1(points_tool_wav(1,:),
points_tool_wav(3,:)...
        , points_tool(1,:), 'pchip', 'extrap');
    clear tool_dzdx tool_theta_deg points_tool_wav
end
tool_gi = griddedInterpolant(points_tool(1,:), points_tool(3,:));

%% interpolate the unevenly-spaced toolpath points
path_interp_c = bplot.dp:sign(c_unwrap(end))*bplot.dp:c_unwrap(end);
path_interp_r = interp1(c_unwrap, coords_comp(2,:), path_interp_c);
path_interp_z = interp1(c_unwrap, coords_comp(4,:), path_interp_c);
path_interp_c_wrap = wrapTo2Pi(path_interp_c);

if cut.sw_conecomp == 1
    path_interp_z = path_interp_z - sin(mach.dxz*pi/180)*path_interp_r;
end

% build the cut surface at each backplot point
surf_cut = surf_ideal;
surf_cut(:,:,4) = surf_cut(:,:,4) + bplot.doc;
for cnt1 = 1:numel(c_bplot)
    slice = surf_cut(cnt1,:,4);
    ind = find(path_interp_c_wrap>c_bplot(cnt1) - bplot.dp/4 ...
        & path_interp_c_wrap<c_bplot(cnt1) + bplot.dp/4);
```

```
    for cnt2 = 1:numel(ind)
        coords_tool = tool_gi(r_bplot - path_interp_r(ind(cnt2))) ...
            + path_interp_z(ind(cnt2));
        jj = coords_tool<slice;
        slice(jj==1) = coords_tool(jj==1);
    end
    surf_cut(cnt1,:,4) = slice;
end
clear slice ind

%% remove r values outside the finished part radius for plotting
% this eliminates any lead-in effects\
surf_ideal_trimmed = surf_ideal;
surf_cut_trimmed = surf_cut;
jj = abs(surf_ideal_trimmed(:,:,2))>part.diameter/2 ...
    | abs(surf_ideal_trimmed(:,:,2))<(3*bplot.dr);
jj = repmat(double(jj), [1,1,4]);
surf_ideal_trimmed(jj==1) = NaN;
surf_cut_trimmed(jj==1) = NaN;
error_trimmed = surf_cut_trimmed(:,:,4) - surf_ideal_trimmed(:,:,4);
[x_plot, y_plot] = pol2cart(surf_cut_trimmed(:,:,1),
surf_cut_trimmed(:,:,2));

%% plot the resulting errors
figure(2)
surf(x_plot, y_plot, error_trimmed(:,:,4))
shading flat
view([0 90])
xlabel('X (mm)', 'FontSize', 14, 'FontName', 'Times')
ylabel('Y (mm)', 'FontSize', 14, 'FontName', 'Times')
h1 = colorbar;
ylabel(h1, 'Part Error (nm)', 'FontSize', 14, 'FontName', 'Times')
set(h1, 'FontSize', 14, 'FontName', 'Times')
set(gca, 'FontSize', 14, 'FontName', 'Times')
xlim([-part.radius part.radius])
ylim([-part.radius part.radius])
```